CHARACTERIZING THE INTERACTIONS OF MOLECULES WITH PHOSPHOLIPID VESICLES AND BILAYERS BY CONFOCAL RAMAN AND SINGLE-MOLECULE FLUORESCENCE MICROSCOPY

by

Grant Aaron Myers

A dissertation submitted to the faculty of
The University of Utah
in partial fulfillment of the requirements for the degree of

Doctor of Philosophy

Department of Chemistry

The University of Utah

December 2012

The University of Utah Graduate School

STATEMENT OF DISSERTATION APPROVAL

The dissertation of **Grant Aaron Myers**

has been approved by the following supervisory committee members:

Joel M. Harris , Chair **8/16/2012** Date Approved

Charles B. Grisson , Member **8/16/2012** Date Approved

John C. Conboy , Member **8/16/2012** Date Approved

Bethany A. Buck-Koehntop , Member **8/16/2012** Date Approved

Vladimir Hlady , Member **8/16/2012** Date Approved

and by **Henry S. White** , Chair of

the Department of **Chemistry**

and by Charles A. Wight, Dean of The Graduate School.

ABSTRACT

Molecular interactions with phospholipid bilayers are investigated using two types of laser-based microscopies. In optical-trapping confocal Raman microscopy, individual phospholipid vesicles are held in place in situ with laser tweezers while Raman scattering spectra are collected to report the preconcentration of analyte molecules via pH-gradient loading. A theory of accumulation is developed to account for source-depletion and vesicle buffering, factors that can significantly reduce the total accumulation. The system of 10 equations including 10 unknowns, five equilibrium constants and five experimental parameters was solved with symbolic-based mathematics software to yield a sixth-order polynomial having a single physically-meaningful, positive, real root. Utilizing this theory, an experiment is designed in which a single vesicle is manipulated by optical tweezers into isolation from other interfering vesicles and subjected to a variety of solution conditions. Raman spectra are analyzed quantitatively with a classical least squares method to determine the concentrations of compounds inside of the vesicle. When the pH gradient is 6.5 units and the citric-acid buffer inside of vesicles is 0.5 M, a 10^4-fold preconcentration factor of a model compound benzyl-dimethyl amine is observed, where accumulation into a 600-nm diameter vesicle is complete in less than 20 min.

Total-internal-reflection fluorescence (TIRF) microscopy is a technique with the dynamic range, spatial and temporal resolution capable of characterizing the interactions of single fluorescently labeled peptides with a planar supported lipid bilayer. TIRF images are analyzed with an adjacent pixel criterion to discriminate between molecular events and random noise exceeding the threshold. The bi-exponential distribution of event durations is interpreted with respect to a consecutive reversible three-state kinetics model, where unfolded peptides from solution first interact weakly with the bilayer then fold to persist for a longer time. Application of this model is shown to be capable of transforming the measured event times into the microscopic rates of the system including the rates of peptide folding and unfolding. The Gibb's free energy of the folding reaction from these measured rates, 1.7 kJ·mol^{-1} is comparable to that of other helix-forming membrane active peptides measured by isothermal titration calorimetry.

To my family:

Niki,

Emma, Leah and Becca

TABLE OF CONTENTS

ACKNOWLEDGMENTS

I gratefully acknowledge the support of mentor and advisor Joel M. Harris who welcomed me as an undergraduate into the group, who encouraged me to push through the discouragements of failed experiments, and who guided me through the labyrinthine paths of primary research. Truly, we stand on the shoulders of giants; I also have need to thank my predecessors who laid the foundations of my research in this group: Dan Cherney, and Ziggy Uibel, also Travis Bridges, Chris Fox and Josh Wayment, who initiated me in the ways of the laboratory. Thanks to other members of the Harris group who have endured my penchant to whistle and with whom I have enjoyed a terrific sense of collaboration and community; especially Jonathan Schaefer, for our warm discussions on research, science and other topics, also Eric Peterson, developer of the single molecule imaging analysis algorithms, which were instrumental to the research in Chapter 3. I should also mention Technische Universtät Braunschweig exchange students Daniel Gacek and Carolin Vietz, who were quick learners and great examples of hard work in the laboratory, who collected large amounts of image data for the benefit of my research. Thanks are due to my doctoral supervisory committee for reviewing this volume and for guiding my research through these years at the University of Utah, an institution that has done much for me and my family. National Science Foundation grants CHE-0654229 and CHE-0957242 supported this research. Finally, I wish to express deepest gratitude to

my family for their encouragement and support: to my mom and dad, Florence and Oliver Myers, also to John and Claudia Downs, and especially to my wife, Niki and our daughters Emma, Leah, and Becca—I love you to the stars and back.

CHAPTER 1

INTRODUCTION

1.1 Overview

This dissertation could be summarized by a quotation: "It has been said already many times that a picture is worth a thousand words; if that is true, then an *interface* is worth a thousand pictures."[1] This research is a literal manifestation of that assertion: thousands of pictures of interfaces were carefully framed and captured and many thousands of words were composed for their description in this volume. However, the interfaces here are not the intended computer graphical user-interfaces of the coiner of this quote, but rather microscopic chemical interfaces; specifically, phospholipid bilayers as in cell membranes. These are the foundation of the borders that define life—that separate living cells from their surroundings. Described in biology textbooks as a 'fluid mosaic',[2] they are varied and complex, and play many important roles: from simple barrier, to protein scaffold, to cytoskeleton anchor, staging area for receptor interaction, and communications transducer. This research explores some of the roles of phospholipid membranes using synthetic bilayer structures prepared in the laboratory with two types of laser-based microscopy.

In Chapter 2, spherical phospholipid vesicles or liposomes with pH gradients are investigated with a laser beam focused through a high-powered microscope to a diffraction-limited spot, enabling the techniques of optical tweezers to trap individual vesicles for analysis and Raman spectroscopy to obtain chemical information about those particles, including the amounts of analyte that become concentrated inside of individual vesicles. In Chapters 3, the laser beam is collimated through the microscope and aligned off center, such that a diffuse spot of light impinges upon a glass-water interface at such an angle as to be completely reflected, or totally internally reflected. This reflection establishes an evanescent excitation field whose intensity decays exponentially from the interface with distance into solution, enabling individual fluorescent molecules to be imaged with high spatial and time resolution as they interact with a planar supported lipid bilayer deposited at that interface. In Chapter 3, both the number of single molecules, as well as the durations of their interactions with phospholipid structures, are measured. The complex processes occurring at phospholipid membrane interfaces are dynamic on very short time scales and must be characterized with high interfacial selectivity, high spatial resolution, and multivariate analysis.

The thousands of images and spectra collected from interfaces in this research contain information that requires analysis and interpretation. Another theme in this research is the utilization of mathematical tools to enable predictions of complex behaviors, to analyze large multidimensional data sets, and to interpret those data to find underlying fundamental parameters. Particularly important in this endeavor was software for symbolic analysis used in the solving of systems of multiple algebraic equations, partial differential equations to generate predictive formulae and to interpret experimental measurements in terms of a rational kinetic model. Also linear algebra for multidimensional least squares was used in the quantitative analysis of Raman scattering spectra.

1.2 Synthetic Phospholipid Bilayer Structures

Glycero-phospholipids, one of the primary components of cell membranes, consist of a three-pronged glycerol center connected to a polar phosphoester head group and to two nonpolar fatty-acid acyl chains. Synthetic membranes used in this research consisted of a single type of glycerophospholipid called dipalmitoyl-phosphatidyl-choline or DPPC, where the head group is zwitterionic choline-modified phosphate and the acyl chains are both linear saturated 16-carbon fatty acids. The amphiphilic character of glycerophospholipids, as well as the matched size of tails to headgroup area allows these molecules to spontaneously assemble in aqueous environments to form extended planar structures, where hydrophobic effects drive the extended hydrophobic lipid chains to pack side-to-side and tail-to-tail in the nonpolar core of the bilayer, while polar head groups face outward into the solution. See Figure 1.1. The thickness of the bilayer is approximately 5 nm, while the mean headgroup area of a single phospholipid is approximately 0.4 nm^2.[3] In the gel-phase, lipids used in the present research have been shown to exhibit a ~30° tilt of acyl tails with respect to the plane of the bilayer.[4] When dried lipid films are hydrated and heated above the gel to liquid-crystalline transition temperature, large (>10 μm) multilamellar vesicular structures form spontaneously. These structures can be refined by high-pressure extrusion through uniform track-etch pores to establish a narrowed distribution of spherical vesicles or liposomes of more

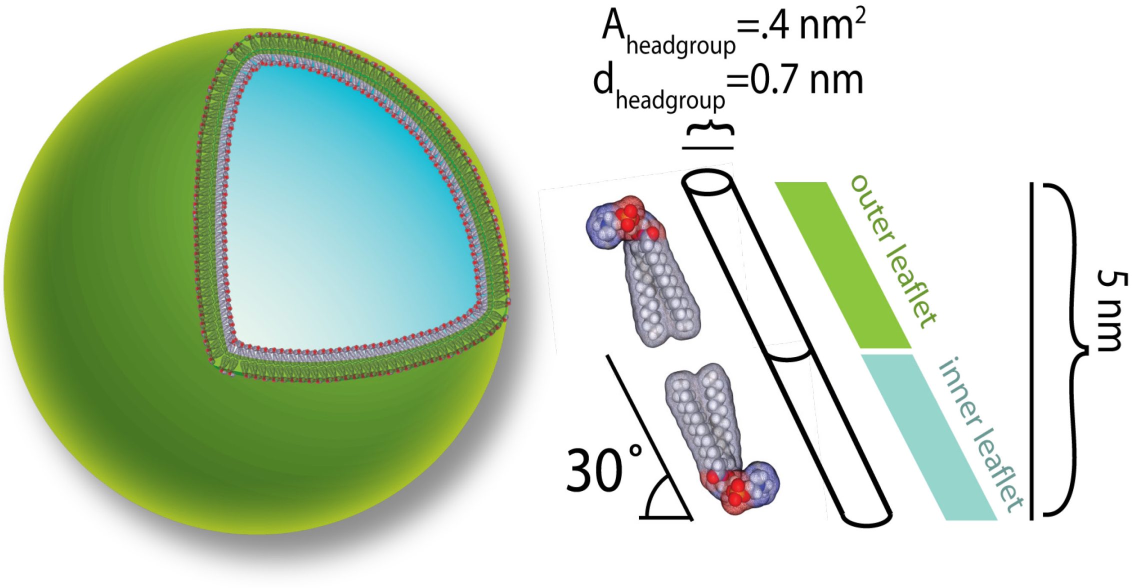

Figure 1.1 Phospholipid bilayers form spontaneously in water, where the amphiphilic character and molecular shape of phospholipids drive hydrophobic acyl chains to pack together in an extended planar structure, like a spherical vesicle with polar headgroups facing inwards and outwards. When the diameter of the vesicle is less than 50 nm, the system is sterically destabilized.

uniform size for analysis. When vesicles are extruded with diameters < ~100-nm, the radius of curvature of the vesicle is comparable to the thickness of the bilayer, destabilizing the vesicles. These preparations, which can also prepared by sonication,[4] are useful in deposition techniques to form planar supported lipid bilayers on solid substrates by vesicle fusion.[5]

In an alternative deposition method that allows better control of the density of lipids and also allows for asymmetric leaflets, lipids are dissolved in volatile solvent and deposited on an air-water interface. The phospholipids spontaneously spread uniformly over the interface with polar headgroups directed towards the solution and the nonpolar fatty acid chains directed towards the air. This monolayer can be compressed by simply moving barriers to change the total area of the interface such that the packing of lipid acyl chains approaches that of vesicles. As shown in Figure 1.2, solid substrates can then be drawn through the interface to deposit a single monolayer at a time. Deposition of a bilayer onto a microscope coverslip surface in this research was accomplished with two steps[6]: first, the substrate was drawn upwards through the interface while oriented perpendicular to the interfacial plane (Langmuir-Blodgett technique) as shown in Figure 1.2A, followed by downwards immersion with the surface oriented parallel to the interface (Langmuir-Schaeffer technique) as shown in Figure 1.2B. Although the first monolayer is stable in air, once a second monolayer has been added, the substrate must remain submerged. Microscope flow cells with the supported lipid bilayer must be assembled in a water bath, and care must be taken to prevent delamination of layers by interaction with the atmosphere or air bubbles in the flow train.

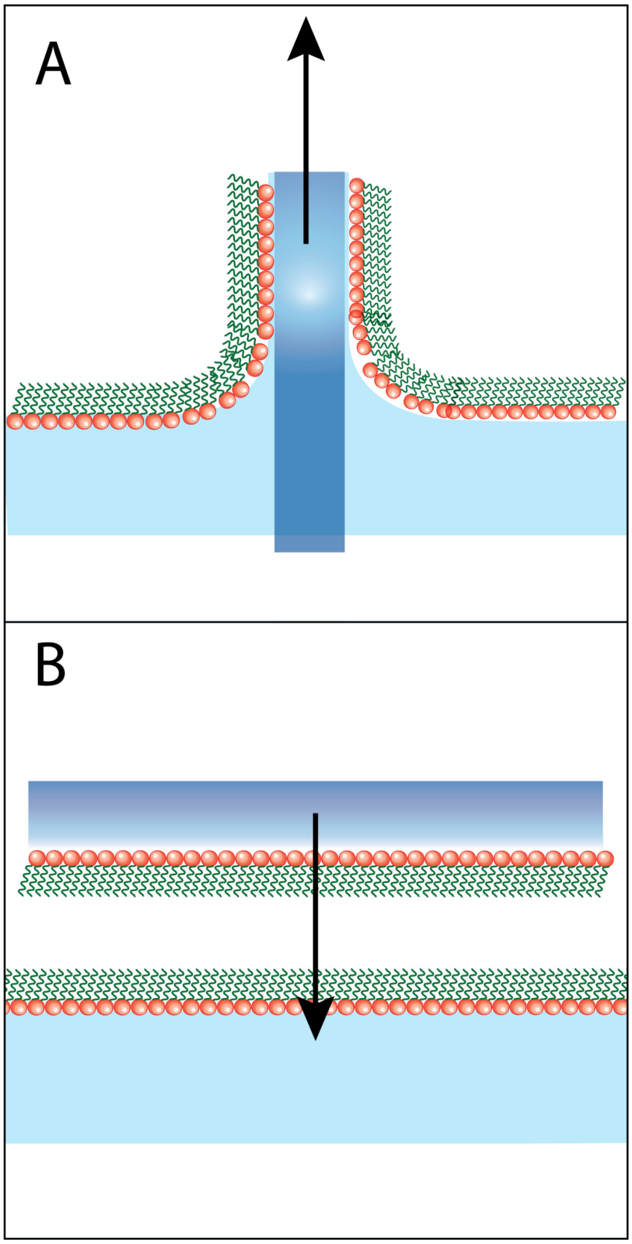

Figure 1.2 Langmuir deposition of a bilayer on a solid substrate can be accomplished with two steps. In A, the substrate is oriented perpendicular to the plane and drawn upwards through lipids deposited at the water/air interface. In B, the substrate is then oriented parallel to the plane and immersed in the solution.

1.3 Ion Gradients Driving Vesicular Accumulation

The organization of the molecules in the phospholipid bilayer is fundamental to its role as a barrier to transport in cell systems. The hydrophobic core of the lipid bilayer prevents the transport of charged ions, so that ions can be selectively held in compartments surrounded by bilayers. Indeed, ion gradients are commonplace in cells, where biology has evolved thousands of selective ion channels and pumps to establish local ion concentrations, and enormous amounts of energy are expended to maintain ion gradients.[7] The establishment of a proton gradient across the thylakoid lipid membranes in mitochondria via the electron transport chain is the primary role of oxygen reduction in aerobic eukaryotic organisms.[8] The dissipation of ion gradients is involved in the rapid transmission of action potentials down axons for neuronal communication.[9] In these cases, ion gradients represent a convenient form of stored chemical potential energy that can be readily transduced to perform a wide variety of cell functions.[10]

That the energy of a proton gradient can be used to concentrate ionizable compounds inside of phospholipid vesicles was recognized by researchers in synthetic preparations of liposomes containing small hydrophobic anesthetic[11] or antibiotic[12] molecules with protonatable amine groups. As shown in Figure 1.3, the neutral form of the molecule is free to dissolve in and permeate the nonpolar bilayer core, while the ionized form will not. If the aqueous interior of the liposome favors the ionized form of the molecule, it will become entrapped and concentrated until the activity of the neutral form, the form free to partition in both compartments, reaches equilibrium inside and outside of the vesicle. The interior concentration is governed by the acid-base equilibrium of the ionizable molecule, where, inside of the liposome, a large

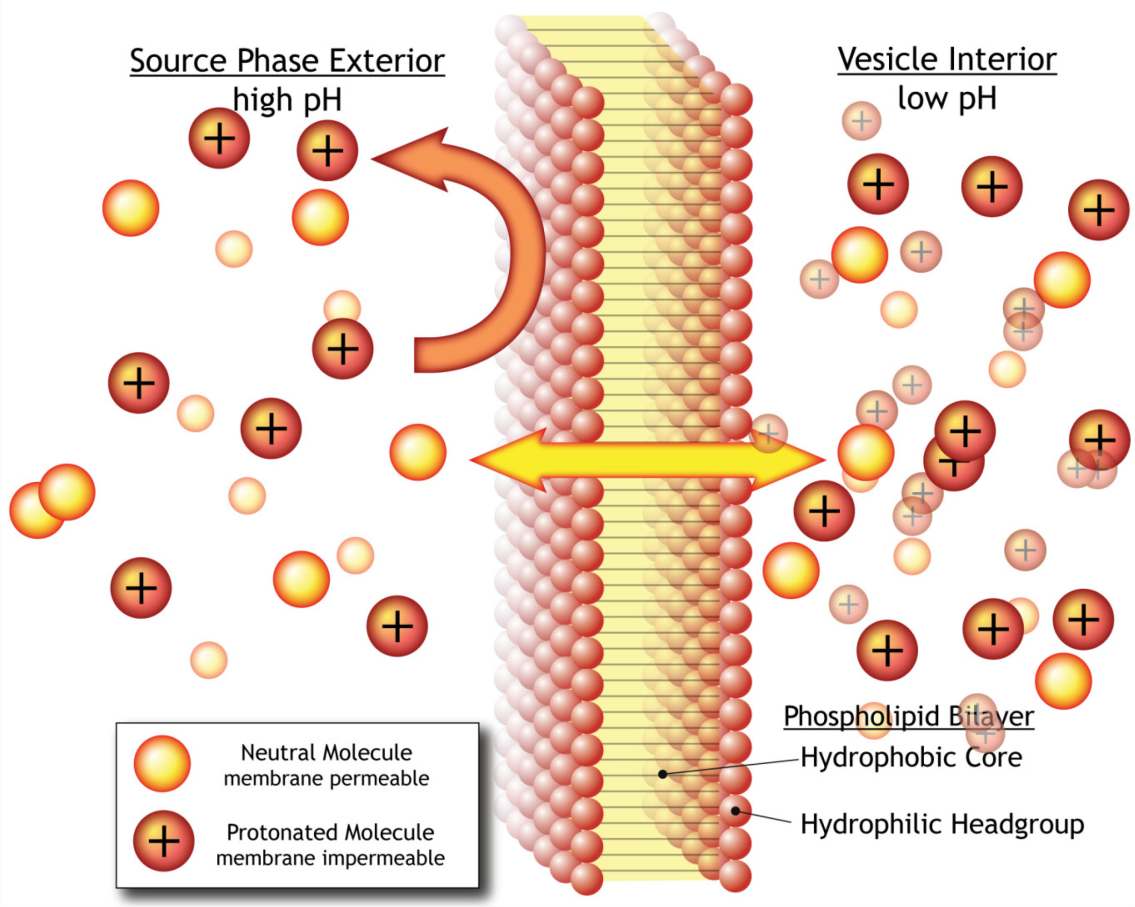

Figure 1.3 Concentration of a protonatable molecule inside a vesicle with a pH gradient. Only the neutral form is free to permeate the membrane and will partition equally in both compartments. However in the interior environment, the same concentration of neutral molecule supports a much larger population of the protonated form.

concentration of the ionized form of the analyte is required to support even a small concentration of the neutral form. Thus a small concentration of neutral compound outside of vesicles can be taken up, ionized, and concentrated to a high degree inside of the liposomes.

This pH-gradient loading technique has been successfully applied to preparations of liposomal pharmaceuticals,[13] liposomal flavorings in food science,[14] and liposomal dyes in textiles.[15] In Chapter 2, the capacity of vesicles to take up large quantities of analyte is explored, where the total flux to the inside of vesicles is sufficient to change the pH and deplete the concentration of the analyte outside of the vesicles. To account for these processes and predict accumulation of analyte into vesicles, the theory of accumulation was developed with equations accounting for the ionization of the buffer and for the mass balance of molecules in the system.

1.4 Optical Trapping Confocal Raman Microscopy

1.4.1 Optical trapping

To investigate the interior composition of phospholipid vesicles, optical trapping or optical tweezers can be used to hold an individual vesicle at a fixed location while Raman scattering reports information about the local chemistry within the vesicle. Optical trapping of particles is accomplished by focusing a coherent beam of light to a diffraction limited spot, where the large photon flux and corresponding electric fields through that tiny spot are sufficient to exert optical forces on particles of size comparable to the laser focus.[16,17] When the particles have a greater dielectric constant than the surrounding solution environment, they will be drawn into the light along the intensity gradient, which is most intense at the center of the focus. When the beam is tightly focused, the particle can be held at the beam waist, with a slight displacement in the direction of propagation due to the scattering of photons by the molecules in the particle and the associated transfer of momentum. Thus, individual particles can be isolated, held in place, and moved into new environments for analysis. Optical tweezers have been applied in biology to trap individual viruses,[18] single cells,[19] cell organelles[20] and to measure the forces of individual motor proteins.[21] In the present research, optical tweezers are utilized to study in situ individual phospholipid vesicles in an aqueous environment, where the particles can be trapped and physically manipulated into new solution environments and analyzed with Raman spectroscopy.

1.4.2 Vibrational Raman spectroscopy

An optical trapping laser beam is also sufficiently intense to produce significant inelastic Raman scattering from trapped particles. This scattering can be collected by the same objective that focused the trapping beam and then dispersed to produce a spectrum. Raman scattering is a vibrational spectroscopy associated selectively with molecular vibrations and rotations that result in a change in polarizability for the molecule.[22] The vast majority of photons that interact with molecules are elastically (Rayleigh) scattered such that the frequency of scattered photons is unchanged relative to the incident radiation. When Rayleigh scattering is filtered out, a small fraction (~1 in 10^7) of scattered photons with different frequencies are observed. Some of these inelastically scattered photons have a higher energy (anti-Stokes Raman scattering) than the incident photons, but a much larger fraction have a lower energy (Stokes Raman scattering). The

Raman spectrum of scattered photons has peaks whose energy-shift relative to the incident light is characteristic of the molecular vibrations that produced the scattering. The oscillating electric fields associated with the incident photons are coupled into the oscillating polarizability of electrons that are associated with a particular molecular mode of vibration. As illustrated in Figure 1.4, incident photons excite molecules to a virtual or polarization state whose energy relative to the initial state corresponds to the incident photon energy. In Rayleigh scattering, the molecule relaxes back to the initial state and the scattered photon is not shifted in frequency. In Stokes Raman scattering, the molecule relaxes to a higher-energy vibrationally excited state, and the scattered photon has a lesser energy than the incident. In anti-Stokes Raman scattering, the molecule begins in a vibrationally excited state, and relaxation from the virtual energy state is to the ground state, resulting in a scattered photon having a higher energy relative to the incident radiation. Raman spectroscopy is a powerful tool yielding molecularly specific vibrational information without the use of extrinsic labels in aqueous conditions. It is commonly used to verify the presence of compounds, quantify the relative amounts of materials present, as well as measure molecular conformations, and even the dielectric environment of molecules.[23]

1.4.3 Optimizing Raman scattering collection with a confocal aperture

To selectively acquire Raman scattering from optically trapped particles, a confocal imaging technique is utilized. Confocal, meaning ‘coincident with the focus’, refers to the placement of an aperture in a focal plane within the collection train that limits the light passed to the detector to only in-focus light, where out-of-focus light is

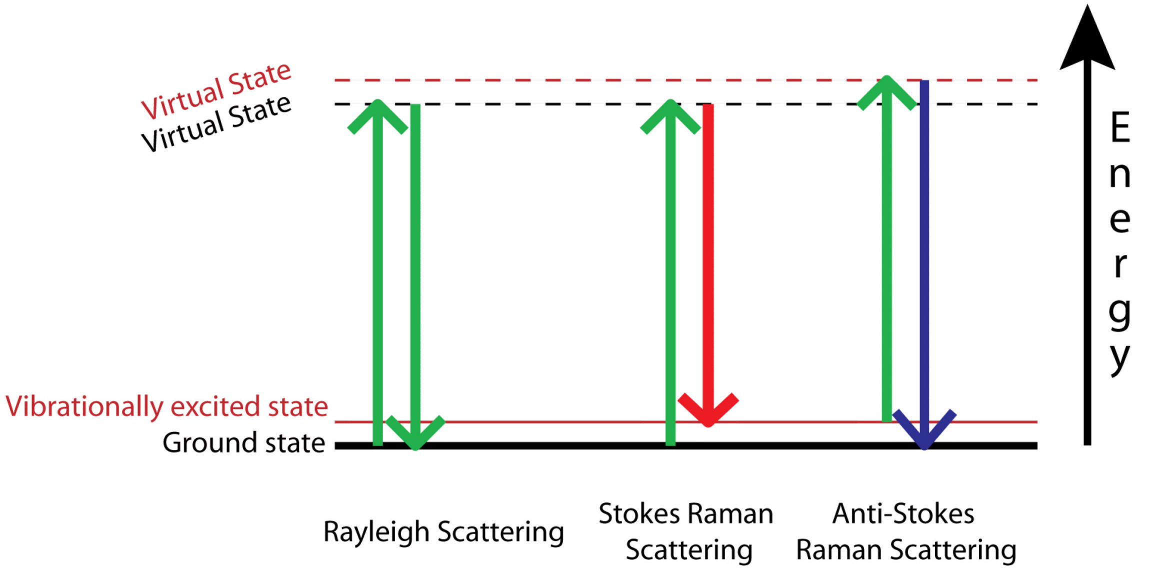

Figure 1.4 Types of photon scattering include Rayleigh, Stokes Raman and anti-Stokes Raman. In all three types, incident photons induce virtual states; in Rayleigh, the scattered photon is of the same energy as the incident; in Stokes Raman, the molecule relaxes to a vibrationally excited state and the scattered photon is shifted to a correspondingly lower frequency; in anti-Stokes Raman, the molecule begins in a vibrationally excited state, but relaxes to the ground state and the scattered photon is shifted to a corresponding higher frequency.

blocked by the aperture, which closely matches the size of the focused spot[24] (see Figure 1.5). In the confocal Raman microscope used in this research, the diffraction-limited spot size through the 1.4-numerical aperture 100x microscope objective is ~560 nm. The confocal aperture in this system is composed of two elements:[25] first the Raman scatter is collected and focused onto the entrance slit of a monochromator, where the slit-width is set to match the focal width, 50-μm in the image plane, or ~500-nm magnified 100x, eliminating out-of-focus light in one of the two dimensions. The second element of the confocal aperture is accomplished by limiting the analysis of light passed from the monochromator to only that light incident upon a small number of pixel rows of the charge-coupled device camera. These pixel rows match the focal width in the image plane, thus eliminating out-of-focus light in the second dimension. When the diameter of the particle matches the beam waist at the focus, the Raman scatter of the particle is collected exclusive of most of the interference from the surrounding solution. In the present research the confocal volume selectively interrogated by the 647-nm laser, focused through the 1.4-numerical-aperture 100x objective is ~0.5 fL.

1.4.4 Analysis of multicomponent spectral data

While Raman scattering of a single vesicle can be interrogated with exquisite spatial selectivity, the challenge is to interpret those spectra, which are a superposition of the spectra of the individual components present in the confocal volume. The resolution of those components can be accomplished with multidimensional analysis methods including classical least squares, inverse least squares, principal component analysis and partial least squares. These techniques are based on the additive property of Raman

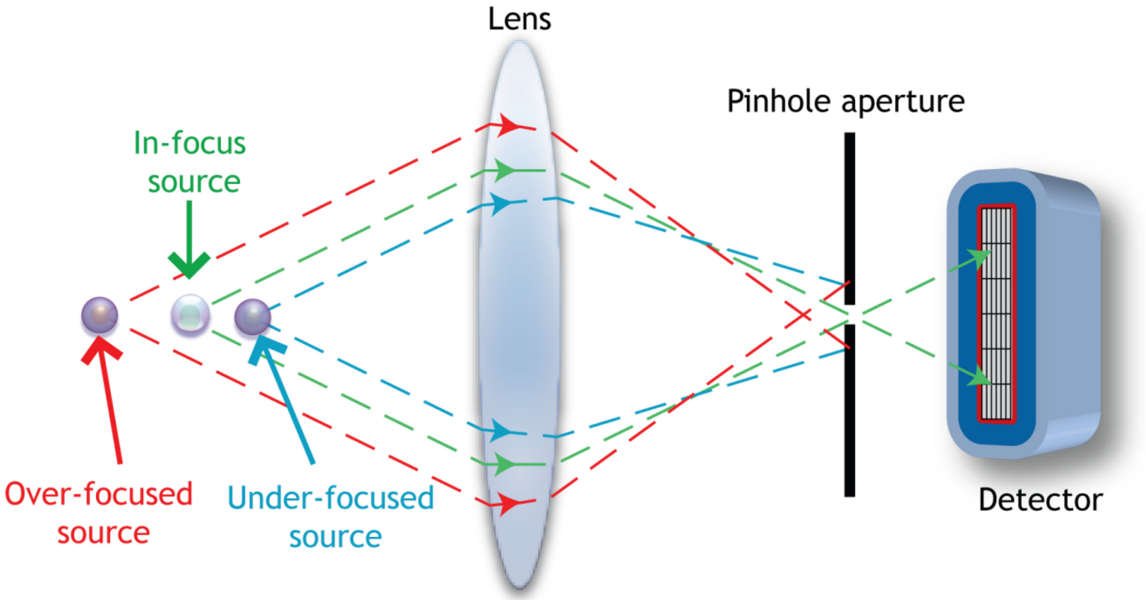

Figure 1.5 Confocal aperture optimization of collected light. When a pinhole aperture is placed in a focus plane, out of focus light is blocked, so that the source can be selectively imaged with the detector.

scattering intensities, where the contribution of a given component to a measured spectrum is proportional to its concentration and the scattering cross section for the characteristic vibration associated with that Raman shift frequency. The simplest application of this principle to spectral interpretation involves measuring the peak intensity at a single frequency. However, a full Raman spectrum contains potentially useful information at all frequencies. Most polyatomic molecules have a number of Raman active vibrational modes and therefore a number of different peaks at various Raman shift frequencies across the spectrum. Classical least squares (CLS) takes advantage of that fact, applying the superposition principle to all frequencies measured across the entire spectrum. CLS requires knowledge of all of the components contributing intensity to the Raman spectrum, and begins with the construction of a set of the spectra of pure components, as illustrated in Figure 1.6, where A is a matrix of m calibration spectra measured over l frequencies, C is a matrix of the concentrations of the n components in each calibration spectrum, and K is the matrix of pure component Raman spectra or equivalently, a matrix of the scattering cross sections and optical throughput for each component at each frequency.

$$[A]_{m\times l} = [C]_{m\times n} * [K]_{n\times l} \qquad [1.1]$$

Note that the determination of K does not necessarily require the measurement of calibration spectra from preparations of individual pure components; spectra from mixtures of components whose concentrations are known are also suitable, as long as the number of calibration spectra measured (m) is at least the number of components (n),

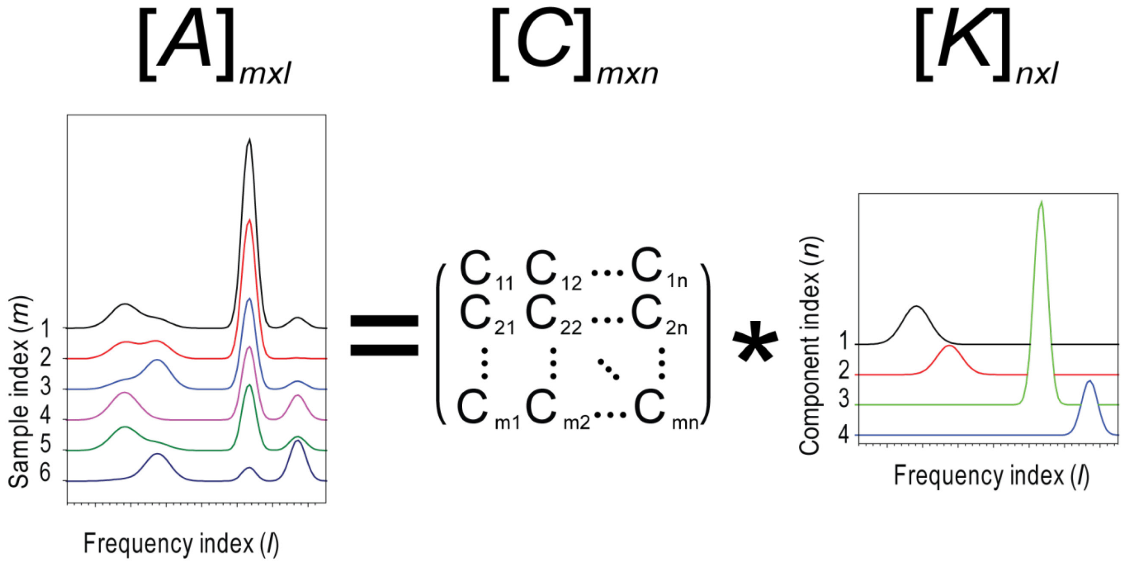

Figure 1.6 Classical least squares multicomponent analysis. The matrix of measured Raman spectra, A, are composed of the product of a matrix of concentrations, C, and a matrix of pure spectra, K.

each component is present in at least one mixture, and at least *n* samples are not mixtures or dilutions of other samples (*n* samples are linearly independent).

When these three conditions are satisfied, the C matrix as defined in Figure 1.5 is of full rank in the *n* (column) dimension, and therefore has a left pseudoinverse[26] so that the least squares best fit K matrix can be determined:

$$[K]_{n\times l} = \left([C]^{\mathsf{T}}{}_{n\times m} * [C]_{m\times n}\right)^{-1}_{n\times n} * [C]^{\mathsf{T}}{}_{n\times m} * [A]_{m\times l} \qquad [1.2]$$

For any data set (D) consisting of mixtures of pure components of unknown concentrations (U), the U matrix can be determined from D and the right pseudoinverse of K:

$$[U]_{m\times n} = [D]_{m\times l} * [K]^{\mathsf{T}}{}_{l\times n} * \left([K]_{n\times l} * [K]^{\mathsf{T}}{}_{l\times n}\right)^{-1}_{n\times n} \qquad [1.3]$$

This linear algebra expression computes the linear least squares best fit of U*K to the data, by effectively scaling the concentrations of components in the U matrix to minimize the sum of the squared residuals between and D and U*K. In the present research, Raman scattering from an optically trapped vesicle arises mainly from the highly polarizable phospholipids, though significant contributions from the buffer inside of the vesicle, as well as outside of the vesicle can be detected. Thus classical least squares treatment of the Raman spectral data yields information about the relative size of the vesicle, the amount of lipid, the contents of the vesicle, as well as the conditions outside of the vesicle.

To summarize, optical trapping confocal Raman microscopy is a technique capable of in situ characterization of individual phospholipid vesicles, where laser tweezers hold the particle in place while vibrational information from Raman scatter is collected. The placement of a confocal aperture in the imaging optics train limits collection to only scattering from a subfemtoliter confocal volume. Raman scattering is additive, so that the technique of classical least squares can be utilized to determine the concentrations of components in the optical trap. One challenge in Raman spectroscopy is that it is a weak effect, where roughly 1 in 10 billion incident photons is inelastically scattered. This limits the sensitivity and dynamic range of measurements, which typically require greater-than millimolar concentrations of analyte and minutes of integration time to accumulate sufficient signal, severely limiting the timescales of dynamic phenomena that can be characterized by this technique. Although enhancement schemes are being developed, such as surface-enhancement,[27,28] stimulated[29] and resonance-enhancement[30] with tunable excitation, these techniques are limited to noble metal substrates or require more complicated instrumentation to implement. Furthermore, optical trapping confocal Raman is an inherently serial technique, where only a single vesicle can be characterized at a time. Few biological processes occurring at phospholipid membranes have dynamics on the time scale of minutes. To probe faster kinetics of molecular interactions with bilayers as in Chapter 3, an analytical technique with much greater sensitivity, time resolution, and spatial multiplexing is needed. Single molecule fluorescence imaging meets many of these requirements.

1.5 Single Molecule Total Internal Reflection Fluorescence Microscopy

Fluorescence microscopy is a technique with outstanding dynamic range capable of even single molecule detection with very high time resolution. Typically, it requires the use of extraneous labels for visualization of molecules of interest that may perturb the interactions and behavior of the system. Total internal reflection fluorescence microscopy is a surface selective technique based upon the principle of a nonpropagating evanescent excitation field established when the light source is reflected off of a high-to-low refractive index interface at an angle greater-than the critical angle for the boundary,[31] as illustrated in Figure 1.7. The critical angle, $\theta_{critical}$, as derived from Snell's law of refraction is given by the following equation:

$$\theta_{critical} = \sin^{-1}\left({}^{n_2}/_{n_1}\right) \qquad [1.4]$$

where n_2 is the lesser index of refraction and n_1 is the greater. For the glass water interface, the refractive indices are 1.52 and 1.33, respectively, corresponding to a critical angle of 61°. The evanescent field is a result of the oscillating electromagnetic waves of the photons avoiding a discontinuity at the reflective boundary; this is analogous to the quantum mechanical particle-in-a-box with finite boundaries, where the probability distribution function for the particle (or photon) decays exponentially with distance from the boundary (or refractive interface). As long as there is an absence of absorbing material in the low-refractive index medium, no energy is transmitted across the

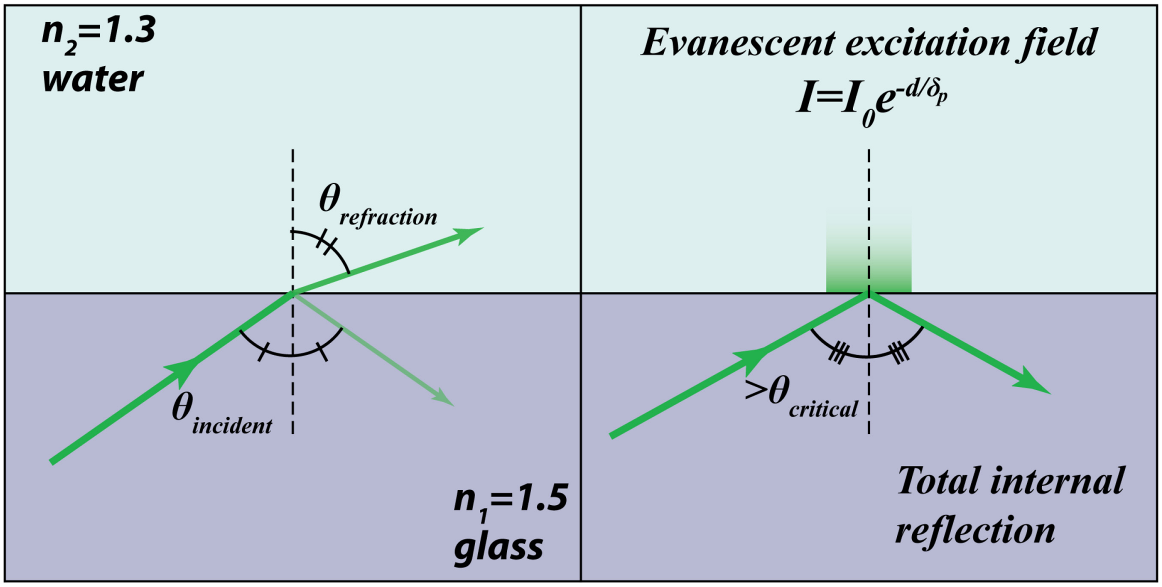

Figure 1.7 Total internal reflection occurs when the angle of incidence is greater than the critical angle. The intensity of the evanescent excitation field decays exponentially with distance from the interface.

reflective interface. Although the Poynting vector for the evanescent field is finite in the direction perpendicular to the interface, it has a time average of zero.

The characteristic decay distance for the evanescent field in TIRF microscopy is a function of the wavelength of the light, the angle of incidence and the refractive indices of media at the interface as given by the following equation:[32]

$$\delta_p = \frac{\lambda}{4\pi \cdot n_2\sqrt{(n_1 \sin\theta_i / n_2)^2 - 1}} \qquad [1.5]$$

where λ is the wavelength and θ_i is the angle of incidence. As observed in the plot in Figure 1.8, the penetration depth exhibits a singularity when the angle of incidence equals the critical angle, corresponding to the transition from total internal reflection to refraction and propagation into the second medium. In practice, for the TIRF microscope system used in the present research where the excitation wavelength is 532 nm and the interface is glass/water, the characteristic penetration length is ~150 nm, corresponding to an angle of incidence of 63°. Thus only fluorophores very close to the interface are selectively excited, and the background from fluorophores in the bulk solution is greatly reduced.

Two methods[33] for accomplishing TIRF microscopy include prism TIRF[34] and through-the-objective TIRF.[35] For the former, a prism is placed, usually above the sample and excitation light is passed through the prism and reflected off the prism/sample interface. Fluorescence at the interface is collected through a microscope objective placed opposite the prism. Through-the-objective TIRF microscopy, the technique used

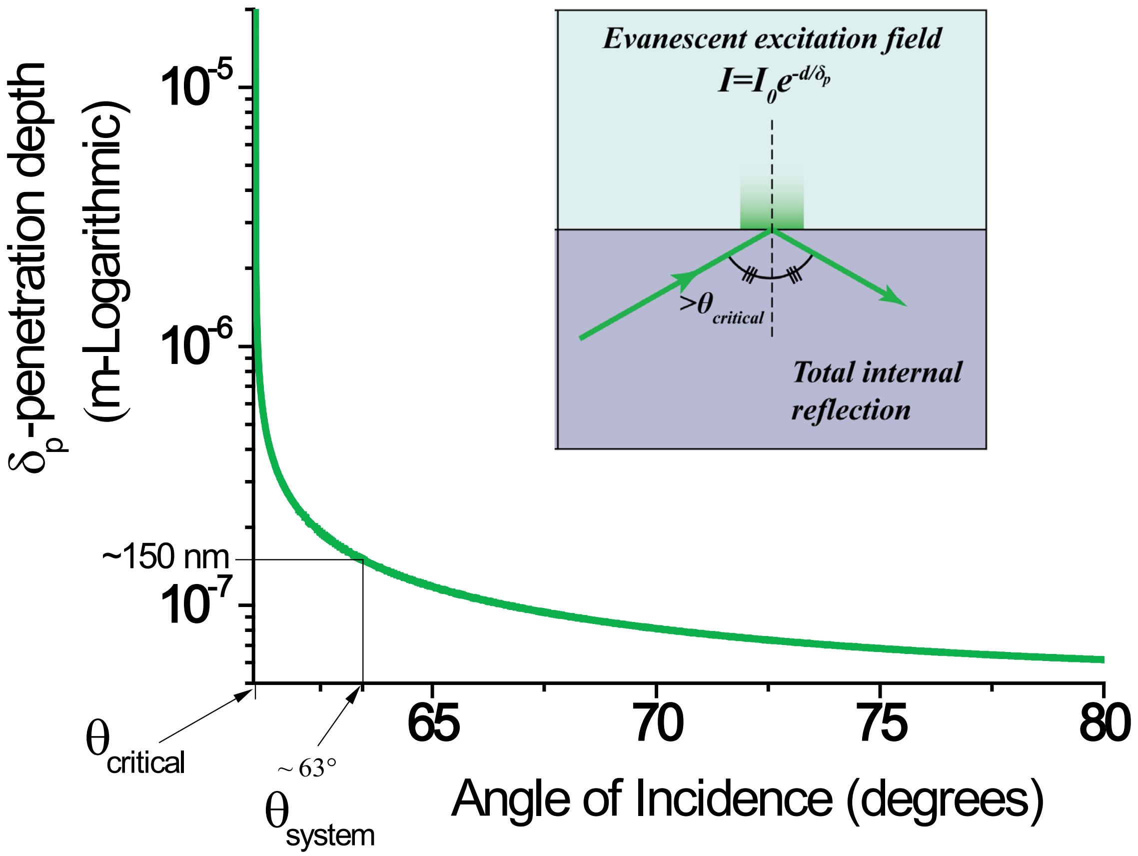

Figure 1.8 Plot of the characteristic distance of the exponentially decaying intensity of the evanescent excitation field. For the system used in the present research, with a 532-nm excitation source at an angle of 63°, the penetration depth is ~150 nm at the glass/water interface.

in the present research,[36,37] is accomplished by alignment of a focused excitation beam off-center through the objective rear aperture. As shown in Figure 1.9, the result is a collimated beam exiting the objective at an angle. When the numerical aperture of the objective is high, the acceptance angle of the system can be sufficient to allow the collimated beam to impinge upon the glass coverslip/sample interface at angles greater than the critical angle. The same objective is also used to collect the fluorescence from particles in the evanescent field, which is filtered to remove the reflected excitation light and passed to a detector.

In the present research, an imaging electron multiplying charge coupled device (EM-CCD) camera was utilized for data collection. These cameras are capable of single photon counting as enabled by a series of high-voltage electron-accelerating impact-ionization amplification gain stages to multiply the number of electrons generated by a photon, thus increasing the signal charge passed to the output amplifier in the readout train.[38] High time resolution is accomplished with a frame-transfer technique, illustrated in Figure 1.10, where the CCD size is doubled and half of the sensor is covered by an opaque mask. After the image has been collected on the exposed side of the CCD, it is rapidly shifted to the masked portion of the sensor so that the much slower readout of pixel intensities can be accomplished while the next frame is collected on the unmasked side of the sensor. The Andor iXon^{EM}+ 897 camera used in the present work is capable of imaging a 256x256-pixel region in real time at a rate of ~30 ms·frame^{-1}, though most work was performed at a rate of 100 ms·frame^{-1} to achieve better signal-to-noise in images of single molecules.

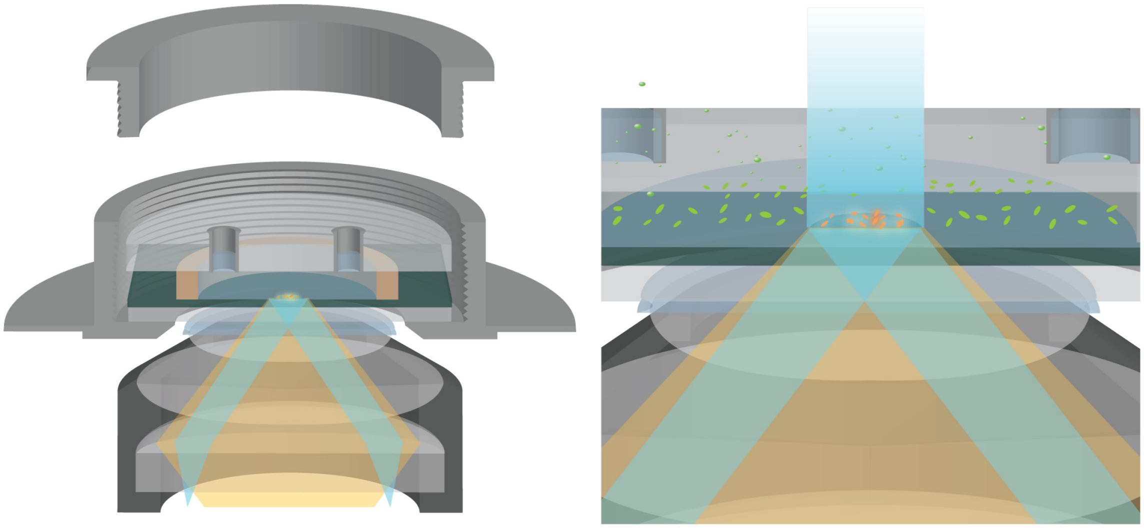

Figure 1.9 Through the objective TIRF schematic. Excitation light (blue) is focused off-center in the objective so that a collimated beam impinges on the glass/solution interface at an angle greater than the critical angle. Fluorescence (orange) is collected by the objective and passed to the camera for imaging.

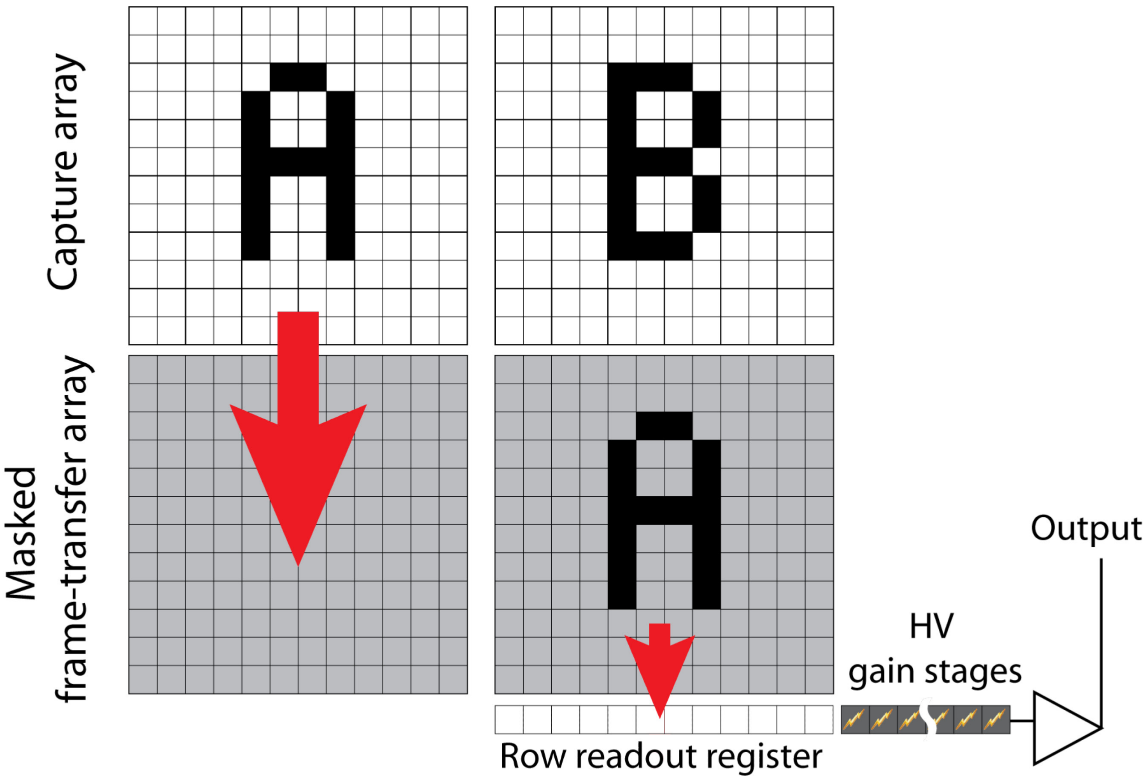

Figure 1.10 Frame transfer scheme for high time resolution charge-coupled device camera. A captured image is rapidly transferred to a masked array to allow for much slower row-readout while the next frame is captured.

One of the challenges of single molecule imaging to measure the kinetics of interactions at the interface is the infrequent occurrence of bright background pixels that exceed the threshold intensity of a molecule (false positives), either from spurious noise or cosmic rays. These can be distinguished from molecular events by implementation of an adjacent pixel criterion,[39] where the point-spread function of a molecular spot after the magnification of the microscope system is distributed over more than one pixel on the CCD camera. While the probability that a single noise pixel exceeds a threshold may be significant, the probability that two (or three) noise pixels adjacent to each other all exceed the threshold is greatly reduced (see Figure 1.11). In addition to this spatial-filtering to distinguish events within an individual frame, a second layer of event filtering occurs in the time domain, where the positions of molecular events in a given frame are compared to the positions of events in subsequent frames. The probability that the adjacent noise pixels in the same position exceed a threshold in two (or more) consecutive frames is vanishingly small. Thus, by neglecting spatially isolated single frame events, false positives are further reduced. However, these spatial criteria and temporal filtering processes for reduction of the false positive rate can generate a concomitant increase in the false negative rate. Thus for a variety of data sets, intensity threshold, event position tolerance and the number of adjacent pixels required are parameters that must be tuned based on the signal-to-noise ratio of a set of data.

When observing single-fluorophore labeled molecules, stochastic fluctuations in the intensity of molecular spots, photoblinking or transitions to long-lived dark states may reduce the intensity of the point spread function below the threshold in a given frame,[40-43] effectively shortening the measured length of events by dividing a single event

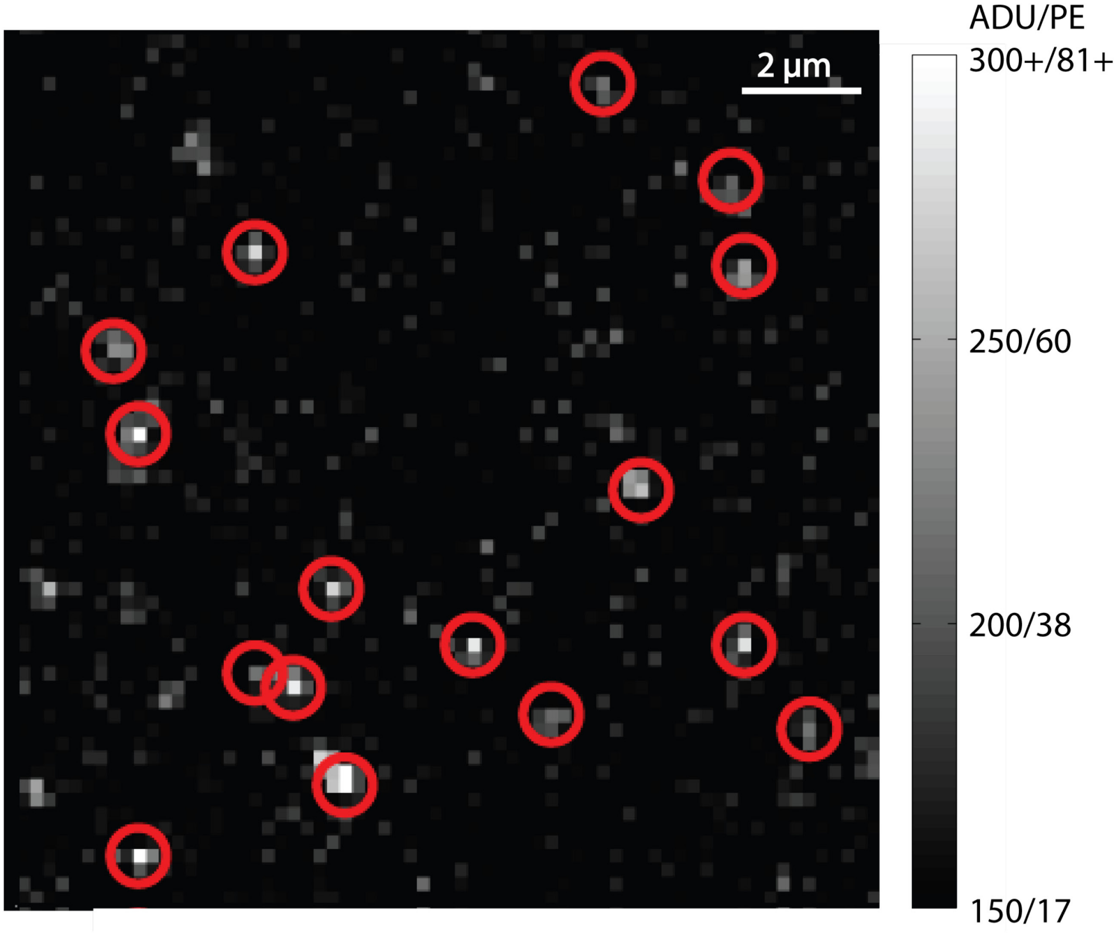

Figure 1.11 Single molecules, called out with red circles are identified with a two-pixel criterion and distinguished from single bright background pixels and single frame events. The threshold was 37 photoelectrons or 3.0 standard deviations above the mean background intensity. While the probability that a single pixel exceeds this threshold in a 256x256 pixel frame is 4.9e-4 or 32 pixels·frame^{-1}, the probability that two noise pixels will be adjacent is only 0.125 false positives frame^{-1}.

into a number of shorter events. These effects are mitigated by bridging brief off states within a bridging time parameter, τ_b, where two events occurring in the same position within τ_b seconds are connected together, bridging the gap so that the length of the event is correctly reported. When the density of molecular events in an image is sparse and the binding rate is small, the probability that a second molecule from solution arrives at the same site within the bridging time (or the within the duration of an event) is also small.

Another critical challenge with the imaging of single fluorophores to measure the kinetics of interactions is photobleaching, where the length of events is underreported because the fluorophore transitions to a long-lived dark state before the molecule of interest leaves the interface. Photobleaching by the excitation source is dependent on the intensity of the source, but there is a trade-off because fluorescence signal is also excitation intensity dependent. Ideally, the characteristic time of photobleaching is much longer than the length of the events characterized. When photobleaching is suspected, it is important to measure the molecular kinetics at various laser powers and find a power low enough not to perturb the measured rates, but high enough to provide sufficient signal-to-noise for reliable images.

1.6 Dynamics of Single Molecules at Phospholipid Interfaces

In Chapter 3, the dynamics of fluorescently-labeled single molecules of a soluble, membrane active peptide interacting with a planar supported lipid bilayer are characterized with imaging total internal reflection fluorescence microscopy. The image data analysis tools described above were applied to find the number of molecules interacting with the interface as well as the length of time individual molecules last at the interface. It was observed that the histogram of these residence event times is biphasic, having two apparent populations of molecules that persist at the interface for significantly different lengths of time.[37] It is known that many soluble membrane active peptides exist as a random coil in solution that fold into an organized secondary structure, such as an alpha-helix.[44] The transition to a folded state likely represents a kinetic barrier that some molecules interacting with the interface do not surpass. Here then is a rational explanation for the two populations of molecular residence times: the short-lived events are for those molecules that do not fold successfully before leaving the interface, and the long-lived events represent molecules that successfully fold. Those that do fold, given enough time, unfold and return to solution via the intermediate state. This behavior can be described by a consecutive three-state reversible kinetics system as illustrated in Figure 1.12:

$$A \underset{k_2}{\overset{k_1}{\rightleftarrows}} B \underset{k_4}{\overset{k_3}{\rightleftarrows}} C \qquad [1.6]$$

The four microscopic forward and reverse rate constants, k_n, in this scheme include the binding and unbinding rates of the peptide, as well as the folding and unfolding rates of the peptide. The relationships between these fundamental interaction parameters and the measured characteristic event lengths can be derived from an analysis of the system of differential equations describing the scheme in Equation 1.6.

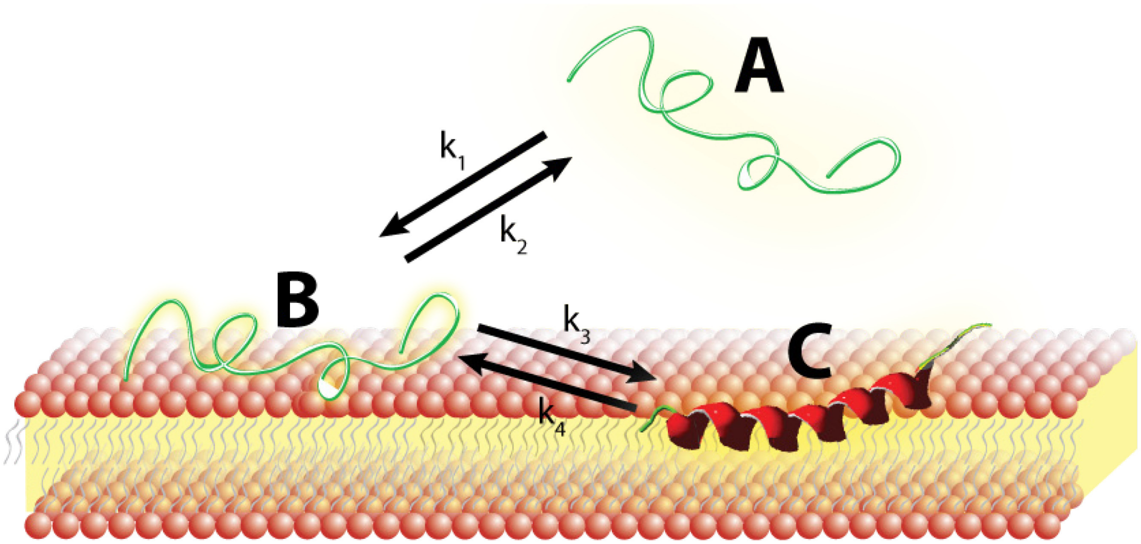

Figure 1.12 Illustration of the consecutive three-state reversible kinetics system for a soluble membrane-active peptide. The peptide exists as a random coil in solution, which first interacts weakly with the bilayer before folding into an alpha-helix.

$$\partial A/_{\partial t} = -k_1 A(t)\lambda^{-1} + k_2 B(t)\lambda^{-1}$$

$$\partial B/_{\partial t} = k_1 A(t) - (k_2 + k_3)B(t) + k_4 C(t) \qquad [1.7]$$

$$\partial C/_{\partial t} = k_3 B(t) - k_4 C(t)$$

where λ^{-1} is the ratio of the area of the interface to the volume of solution in the system. This analysis confirms that the histogram of event lengths will be bi-exponential and shows that the relationships between the histogram measured parameters and the microscopic rates are surprisingly simple (though nontrivial). The analysis allows the interpretation of the molecular count versus solution concentration-isotherm data to determine the heterogeneous solution/interface binding rate.

1.7 References

(1) Shneiderman, B. In *NSF & EC Meeting on Human-Computer Interaction Research Agenda*; Toulouse, France, 1999.

(2) Singer, S. J.; Nicolson, G. L. *Science* **1972**, *175*, 720.

(3) Anglin, T. C.; Conboy, J. C. *Biophysical Journal* **2008**, *95*, 186.

(4) Marsh, D. *CRC Handbook of Lipid Bilayers*; CRC Press: Boca Raton, Fla., 1990.

(5) Duzgunes, N.; Paiement, J.; Freeman, K. B.; Lopez-Straubinger, N. G.; Wilschut, J.; Papahadjopoulos, D. *Biochemistry* **1984**, *23*, 3486.

(6) Charitat, T.; Bellet-Amalric, E.; Fragneto, G.; Graner, F. *The European Physical Journal B - Condensed Matter and Complex Systems* **1999**, *8*, 583.

(7) Alberts, B. *Essential Cell Biology : An Introduction to the Molecular Biology of the Cell*; Garland Pub.: New York, 1998.

(8) Alberts, B. *Molecular Biology of the Cell*; 4th ed.; Garland Science: New York, 2002.

(9) Purves, W. K. *Life, the Science of Biology*; 5th ed.; Sinauer Associates ;
W.H. Freeman: Sunderland, Mass.
Salt Lake City, Utah, 1998.

(10) Reece, J. B.; Campbell, N. A. *Campbell Biology / Jane B. Reece ... [et al.]*; 9th ed.; Benjamin Cummings / Pearson: Boston, 2011.

(11) Mayer, L. D.; Bally, M. B.; Hope, M. J.; Cullis, P. R. *Journal of Biological Chemistry* **1985**, *260*, 802.

(12) Mayer, L. D.; Bally, M. B.; Cullis, P. R. *Biochimica et Biophysica Acta, Biomembranes* **1986**, *857*, 123.

(13) Petre, C. E.; Dittmer, D. P. *International Journal of Nanomedicine* **2007**, *2*, 277.

(14) Reza Mozafari, M.; Johnson, C.; Hatziantoniou, S.; Demetzos, C. *Journal of Liposome Research* **2008**, *18*, 309.

(15) Barani, H.; Montazer, M. *Journal of Liposome Research* **2008**, *18*, 249.

(16) Ashkin, A.; Dziedzic, J. M.; Bjorkholm, J. E.; Chu, S. *Optics Letters* **1986**, *11*, 288.

(17) Ashkin, A. *Proceedings of the National Academy of Sciences* **1997**, *94*, 4853.

(18) Ashkin, A.; Dziedzic, J. *Science* **1987**, *235*, 1517.

(19) Ashkin, A.; Dziedzic, J. M.; Yamane, T. *Nature* **1987**, *330*, 769.

(20) Ajito, K.; Torimitsu, K. *Lab on a Chip* **2002**, *2*, 11.

(21) Svoboda, K.; Schmidt, C. F.; Schnapp, B. J.; Block, S. M. *Nature* **1993**, *365*, 721.

(22) Wilson, E. B.; Decius, J. C.; Cross, P. C. *Molecular Vibrations : The Theory of Infrared and Raman Vibrational Spectra*; Dover Publications: New York, 1980.

(23) Smith, E.; Dent, G. *Modern Raman Spectroscopy : A Practical Approach*; J. Wiley: Hoboken, NJ, 2005.

(24) Brakenhoff, G. J.; Blom, P.; Barends, P. *Journal of Microscopy* **1979**, *117*, 219.

(25) Williams, K. P. J.; Pitt, G. D.; Batchelder, D. N.; Kip, B. J. *Applied Spectroscopy* **1994**, *48*, 232.

(26) Strang, G. *Introduction to Linear Algebra*; 4th ed.; Wellesley-Cambridge Press: Wellesley, MA, 2009.

(27) Albrecht, M. G.; Creighton, J. A. *Journal of the American Chemical Society* **1977**, *99*, 5215.

(28) Jeanmaire, D. L.; Van Duyne, R. P. *Journal of Electroanalytical Chemistry and Interfacial Electrochemistry* **1977**, *84*, 1.

(29) Lai, E. P. C.; Harris, J. M. *Canadian Journal of Applied Spectroscopy* **1992**, *37*, 161.

(30) Melveger, A. J. *Resonance Raman Spectroscopy as an Analytical Tool*; Franklin Institute Press: Philadelphia, 1978.

(31) Axelrod, D.; Hellen, E. H.; Fulbright, R. M. *Topics in Fluorescence Spectroscopy* **1992**, *3,* 289.

(32) Hansen, W. N. *Journal of the Optical Society of America* **1968**, *58*, 380.

(33) Schneckenburger, H. *Current Opinion in Biotechnology* **2005**, *16*, 13.

(34) Axelrod, D. *The Journal of Cell Biology* **1981**, *89*, 141.

(35) Axelrod, D. *Journal of Biomedical Optics* **2001**, *6*, 6.

(36) Wayment, J. R.; Harris, J. M. *Analytical Chemistry* **2008**, *81*, 336.

(37) Fox, C. B.; Wayment, J. R.; Myers, G. A.; Endicott, S. K.; Harris, J. M. *Analytical Chemistry* **2009**, *81*, 5130.

(38) Chao, J.; Ward, E. S.; Ober, R. J. *Proceedings of SPIE* **2012**, *8227*, 82271P/1.

(39) Peterson, E. M.; Harris, J. M. *Analytical Chemistry* **2010**, *82*, 189.

(40) Ambrose, W. P.; Goodwin, P. M.; Martin, J. C.; Keller, R. A. *Physical Review Letters* **1994**, *72*, 160.

(41) Gensch, T.; Böhmer, M.; Aramendía, P. F. *Journal of Physical Chemistry A* **2005**, *109*, 6652.

(42) Lu, H. P.; Xie, X. S. *Nature* **1997**, *385*, 143.

(43) Yip, W.-T.; Hu, D.; Yu, J.; Bout, D. A. V.; Barbara, P. F. *Journal of Physical Chemistry A* **1998**, *102*, 7564.

(44) Wieprecht, T.; Apostolov, O.; Beyermann, M.; Seelig, J. *Journal of Molecular Biology* **1999**, *294*, 785.

CHAPTER 2

CONFOCAL RAMAN MICROSCOPY OF PH - GRADIENT-BASED 10 THOUSAND-FOLD PRECONCENTRATION OF COMPOUNDS WITHIN INDIVIDUAL, OPTICALLY TRAPPED PHOSPHOLIPID VESICLES

Adapted with permission from: Grant A. Myers and Joel M. Harris, *Confocal Raman Microscopy of pH-Gradient-Based 10 000 -Fold Preconcentration of Compounds within Individual, Optically Trapped Phospholipid Vesicles*, Analytical Chemistry, **2011**, 83 (15), pp 6098-6105, American Chemical Society

2.1 Introduction

Phospholipid vesicle (or liposome) encapsulation is an active area of research, with applications ranging from textiles,[1] to food science,[2] and pharmaceuticals.[3,4] These applications benefit from the capability of phospholipid vesicles to provide stable and efficient encapsulation of compounds in their interior. An effective method for encapsulation of ionizable compounds involves establishment of a strong proton or other ion-activity[3,5] differences between the vesicle interior and the surrounding solution. The pH-gradient encapsulation technique has been applied to several successful liposomal drug formulations.[6] The technique exploits the semi-permeable character of phospholipid bilayers, where a small, neutral molecule can permeate the vesicle membrane, while its ionized (protonated or deprotonated) counterpart cannot.

For neutral, basic compounds that are ionized at a low pH, for example, the ratio of the protonated form of the compound inside versus outside the vesicle can approach the ratio of proton activities inside versus outside the vesicle.[7,8] Therefore, a pH gradient of 3 units could drive a 1000-fold increase in concentration of a compound within a vesicle compared to the surrounding solution. While this strategy is useful in designing efficient encapsulation of drugs or other payloads within vesicles, the large increase in concentration in the small volume of a vesicle suggests a preconcentration scheme for detection of trace-level compounds. An ionizable analyte present in solution at low concentrations could be driven by a pH gradient into the interior of a vesicle where it could be selectively detected at much higher concentrations.

Past investigations of pH-gradient loading have relied on characterization of bulk liposome suspensions using ex situ measurement techniques. For example, following separation of vesicles in suspension from residual free compound in solution, vesicles are lysed with detergent, and the concentration of the encapsulated compound is measured by absorption spectroscopy[9] or by a radiolabel.[10] This methodology has been sufficient for the development of drug formulations, where the goal is simply to produce a stable liposome suspension encapsulating a large fraction of the available drug. To take advantage of the much higher concentration of a compound entrapped within a vesicle for the purpose of enhanced detection, one needs to have a micro-scale measurement technique that can selectively probe the solution composition within a vesicle. Optical-trapping confocal Raman microscopy[11-14] is capable of characterizing the structure and contents of individual μm- and sub-μm-sized phospholipid vesicles.[15-20] This method has been successfully employed to characterize the membrane permeability and localization of compounds within phospholipid vesicles and to determine concentrations of compounds inside vesicles without the use of fluorescent or radioactive labels.[15,18] It has also been applied to the study of liquid-liquid extraction of hydrophobic compounds into organic-solvent droplets dispersed in water.[21]

In this work, optical-trapping confocal Raman microscopy is used to detect and quantify analytes concentrated within individual vesicles by pH-gradient loading. The method is nearly ideal for this purpose because the collection of Raman scattering is constrained by confocal optics to a small volume that can be entirely filled with a vesicle under investigation. Design of the experiment is based on the relevant acid-base equilibria of the analyte and buffers, which define the limits of preconcentration arising from depletion of the bulk solution concentration and the buffer capacity within a vesicle. To characterize the preconcentration of a compound inside an individual vesicle, optical-trapping is used to manipulate a vesicle into and out of external solutions of varying pH and analyte concentrations. The model analyte compound used in this study is N-benzyl, N-N-dimethylamine (BDMA), which incorporates both a weak-base tertiary amine and an aromatic ring, the latter serving as a Raman-scattering reporter group. A multidimensional least squares analysis is used to quantify both lipid, BDMA, and a perchlorate-ion internal standard within the vesicle. The model for preconcentration based on acid-base equilibria is compared to experimental results, and achievement of a 10^4-fold concentration enhancement is reported.

2.2 Theory

2.2.1 Fundamental equations

The basis of pH-gradient loading of an analyte into a vesicle is the acid-base equilibria[7,8] for the ionization of the analyte both inside and outside the vesicle:

$$K_A = \frac{\gamma_{H^+_{in}}[H^+]_{in}\,\gamma_{A_{in}}[A]_{in}}{\gamma_{HA^+_{in}}[HA^+]_{in}} = \frac{\gamma_{H^+_{out}}[H^+]_{out}\,\gamma_{A_{out}}[A]_{out}}{\gamma_{HA^+_{out}}[HA^+]_{out}} \qquad [2.1]$$

where $[A]$ is the concentration of a neutral amine in this example, $[HA^+]$ is the concentration of its conjugate acid, K_A is the acid dissociation constant, and γ is the activity coefficient of a given species. If the neutral form of the analyte is membrane permeable, then the equilibrium condition coupling the two compartments is that the activity of the neutral form of the compound is the same inside and outside of the vesicle:

$$\gamma_{A_{in}}[A]_{in} = \gamma_{A_{out}}[A]_{out} \qquad [2.2]$$

It will be assumed that the activity coefficients of the analyte species are equivalent inside and outside the vesicle, although this assumption will be revisited in the comparison between model predictions and experimental results. Neglecting activity coefficients, Equations 2.1 and 2.2 can be combined to predict the total concentration of analyte within a vesicle at equilibrium, which depends on the hydrogen ion activities inside and outside the vesicle relative to the acid disassociation constant of the protonated amine:

$$[A]_{in}^{total} = [HA^+]_{in} + [A]_{in} = \frac{[H^+]_{in} + K_A}{[H^+]_{out} + K_A}\left([HA^+]_{out} + [A]_{out}\right) = \frac{[H^+]_{in}}{[H^+]_{out} + K_A}[A]_{out}^{total} \quad [2.3]$$

The acid dissociation constant term in the numerator can also be neglected, because under typical loading conditions $[H^+]_{in} >> K_{A.}$ This equation demonstrates the principle of pH-gradient loading, where a low pH inside the vesicle and high pH outside the vesicle leads to a large buildup of $[HA^+]$ inside the vesicle, transferred from the source phase until the activities (concentrations) of the membrane-permeable, neutral form of the analyte inside and outside of the vesicle are equal; see in Figure 2.1.

Dividing the numerator and denominator of the right side of Equation 2.3 by K_A and taking the log of the hydrogen ion activity and the acid disassociation constant gives the enrichment factor (E), or the ratio of the total concentrations of the analyte inside and outside the vesicle, versus the pH of the source phase:

$$E = [A]_{in}^{total} / [A]_{out}^{total} = \frac{10^{pK_A - pH_{in}}}{1 + 10^{pK_A - pH_{out}}} \quad [2.4]$$

The analyte enrichment versus source-phase pH takes the form of a generalized logistic function; see Figure 2.2. The upper limit of the enrichment, at a source-phase pH much greater than the pK_A of the analyte, is given by the numerator, which is the ratio of the proton activity inside the vesicle to the acid disassociation constant of the analyte. The inflection point at half the maximum enrichment occurs when the source-phase pH equals the pK_A of the analyte (Figure 2.2A).

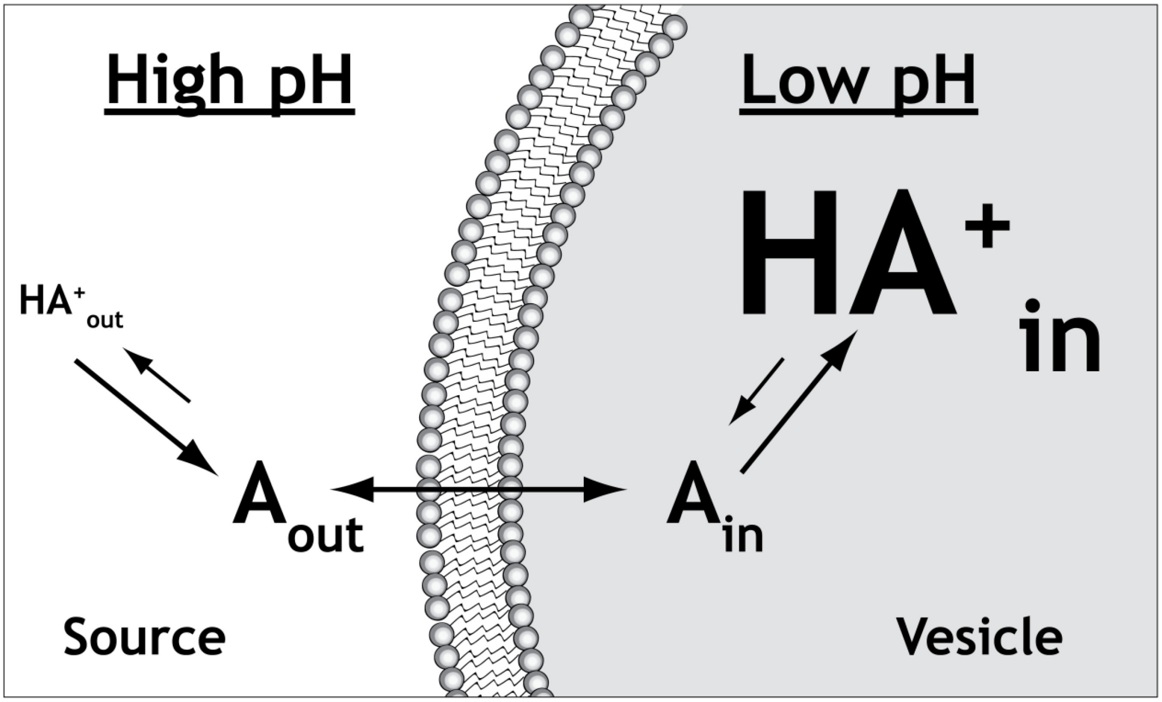

Figure 2.1: Schematic of pH-gradient loading of an ionizable analyte inside of a phospholipid vesicle. The neutral form of the basic analyte compound can permeate the phospholipid membrane, while the protonated form of the analyte cannot. At equilibrium, the activity of the membrane-permeable neutral form is equivalent inside and outside of the vesicle. The pH gradient will lead to accumulation of the protonated form of the analyte inside of the vesicle.

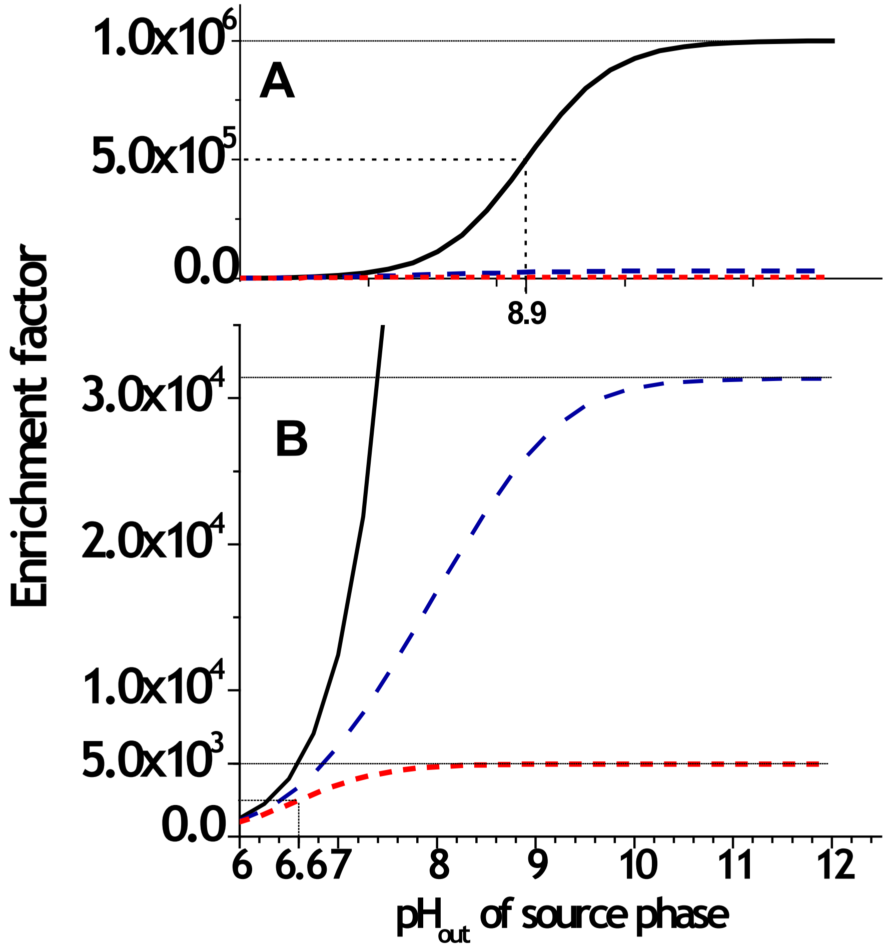

Figure 2.2: Predictions of pH-gradient driven analyte enrichment relative to the total concentration of analyte in the sample, plotted on two vertical scales. The initial pH inside of the vesicle is 2.9 and the pK_A of the analyte is 8.9. The solid black curve is from Equation 2.4, which neglects the buffering capacity and source-phase depletion. The dashed blue curve accounts for buffer capacity in the vesicle for a 0.5-M citrate buffer with 15-µM analyte in the source phase from a solution to the 6th-order polynomial in Figure 2.3. The dotted red curve accounts for depletion of analyte from the source phase (Equation 2.8), where the vesicle volume fraction is 2×10^{-4}, typical of extruded vesicle dispersions.

While Equation 2.4 should accurately predict the ratio of the analyte concentration inside versus outside a vesicle for a given pH gradient, the concentration of analyte inside a vesicle relative to the *original* concentration in the source phase and the *initial* pH gradient is limited by two additional constraints that are not addressed in Equation 2.4. First, the concentration of the analyte in the source phase at equilibrium, $[A]_{\mathrm{out}}$, may be depleted by its transfer to the interior volumes of many vesicles in the sample. Indeed, in liposomal drug preparation, it is desirable to generate high encapsulation efficiencies, where more than 90% of a compound can be transferred to the inside of vesicles at equilibrium.[3] For analytical applications, source-phase depletion can limit the enrichment relative to the initial analyte concentration and degrade the sensitivity of detection within vesicles. A second constraint that can reduce enrichment is the finite capacity of the buffer within the vesicle, where the interior pH may change significantly from its initial value after a large concentration of an analyte accumulates in the vesicle interior and titrates the buffer.[8] These two processes can be addressed by expanding the system of equations to account for the mass balance of the analyte and the finite buffering of the vesicle interior.

2.2.2 Source-phase depletion

A mass-balance equation accounting for the total number of moles of analyte inside and outside of vesicles can be included in the system of equations to determine the depletion of analyte from the source phase:

$$V_{total}[A]_{total} = V_{in}[A]_{in}^{total} + V_{out}[A]_{out}^{total} \qquad [2.5]$$

where $\boldsymbol{V}$ represents the respective volumes, and $[\boldsymbol{A}]_{\text{total}}$ represents the concentration of analyte in the entire volume. Dividing both sides of this equation by the total volume and using that result to eliminate the term for the total concentration of analyte in the source phase in Equation 2.3 gives a prediction of the concentration of analyte within the vesicles in terms of known quantities after simplification:

$$[A]_{in}^{total} = \frac{[H^+]_{in} + K_A}{[H^+]_{out} + K_A + [H^+]_{in} F_{in}^{V} - [H^+]_{out} F_{in}^{V}} [A]_{total} \qquad [2.6]$$

Under typical conditions for loading the protonated form of weak base in the vesicle, $[H^+]_{in} >> K_A$, $[H^+]_{in} >> [H^+]_{out}$, Equation 2.6 simplifies to the following:

$$[A]_{in}^{total} = \frac{[H^+]_{in}}{[H^+]_{out} + K_A + [H^+]_{in} F_{in}^{V}} [A]_{total} \qquad [2.7]$$

which differs from Equation 2.3 by substitution of the concentration of analyte outside of vesicles for the total concentration analyte in the sample and by the vesicle-volume fraction included in the denominator.

This equation can be rearranged to predict the enrichment of analyte within vesicles while accounting for depletion of the analyte from the source phase:

$$E = [A]_{in}^{total} / [A]_{total} = \frac{10^{p\kappa - pH_{in}}}{1 + 10^{p\kappa - pH_{out}}} \qquad [2.8]$$

where $\kappa = K_A + [H^+]_{in} F_{in}^V$ and $p\boldsymbol{\kappa} = -\log_{10}(\boldsymbol{\kappa})$. When the vesicle volume fraction is negligible, Equation 2.8 is equivalent to Equation 2.4. When the vesicle volume fraction is large and dominates $\boldsymbol{\kappa}$, depletion of the analyte from the source phase is significant and the maximum enrichment factor is equal to the inverse of the vesicular volume fraction. Under these conditions, the source phase pH that produces 50% of the maximum enrichment of the analyte is given by the pH of the vesicle interior minus the log of the vesicle volume fraction. As an example, the dotted red curve in Figure 2.2B represents the enrichment factor as a function of the pH of the source phase where the interior pH of the vesicle is 2.9, the pK_A of the analyte is 8.9 and the vesicle volume fraction F_{in}^V is 2×10^{-4}, typical of extruded vesicle preparations used in microscopy analysis. For this example, the maximum enrichment is $1/F_{in}^V = 5 \times 10^3$, and the source phase pH at half maximum enrichment is: $pH_{in} - \log(F_{in}^V) = 6.6$, as noted on the y- and x-axes of Figure 2.2B.

These results illustrate that even small vesicle volume fractions can lead to source-phase depletion and inhibit the potential analyte enrichment to be realized by pH gradient vesicle loading. Furthermore, under conditions where enrichment is limited by source-phase depletion, the magnitude of enrichment and resulting sensitivity in measurement depends on the vesicle volume fraction. The solution volume encapsulated by vesicles is difficult to control from one preparation to the next, especially for extruded vesicles larger than 100 nm in diameter, where significant polydispersity in size and lamellarity is observed.[22] Thus, the average vesicle size and total amount of lipid used to prepare the dispersion cannot reliably be used to accurately estimate the vesicle volume fraction. A possible solution to this problem would be to dilute the vesicles into a large source-phase volume so that depletion is insignificant. While this would reduce the vesicle volume fraction, it requires a large volume of source solution and also creates a tedious problem of locating a vesicle for measurement in the dilute dispersion. In the present work, the depletion issue is addressed by optical trapping of vesicles and manipulating them into a vesicle-free solution, which allows the analyte accumulation of a *single* vesicle to be characterized, isolated from other vesicles in the system.

2.2.3 Vesicle buffer capacity

Even in the absence of source-phase depletion, a second constraint that can limit enrichment is the finite capacity of the buffer within the vesicle, where the interior pH may change significantly from its initial value as the accumulated analyte concentration approaches that of the buffer.[8] To account for the pH change due to accumulation of the analyte, the acid/base equilibria of the buffer must be included in the system of equations. For example, for a citric acid buffer within the vesicle, three acid dissociation equilibria are needed:

$$K_1 = \frac{[H^+]_{in}[H_2B^-]}{[H_3B]} \qquad [2.9a]$$

$$K_2 = \frac{[H^+]_{in}[HB^{2-}]}{[H_2B^-]} \qquad [2.9b]$$

$$K_3 = \frac{[H^+]_{in}[B^{3-}]}{[HB^{2-}]} \qquad [2.9c]$$

where pK$_1$ = 3.14, pK$_2$ = 4.78, and pK$_3$ = 5.29 and the total buffer concentration is given by:

$$[B]_{in}^{total} = [H_3B] + [H_2B^-] + [HB^{2-}] + [B^{3-}] \qquad [2.10]$$

The citric acid buffer used to hydrate the vesicles has been titrated with small quantities of strong base (sodium hydroxide) to set the desired initial pH of the interior buffer. From the equilibria in Equations 2.9 a – c and the initial pH giving $[H^+]_0$, the sodium ion concentration in the buffer can be determined:

$$[Na^+] = \frac{[H^+]_0^3[B]_{in}^{tot}K_1 + 2[H^+]_0^2[B]_{in}^{tot}K_1K_2 + 3[H^+]_0^2[B]_{in}^{tot}K_1K_2K_w + K_w\beta - [H^+]_0^2\beta}{[H^+]_0\beta} \qquad [2.11]$$

where $\beta = [H^+]^3 + [H^+]^2K_1 + [H^+]K_1K_2 + K_1K_2K_3$. As neutral analyte molecules pass through the vesicle membrane and are protonated to form HA$^+$, protons are released from the acidic forms of the buffer to compensate; no charge passes through the membrane so the internal charge in the vesicle is conserved. A conservation-of-charge constraint includes the ions in the vesicle interior and accounts for acid-base reactions:

$$[HA^+]_{in} + [H^+]_{in} + [Na^+] = [H_2B^-] + 2[HB^{2-}] + 3[B^{3-}] + [OH^-]_{in} \qquad [2.12]$$

where

$$[OH^-]_{in} = K_w \,/\, [H^+]_{in} \qquad [2.13]$$

In total, there are 10 independent equations (Equations 2.1, 2.2, 2.5, 2.9 a - c, 2.10-2.13) and 10 unknown concentrations, constrained by five equilibrium constants (3 buffer pK_a's, the analyte pK_a and the autoprotolysis constant of water), and five parameters determined by conditions of the experiment, including the concentration of the vesicle buffer, its initial pH, the vesicle volume fraction, the pH of the source-phase buffer, and the concentration of analyte in the source phase. Five other secondary variables were introduced in other equations; all variables are summarized in Table 2.1. The solution to the system of equations is found by isolating $[H^+]_{in}$, the concentration of protons inside of the vesicle at equilibrium, which occurs in 7 out of 10 of the equations in the system. The strategy is to first solve all the equations for other unknowns in terms of $[H^+]_{in}$. These expressions are then substituted into the charge-balance equation such that the only unknown remaining in the charge balance is for $[H^+]_{in}$. This expression is then solved for $[H^+]_{in}$, and the result is a 6th -order polynomial having only one root that is positive and real; see Figure 2.3. This root, represents a unique, physically meaningful solution to the system of equations and provides the value of $[H^+]_{in}$ at equilibrium, which can be used to determine the enrichment factor, *E*, through Equation 2.6.

As an example, the dashed blue curve in Figure 2.2B represents the enrichment factor that accounts for the capacity of a 0.5-M citrate buffer in vesicles with an initial pH

Table 2.1: Table of Variables

Equation numbers refer to equations in Chapter 2, *i.e.* 2.1, 2.3-4, 2.6-9, 2.12-13 etc.

Unknowns		**Appearing in Equations**
$[H^+]_{in}$	*Equilibrium vesicle proton concentration (also pH_{in})*	**1, 3-4, 6-9, 12-13**
$[OH^-]_{in}$	*Equilibrium vesicle hydroxide concentration*	**12-13**
$[HA^+]_{in}$	*Equilibrium vesicle protonated analyte concentration*	**1, 3**
$[A]_{in}$	*Equilibrium vesicle neutral analyte concentration*	**1-3**
$[HA^+]_{out}$	*Equilibrium source phase protonated analyte concentration*	**1, 3**
$[A]_{out}$	*Equilibrium source phase neutral analyte concentration*	**1-3**
$[H_3B]$	*Equilibrium neutral buffer concentration*	**9a, 10**
$[H_2B^-]$	*Equilibrium monobasic buffer concentration*	**9a-b, 10, 12**
$[HB^{2-}]$	*Equilibrium dibasic buffer concentration*	**9b-c, 10, 12**
$[B^{3-}]$	*Equilibrium tribasic buffer concentration*	**9c, 10, 12**
$[Na^+]$	*Vesicle concentration of sodium ion*	**11-12**
Variables set in experiment		
$[B]^{Tot}$	*Total concentration of vesicle buffer*	**10-11**
$[A]_{Total}$	*Total concentration of analyte in the entire system*	**5-8**
$[H^+]_{out}$	*Source phase concentration of protons(also pH_{out})*	**1, 3-4, 6-8**
$[H^+]_0$	*Initial vesicle concentration of protons*	**11**
F_{in}^V	*Volume fraction of vesicles in system*	**6-8**
Thermodynamic constants and activity coefficients		
K_w	*Equilibrium dissociation constant for water*	**11, 13**
K_A	*Equilibrium dissociation constant for the analyte (also pK_A)*	**1, 3-4, 6-8**
K_1	*First equilibrium dissociation constant for citrate buffer*	**9a, 11**
K_2	*Second equilibrium dissociation constant for citrate buffer*	**9b, 11**
K_3	*Third equilibrium dissociation constant for citrate buffer*	**9c, 11**
$\gamma_{A_{in}}$	*Activity coefficient for neutral analyte inside vesicles*	**1-2**
$\gamma_{A_{out}}$	*Activity coefficient for neutral analyte outside vesicles*	**1-2**
$\gamma_{HA^+_{in}}$	*Activity coefficient for protonated analyte inside vesicles*	**1-2**
$\gamma_{HA^+_{out}}$	*Activity coefficient for protonated analyte outside vesicles*	**1-2**
$\gamma_{H^+_{in}}$	*Activity coefficient for protons inside the vesicles*	**1-2**
$\gamma_{H^+_{out}}$	*Activity coefficient for protons outside the vesicles*	**1-2**
Other variables, unknowns, and placeholders		
	Placeholder for $[A]_{in} + [HA^+]_{in}$	**3-8**
	Placeholder for $[A]_{out} + [HA^+]_{out}$	**4-5**
V_{total}	*Total volume of vesicles and source phase*	**5**
$V_{vesicle}$	*Total volume of all vesicles*	**5**
V_{out}	*Total volume of source phase*	**5**
κ	*Placeholder for* $K_A + [H^+]_{in}$ *(also $p\kappa$)*	**8**
β	*Placeholder for* $[H^+]^3 + [H^+]^2 K_1 + [H^+] K_1 K_2 + K_1 K_2 K_3$	**11**

$$\begin{aligned}
&H_{\mathrm{in}}^{6}F_{\mathrm{in}}^{V} + H_{\mathrm{in}}^{5}\big(-A_{\mathrm{tot}}\big(-1 + F_{\mathrm{in}}^{V}\big) + H_{\mathrm{out}} - F_{\mathrm{in}}^{V}H_{\mathrm{out}} + F_{\mathrm{in}}^{V}K_1 + K_A + F_{\mathrm{in}}^{V}\mathrm{Na}^{+}\big) + \\
&H_{\mathrm{in}}^{4}\big(-B_{\mathrm{in}}^{\mathrm{tot}}F_{\mathrm{in}}^{V}K_1 - A_{\mathrm{tot}}\big(-1 + F_{\mathrm{in}}^{V}\big)K_1 + H_{\mathrm{out}}K_1 - F_{\mathrm{in}}^{V}H_{\mathrm{out}}K_1 + F_{\mathrm{in}}^{V}K_1K_2 + K_1K_A \\
&\qquad - F_{\mathrm{in}}^{V}K_W + H_{\mathrm{out}}\mathrm{Na}^{+} - F_{\mathrm{in}}^{V}H_{\mathrm{out}}\mathrm{Na}^{+} + F_{\mathrm{in}}^{V}K_1\mathrm{Na}^{+} + K_A\mathrm{Na}^{+}\big) + \\
&H_{\mathrm{in}}^{3}\big(-B_{\mathrm{in}}^{\mathrm{tot}}H_{\mathrm{out}}K_1 + B_{\mathrm{in}}^{\mathrm{tot}}F_{\mathrm{in}}^{V}H_{\mathrm{out}}K_1 - 2B_{\mathrm{in}}^{\mathrm{tot}}F_{\mathrm{in}}^{V}K_1K_2 - A_{\mathrm{tot}}\big(-1 + F_{\mathrm{in}}^{V}\big)K_1K_2 \\
&\qquad + H_{\mathrm{out}}K_1K_2 - F_{\mathrm{in}}^{V}H_{\mathrm{out}}K_1K_2 + F_{\mathrm{in}}^{V}K_1K_2K_3 - B_{\mathrm{in}}^{\mathrm{tot}}K_1K_A + K_1K_2K_A \\
&\qquad - H_{\mathrm{out}}K_W + F_{\mathrm{in}}^{V}H_{\mathrm{out}}K_W - F_{\mathrm{in}}^{V}K_1K_W - K_AK_W + H_{\mathrm{out}}K_1\mathrm{Na}^{+} \\
&\qquad - F_{\mathrm{in}}^{V}H_{\mathrm{out}}K_1\mathrm{Na}^{+} + F_{\mathrm{in}}^{V}K_1K_2\mathrm{Na}^{+} + K_1K_A\mathrm{Na}^{+}\big) + \\
&H_{\mathrm{in}}^{2}\big(-2B_{\mathrm{in}}^{\mathrm{tot}}H_{\mathrm{out}}K_1K_2 + 2B_{\mathrm{in}}^{\mathrm{tot}}F_{\mathrm{in}}^{V}H_{\mathrm{out}}K_1K_2 - 3B_{\mathrm{in}}^{\mathrm{tot}}F_{\mathrm{in}}^{V}K_1K_2K_3 \\
&\qquad - A_{\mathrm{tot}}\big(-1 + F_{\mathrm{in}}^{V}\big)K_1K_2K_3 + H_{\mathrm{out}}K_1K_2K_3 - F_{\mathrm{in}}^{V}H_{\mathrm{out}}K_1K_2K_3 \\
&\qquad - 2B_{\mathrm{in}}^{\mathrm{tot}}K_1K_2K_A + K_1K_2K_3K_A - H_{\mathrm{out}}K_1K_W + F_{\mathrm{in}}^{V}H_{\mathrm{out}}K_1K_W \\
&\qquad - F_{\mathrm{in}}^{V}K_1K_2K_W - K_1K_AK_W + H_{\mathrm{out}}K_1K_2\mathrm{Na}^{+} - F_{\mathrm{in}}^{V}H_{\mathrm{out}}K_1K_2\mathrm{Na}^{+} \\
&\qquad + F_{\mathrm{in}}^{V}K_1K_2K_3\mathrm{Na}^{+} + K_1K_2K_A\mathrm{Na}^{+}\big) + \\
&H_{\mathrm{in}}\big(-3B_{\mathrm{in}}^{\mathrm{tot}}H_{\mathrm{out}}K_1K_2K_3 + 3B_{\mathrm{in}}^{\mathrm{tot}}F_{\mathrm{in}}^{V}H_{\mathrm{out}}K_1K_2K_3 - 3B_{\mathrm{in}}^{\mathrm{tot}}K_1K_2K_3K_A \\
&\qquad - H_{\mathrm{out}}K_1K_2K_W + F_{\mathrm{in}}^{V}H_{\mathrm{out}}K_1K_2K_W - F_{\mathrm{in}}^{V}K_1K_2K_3K_W - K_1K_2K_AK_W \\
&\qquad + H_{\mathrm{out}}K_1K_2K_3\mathrm{Na}^{+} - F_{\mathrm{in}}^{V}H_{\mathrm{out}}K_1K_2K_3\mathrm{Na}^{+} + K_1K_2K_3K_A\mathrm{Na}^{+}\big) - \\
&H_{\mathrm{out}}K_1K_2K_3K_W + F_{\mathrm{in}}^{V}H_{\mathrm{out}}K_1K_2K_3K_W - K_1K_2K_3K_AK_W
\end{aligned}$$

Figure 2.3: The roots of this sixth order polynomial in H_{in} are solutions to the system of ten equations, numbers 2.1-2, 2.5, 2.9a-c, and 2.10-13. This expression contains a single unknown, H_{in}, five equilibrium constants, $K_{1\text{-}3}$, K_A, and K_w, and five parameters set in the experiment, A_{tot}, $F_{in}{}^{V}$, H_{out}, Na^+, and B_{in}^{tot}.

of 2.9, a pK_A value of 8.9, a concentration of analyte in the source phase of 15 μM, and an infinitesimal vesicle volume fraction. At equilibrium after the analyte accumulates in the vesicle, the pH inside the vesicle increases from 2.9 up to ~ 4.4. Under these conditions, the maximum enrichment factor is $\sim 3\times10^4$, corresponding to an analyte concentration in the vesicle of ~470 mM, or approximately 94% of the concentration of the citrate buffer.

In summary, Figures 2.2A and 2.2B show that under typical experimental conditions, both buffer capacity and source-phase depletion can significantly limit the accumulation of analyte inside of vesicles. The maximum estimated enrichments when accounting for buffering and depletion are two to three orders of magnitude smaller than the estimated enrichment neglecting those factors. With a goal of an experiment to produce a very high preconcentration of an analyte inside phospholipid vesicles, theory suggests that the pH gradient, the pKa of the analyte and the concentration of buffer inside the vesicle should be as large as possible, while the vesicle volume fraction should be as small as possible. Following these guidelines, an experiment is designed to test this concept and achieve high enrichment factors through pH gradient loading of optically trapped phospholipid vesicles.

2.3 Materials and Methods

2.3.1 Materials

Buffers were prepared from citric acid monohydrate, and monobasic sodium phosphate, boric acid and sodium chloride titrated to the desired pH with sodium hydroxide, all from Malinckrodt (Paris, KY), diluted into 18 MΩ·cm double-distilled water filtered with a Barnstead (Boston, MA) NANOpure II system. Sodium perchlorate from Sigma-Aldrich (St. Louis, MO) was added to the vesicle buffer as an internal Raman scattering standard. The concentration of sodium chloride required in the source phase buffer to match the osmolarity of the vesicle buffer was estimated using CurTiPot 3.3.2, which implements low-level activity approximations; www2.iq.usp.br/docente/gutz/Curtipot_.html. N-benzyl, N-N-dimethylamine (BDMA) was purchased from Sigma (St. Louis, MO) and dipalmitoyl-phosphatidyl-choline (DPPC) from Avanti Polar Lipids (Alabaster, AL). Phospholipid vesicles containing citrate/perchlorate buffer were extruded following the procedure detailed elsewhere,[15] where 1mg/mL lipid solutions were subjected to at least four freeze/thaw cycles before extrusion through a single 0.6-µm pore-size polycarbonate track etch filter from Nucleopore (Pleasanton, CA). A freeze/thaw cycle consisted of heating the lipid solution above the transition temperature in a water bath followed by submersion and stirring in liquid nitrogen until solid. Immediately after extrusion, vesicles were diluted by a factor of 300-600 in an osmotically-matched phosphate/borate/sodium chloride buffer solution to establish the pH gradient. All experiments were performed at room temperature, ~22° C.

2.3.2 Confocal Raman microscopy

The optical-trapping confocal Raman microscope has been described elsewhere.[18] Briefly, the 647.1 nm laser line from a Krypton-ion laser is focused through a beam expander to back-fill the 100x oil immersion objective in a Nikon T100 inverted microscope frame. Approximately 20 mW of laser power through the microscope focus are sufficient to optically trap and manipulate phospholipid vesicles in the sample, which are located through the eyepiece of the microscope with illumination from an overhead condenser. Raman scattering from the sample is collected back through the same microscope objective, filtered and focused onto the entrance slit of a three-quarter-meter Chromex monochromator (Billerica, MA), where the slit acts as the confocal aperture in the horizontal dimension. The spectrum dispersed by the monochromator is imaged with a water-cooled Andor CCD camera (South Winsdor, CT) where the confocal aperture in the vertical dimension is defined by restricting the collection to three pixel rows, which are binned together by the camera controller.

The Raman-shift axis was calibrated daily using an acetonitrile/toluene mixture and peak assignments[23] established by ASTM E1840-96 with a cubic-order polynomial interpolation. To limit the fluorescent background associated with the coverslip glass, Raman scattering was collected at a distance of ~15 μm from the coverslip surface. All spectra were processed in a MATLAB (The MathWorks Inc., Natick, MA) environment, where a dark background spectrum was first subtracted (no light passed to the monochromator) to eliminate the detector offset. Next, a spectrum acquired of the tungsten source from the overhead bright-field illuminator was used to remove the wavelength-dependent modulations in the detector sensitivity. The Raman spectra were flat-field corrected for the CCD wavelength-dependent response by taking the ratio to the spectrum of the tungsten source. The tungsten source exhibited a fall-off in intensity between 750 and 800 nm, which was corrected by fitting the tungsten source spectrum to a 10th-order polynomial and multiplying the flat-fielded spectrum by this smooth polynomial to remove the intensity bias at longer wavelengths. As an example, a raw spectrum as collected by the CCD is plotted in Figure 2.4A, while the dark-spectrum and

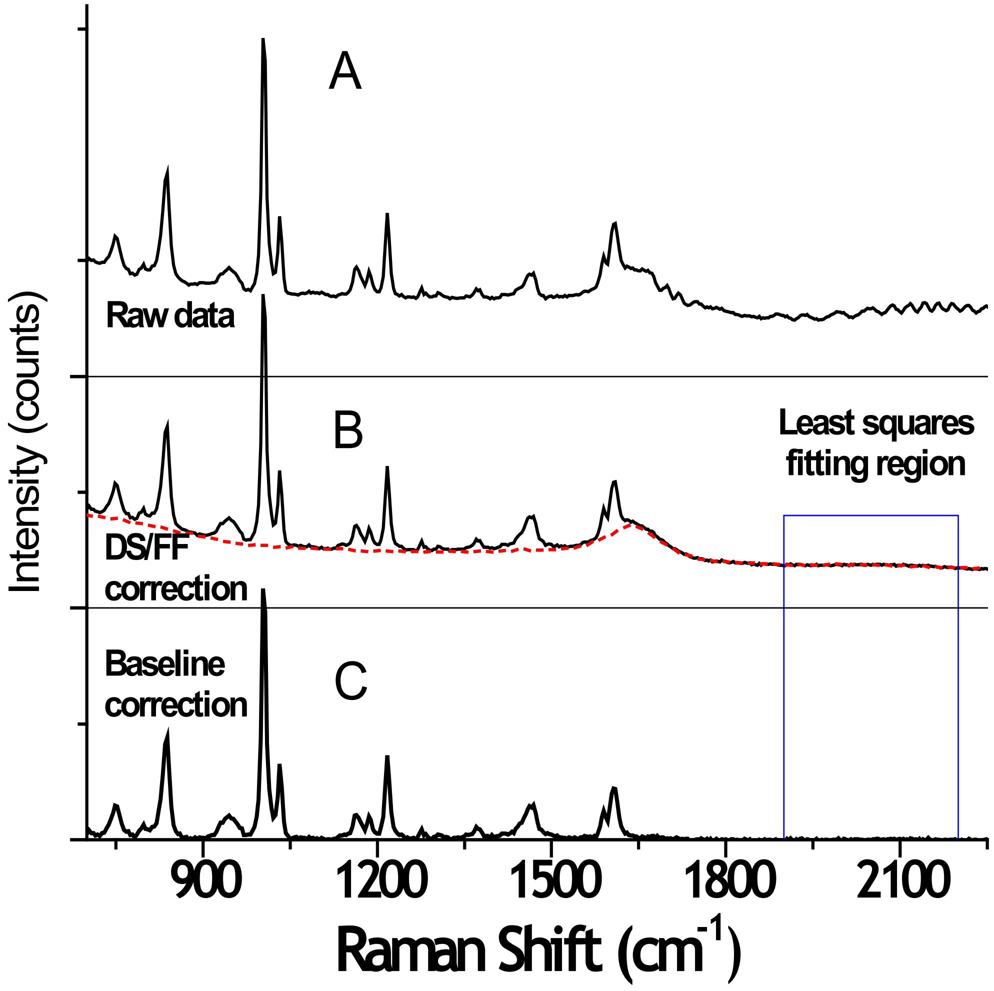

Figure 2.4: Corrections performed on a Raman spectrum of 250-mM BDMA solution acidified with HCl. A. Raw data collected from the CCD. B. Solid line shows the results of dark spectrum (DS) and flat-field (FF) correction. The dashed red line is the water background spectrum, scaled to the BDMA data in the region indicated. C. BDMA Raman spectrum following water baseline-correction.

flat-field corrected data are plotted as the solid line in Figure 2.4B. Occasional cosmic ray events were corrected by replacing their intensity with the average of the intensity of adjacent pixels.

Prior to least-squares analysis, the Raman spectra need to be baseline corrected for so that the peak intensities can be interpreted quantitatively. Typically, this is done by fitting the baseline in regions between peaks to a polynomial, which is then subtracted from the data; this approach is largely subjective and can lead to errors in peak intensities that propagate into the subsequent quantitative analysis. A more objective and stable approach is employed in this work, where a background spectrum of pure water is used for baseline correction; the water spectrum was scaled and subtracted from a given spectrum until the squared residuals in the quiet region between 1900 and 2200 cm^{-1} were minimized. This is shown in Figure 2.4B, where the fitting region used to scale the water background spectrum is noted, and the results after subtraction are plotted in Figure 2.4C. The result is a baseline-corrected spectrum that accurately eliminates the water bending-mode scattering near 1600 cm^{-1} as well the broad background between 300 and 1500 cm^{-1}. This water-baseline correction does not produce significant negative intensity across the region of interest, which is critical for accurate analysis of components in the data.

The sample cell is constructed with a solution well coupled to a 140-μm x ~500-μm channel, used to store vesicles while the solution in the well is changed; see Figure 2.5. After introduction of vesicle solution through the injection port, the solution in the well is emptied and rinsed, while the narrow width of the channel preserves the solution of vesicles in the channel. After a source-phase solution is added to the well, a

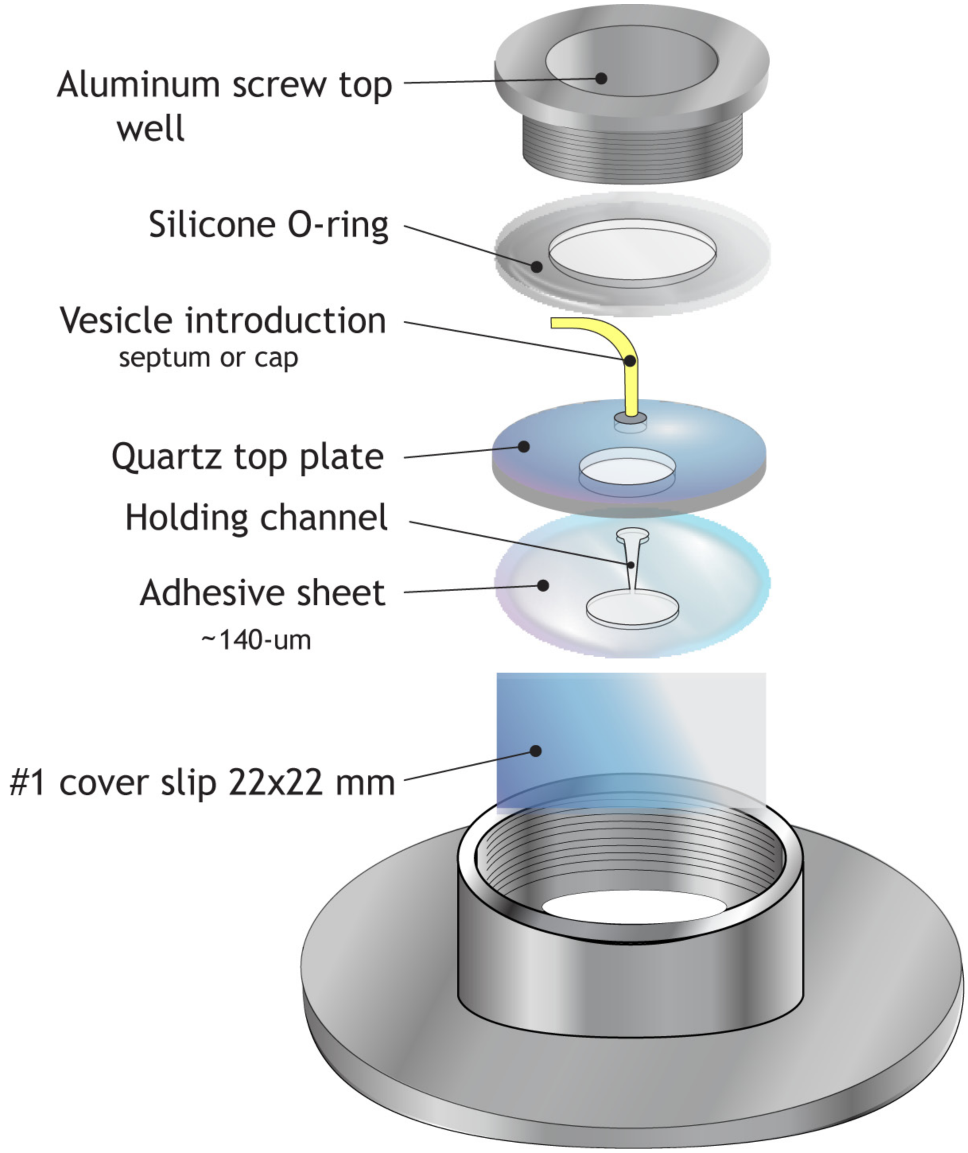

Figure 2.5: Exploded diagram of the confocal-Raman sample cell. The sample cell is built by sandwiching patterned-cut double-coated polyester adhesive tape (9495 MPF from 3M, St. Paul, MN) between a #2 coverslip and a quartz top plate having two drilled holes.

single vesicle is selected in the holding channel, optically trapped, and moved down the channel and into the well by translating the microscope stage as in Figure 2.6. After a measurement has been completed, the vesicle is returned to the holding channel via the optical trap and the well is emptied, rinsed and refilled with the next source-phase solution, while the original vesicle remains optically trapped so that the measurement can be repeated on the same vesicle. A similar 'dead-volume' zone approach has been employed in a microfluidics channel, where optically trapped DNA could be stored and then introduced into solutions to study their unfolding behavior under various solution conditions.[24]

2.4 Results and Discussion

2.4.1 Quantitative analysis of vesicle contents

Raman spectra were acquired from standard solutions of the aqueous citrate buffer, source-phase phosphate/borate/sodium chloride buffer, sodium perchlorate, BDMA, and 0.6-μm diameter extruded DPPC vesicles, using a minimum integration time of 10 minutes. After background and baseline correction, the spectra were normalized by concentration and integration time, except for the DPPC vesicle standard spectrum, which has an unknown lipid concentration. The corrected and normalized standard spectra are presented in Figure 2.7. From these results, it is evident that the spectra have significant peak overlap, which makes it necessary to incorporate all of the components into a least squares model for quantitative analysis. Fortunately, the spectrum of each component is known, and they do not exhibit significant changes due to chemical interactions when mixed together

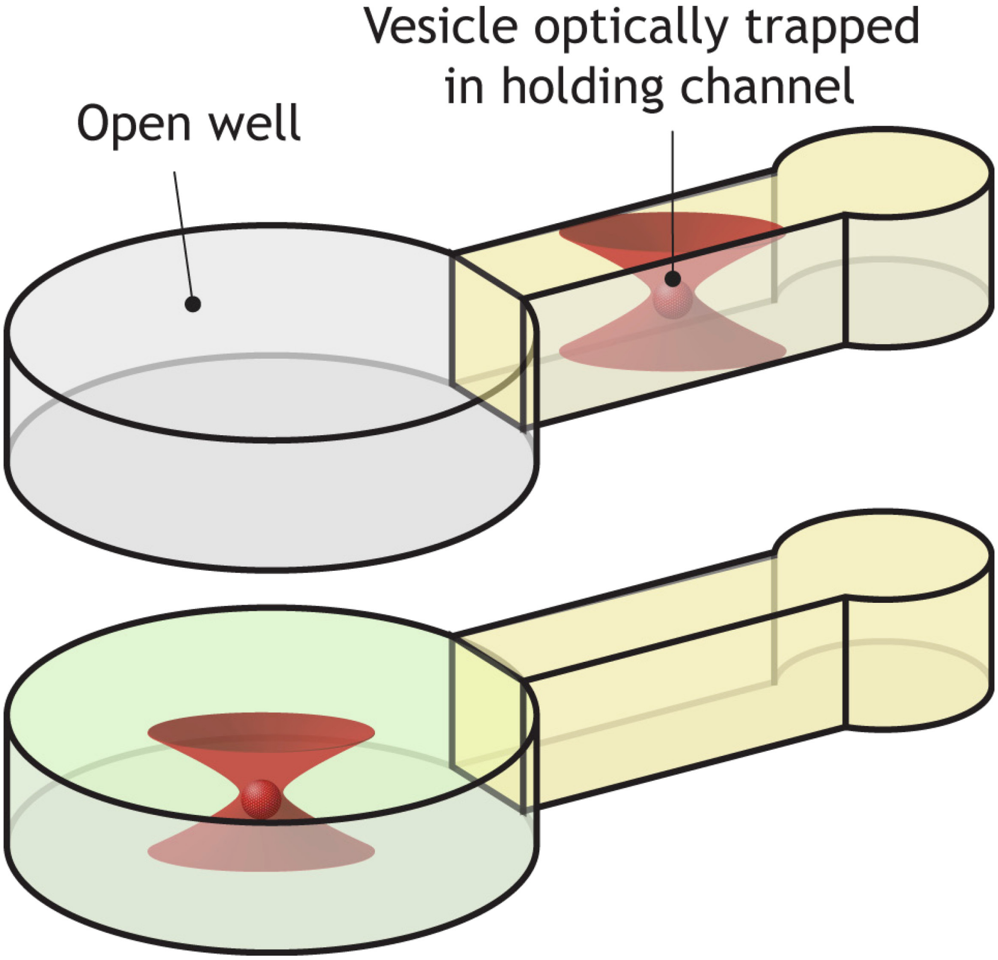

Figure 2.6: Confocal Raman microscopy vesicle manipulation. While a vesicle is optically trapped in the holding channel (not to scale), the solution in the well is replaced. By optical trapping, the vesicle is moved into the well a measurement is performed, after which the vesicle is returned to the holding channel so that the process can be repeated.

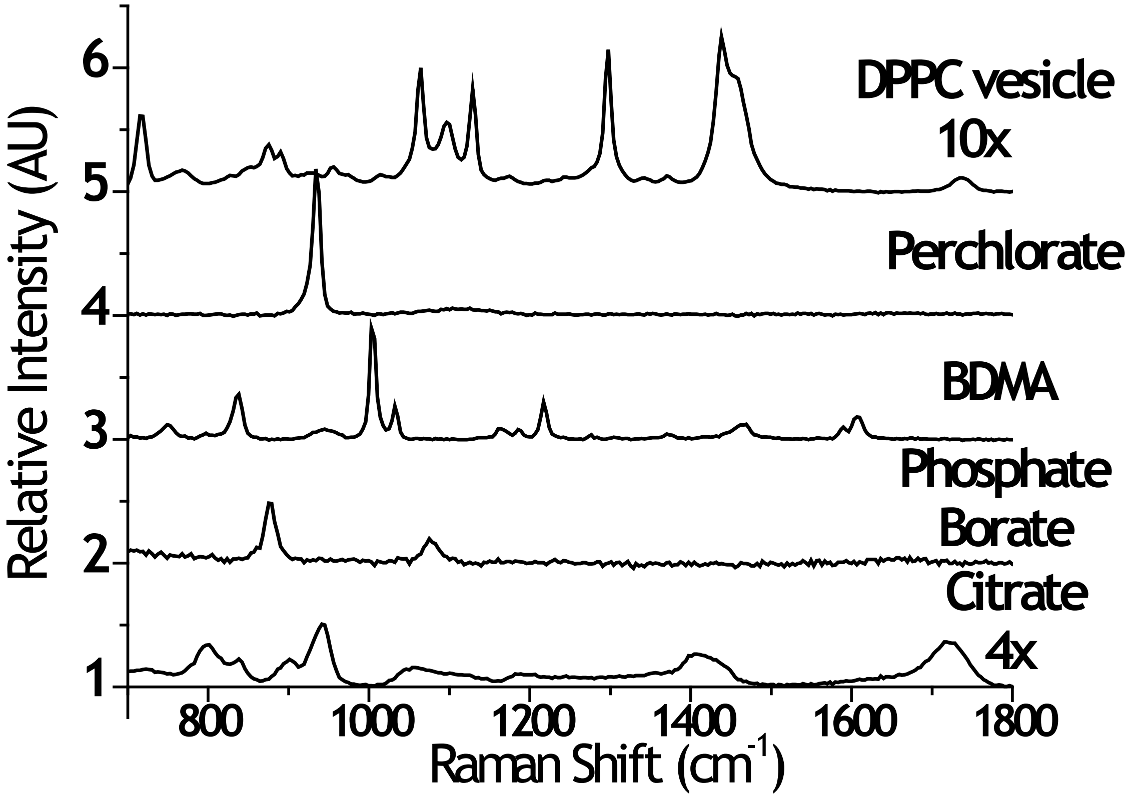

Figure 2.7: Standard Raman spectra used in the least squares analysis. From the top, first is an optically-trapped DPPC vesicle, scaled by a factor 10. Next is 160 mM sodium perchlorate, followed by 250 mM BDMA acidified with HCl (pH <2), 50mM/50mM/419mM phosphate/borate/sodium chloride buffer at pH 5.0, and finally 500 mM citrate buffer at pH 2.9, which has been scaled by a factor 4. All spectra (except that of the DPPC vesicle) are normalized by their concentrations and integration times in order to show the relative scattering intensities of the component species.

To determine the concentration of the components in a sample from the corresponding measured spectra, a least squares fit of the sample spectrum to the standard spectra was performed, minimizing the squared residuals across the entire spectrum from between 700 and 1800 cm^{-1} as in Figure 2.8. The concentration of a given component is directly proportional to the magnitude of the corresponding scaling factor obtained from the least squares fit. However the concentration reported by the scaling factor is not necessarily the concentration inside the vesicle, but rather the average concentration in the confocal volume. Because there is limited control over vesicle size, the fraction of the confocal volume that is filled by a vesicle will vary. Thus, to estimate the concentration of BDMA accumulated inside of a vesicle, sodium perchlorate was included as an internal standard in the vesicle buffer. The perchlorate ion, which exhibits strong Raman scattering at ~940 cm^{-1} from the ClO_4^- symmetric stretch,[25] has been shown to be DPPC membrane impermeant.[15] Thus, assuming that the perchlorate ion occupies the same volume as accumulated BDMA in the vesicle, the concentration of BDMA within the vesicle can be estimated by ratioing the fitted scaling factor for BDMA to the fitted scaling factor of perchlorate and multiplying by the known concentration of perchlorate in the vesicle buffer.

The error in reporting the concentration of BDMA inside of a vesicle was estimated by performing 5 replicate 300-s integration measurements on a vesicle containing citrate buffer, sodium perchlorate, and BDMA in a solution of phosphate/borate buffer at equilibrium, where the vesicle was optically manipulated to different regions of the well to simulate the movement of a vesicle in and out of the holding channel. Each replicate was fit using least squares with the standard spectra, and

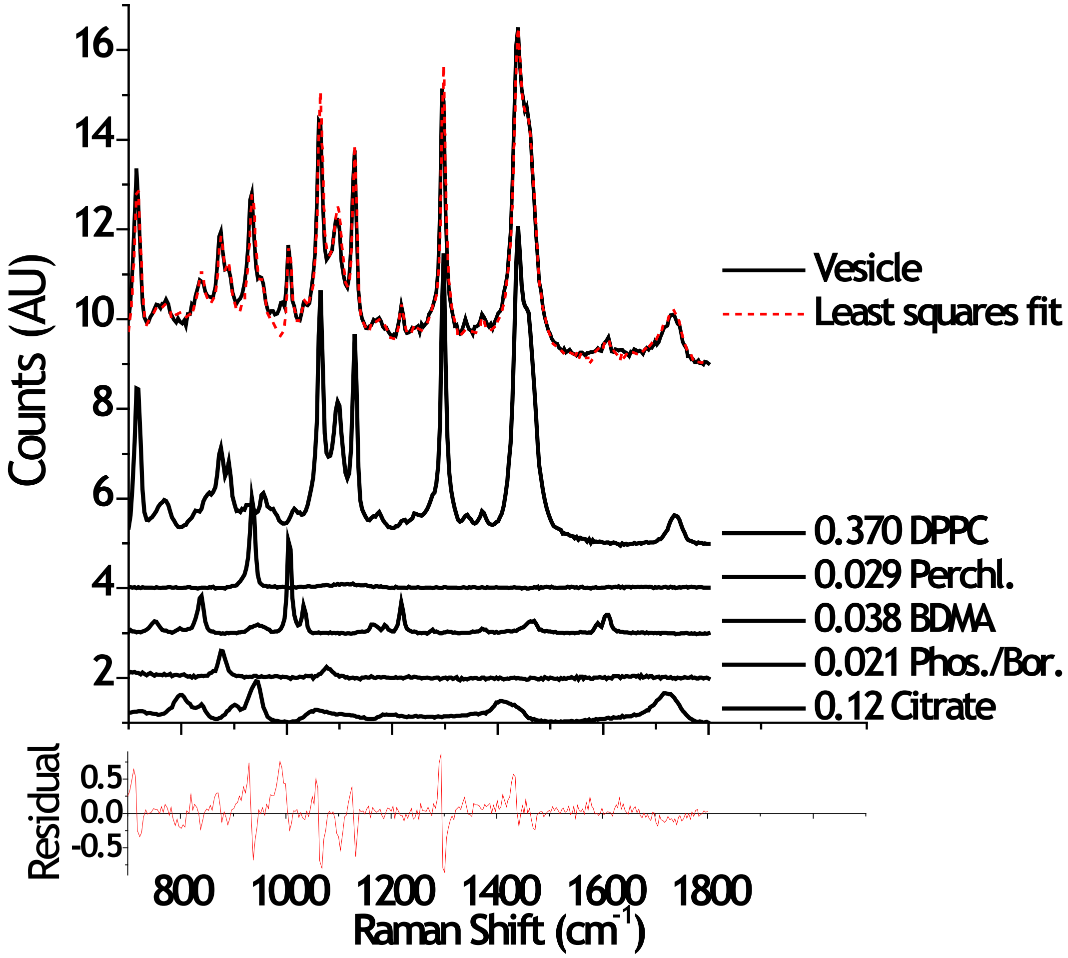

Figure 2.8: Least squares analysis of a Raman spectrum from vesicle containing 0.5 M citrate buffer and 80-mM perchlorate, initially at pH 2.9 then equilibrated in phosphate/borate/sodium chloride and 15-uM BDMA at pH 7.7. From the top, the solid black curve is the vesicle spectrum, and the dotted red curve is the least squares fit to the standard spectra plotted below: these include DPPC (37% of the intensity of the standard vesicle), perchlorate (29 mM), BDMA (38 mM), phosphate/borate (21 mM), and citrate (120 mM). At the very bottom are the residuals of the least squares fit.

the least squares fit parameters for the average concentration of BDMA and perchlorate in the confocal volume were 30 ± 4 mM and 18 ± 3 mM, respectively. From the ratio of these concentrations multiplied by the concentration of perchlorate ion in the vesicle (80 mM), the concentration of BDMA within the vesicle is calculated to 130 ± 30 mM, where the standard deviation of the BDMA concentration, 30 mM, was estimated by propagation of errors assuming negligible covariance. To estimate the BDMA concentration uncertainties for spectra acquired with longer or shorter integration times, the results are scaled by the inverse square-root of the integration times. Fitting of data spectra to linear combinations of the pure standards spectra resulted in residuals across the spectrum having magnitudes less than 10%, as shown in Figure 2.8. The relative standard deviation of fitted parameters for replicates was generally less than 20%.

2.4.2 Measurements of analyte accumulation in vesicles

To test the accumulation of BDMA into a vesicle over time, ~600-nm diameter phospholipid vesicles containing 0.5-M citric acid buffer with 80 mM sodium perchlorate set at pH 2.9 were diluted into 50/50/419-mM phosphate/borate/sodium chloride buffer at pH ~4.5 and injected into the holding channel of the cell. A single vesicle was selected, optically trapped and pulled from the holding channel into the well having the same phosphate buffer set to a pH of 9.4 and containing 50-μM BDMA. The accumulation of BDMA inside the vesicle was monitored by collecting successive 30-s integrations until equilibrium had been achieved. Figure 2.9 is a plot of the time evolution of the spectra collected from a vesicle equilibrating in the well. In the spectral region plotted in Figure 2.9A, the principle peaks from perchlorate, BDMA, and DPPC can be observed, where

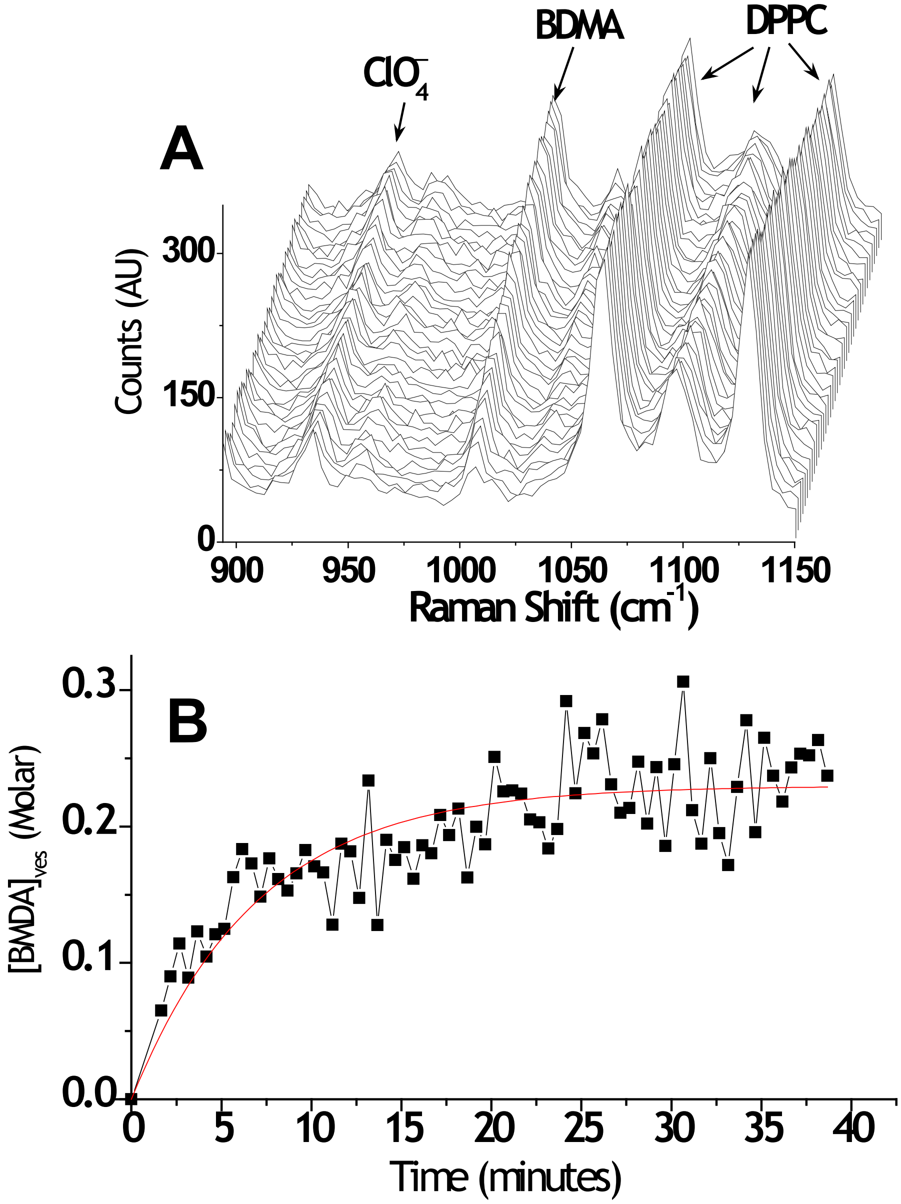

Figure 2.9: Time evolution of the spectra (A) from a 0.6-μm diameter vesicle containing 80-mM perchlorate and 0.5-M citric acid buffer initially at pH 2.9, transferred into phosphate/ borate buffer at pH 9.4 with 50-μM BDMA. The perchlorate ion symmetric stretch at ~940 cm^{-1}, the ring trigonal mode of BDMA at 1006 cm^{-1}, and C-C vibrations associated with the acyl chains of DPPC between ~1050 cm^{-1} and ~1130 cm^{-1} are noted. (B) The concentration of BDMA in the vesicle over time determined from a least squares fit of Raman spectra to the standard spectra in Figure 2.7, fit to an exponential rise to a maximum with a time-constant of 7 min.

the symmetric stretch[25] of the ClO_4^- ion can be identified at ~940 cm^{-1}, the trigonal ring deformation[26] of BDMA is at ~1005 cm^{-1}, and the three C-C trans/gauche vibrations[27] of DPPC are found between 1050 and 1130 cm^{-1}. Interestingly, the trans peak near 1130 decreases over time, while the gauche peak near 1100 broadens, which is an indication of increasing membrane disorder[28] as BDMA accumulates in the vesicle. As shown in Figure 2.9B, the BDMA achieves equilibrium accumulation in the vesicle with a ~7-min time-constant. The kinetics of transferring analyte into the vesicle are slower than a solution-diffusion controlled limit; the source phase solution volume required to supply the ~ 5×10^3 enriched concentration of BDMA is contained in a source-phase solution volume corresponding to a 5-μm radius sphere, diffusion through which would take only $t = r^2/6D$ ~ 30 ms to equilibrate with the vesicle membrane surface. Therefore, the rate of equilibration is not source-phase diffusion controlled, but likely limited by slow transport through the gel-phase lipid bilayer or by a slow rate of partition into the membrane. Nevertheless, the rate of reaching equilibrium is quite fast compared to a 5×10^3-fold extraction into any macroscopic volume. For example, a 1-mL receiver phase would need to be equilibrated with *5* liters of source phase, where molecular transport across the large dimensions of the source-phase solution would be extremely slow, even with convection or stirring.

To test the source-phase pH dependence of analyte accumulation, the equilibrium concentration of BDMA inside of vesicles was measured as a function of the pH of the external solution. Extruded phospholipid vesicles containing 0.5-M citric acid buffer set at pH 2.9 with 80-mM sodium perchlorate were diluted into 50/50/419-mM phosphate/borate/sodium chloride buffer set at pH ~4.5 and injected into the holding channel of the cell. A single vesicle was again selected, optically trapped and pulled into the well containing phosphate buffer with 15-μM BDMA and a pH that was varied from 6.0 to 9.5. In each solution condition, the Raman spectrum of the vesicle was periodically checked to determine when equilibrium had been achieved, after which a measurement was made by integrating for at least 600 s. After a spectrum was measured, the vesicle was returned to the holding channel, the well was emptied and replaced with the next higher pH solution, and the measurement was repeated.

The Raman spectra from this experiment, normalized for differences in integration time, are plotted in Figure 2.10. Each of these spectra was fit by linear least squares to the standard spectra in Figure 2.7 to determine the concentration of BDMA in the vesicle by taking the ratio of the least squares fitted BDMA and perchlorate amplitudes, as described above. The resulting concentrations are plotted as a function of the pH of the source phase in Figure 2.11, along with the theoretical predictions of the vesicle concentration of BDMA, where $[\mathrm{BDMA}]_{\mathrm{tot}} = 15\ \mu\mathrm{M}$, $\mathrm{pK_a}$ of BDMA = 8.9, total citrate concentration in the vesicle is 0.5M, the internal pH is initially 2.9, and the source phase pH is as indicated. The data show that the enrichment achieved at the highest pH gradient was $2.3\mathrm{x}10^4$ or about 80% of the predicted enrichment factor. The measurement of the concentration of BDMA in the vesicle by Raman spectroscopy is consistently lower than the prediction across the entire range of source-phase pH values.

To reconcile the prediction with the measurement, some of the input parameters in the model were varied individually, and the resulting prediction curve was compared to the data. For example, when the total concentration of buffer in the vesicle was decreased, the result was a theoretical curve having a shape that does not correspond to

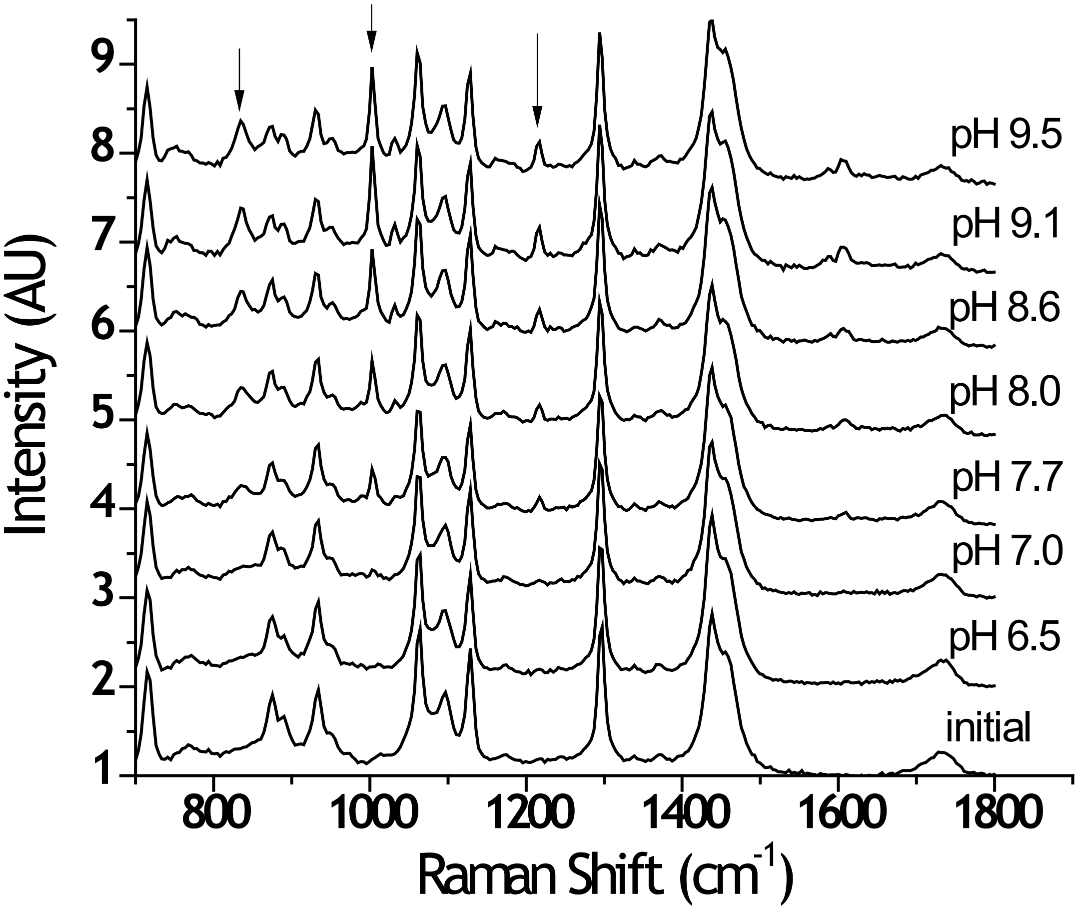

Figure 2.10: Normalized spectra collected from a single vesicle containing 80-mM perchlorate and 0.5-M citrate initially at a pH of 2.9 before and after equilibration in phosphate/borate buffers with 15-µM BDMA at different values of source-phase pH, as noted. The growth of BDMA intensity is noted with arrows.

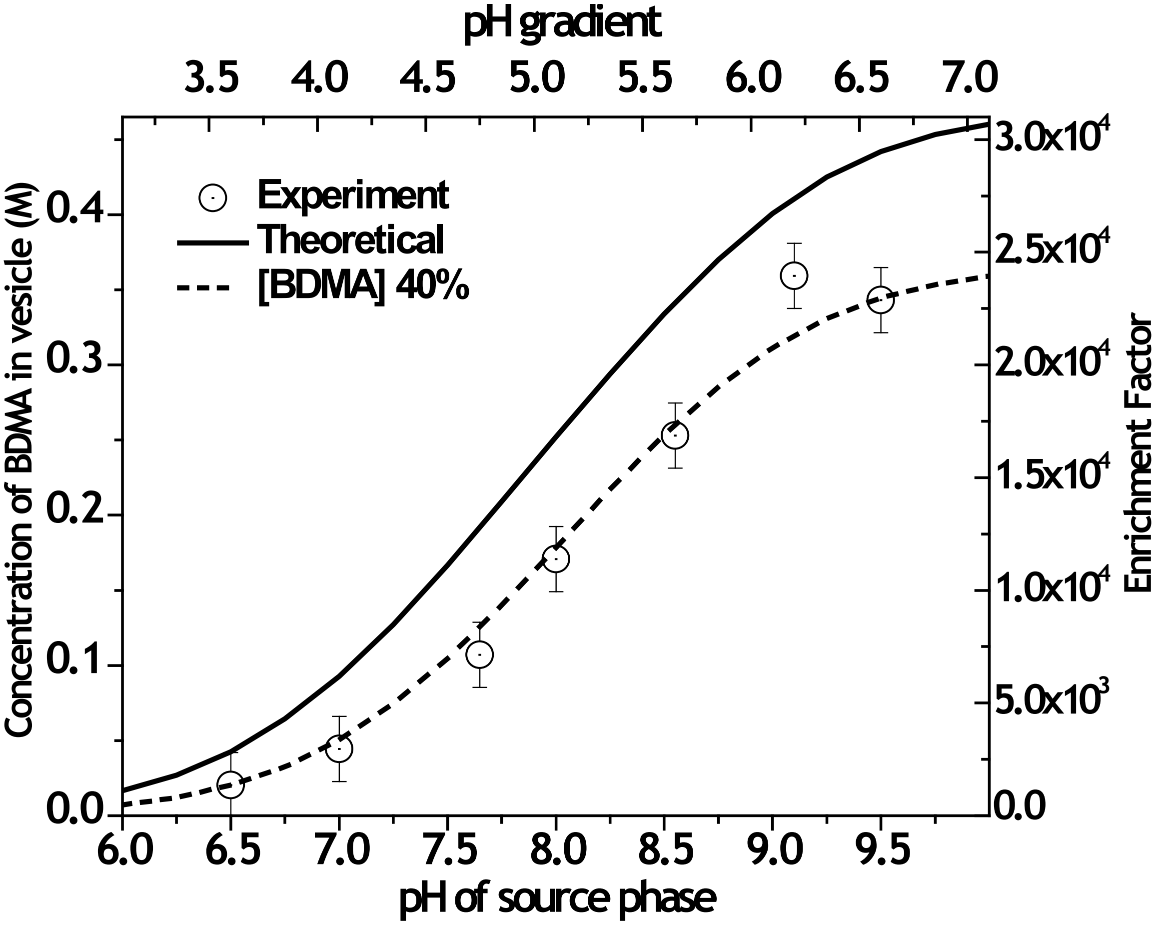

Figure 2.11: Theoretical (lines) and measured (points) concentrations of BDMA inside of a vesicle containing 0.5-M citrate buffer initially at pH 2.9, equilibrated in source phase phosphate/borate/sodium chloride buffers with 15-µM BDMA at the pH indicated. The solid curve represents the predicted concentration of BDMA from the solution to the 6th-order polynomial model in Figure 2.3. The dashed curve represents the theoretical accumulation as if the concentration of BDMA were lowered by 40% due to an activity coefficient of 2.5.

the experimental points over full the range of pH. However, it was found that simply scaling the source concentration of BDMA by a factor of 40% brings the predicted concentrations in line with the experimental results, as observed in the dashed line of Figure 2.11. This suggests the impact of activity in non-ideal solution conditions within the vesicle, where the concentration of solutes exceeds 1M. Based on the results, the activity coefficient for BDMA in the vesicle is estimated to be ~2.5. This could be explained by a salting-out effect, as utilized in separation of proteins,[29] on the relatively hydrophobic benzyl amine, where the total concentration of salts inside the vesicle approaches 1 M at the highest BDMA enrichment conditions.

2.5 Conclusion

With the development of a model to account for depletion of the source phase and buffering of the vesicles, an experiment was designed where the predicted enrichment factors on the order of 10^4 for a model analyte compound, BDMA, inside of phospholipid vesicles could be achieved. Optical-trapping confocal Raman microscopy using a cell with a holding channel and open well allows the response of a single vesicle to various source-phase solution conditions to be characterized. The concentration of BDMA inside of the vesicle was determined using linear least squares with ratioing to an internal perchlorate ion standard. The standard spectra were also used to quantify the relative concentrations of other components in the observation volume, including the phospholipid and the intra- and extra-vesicle buffers. The accumulation of BDMA was found to be fast, but not diffusion limited; these kinetics and their dependence on vesicle membrane composition will be characterized in future research. In the present work, the concentration of BDMA inside of the vesicle at the highest pH gradient was 350 ± 20 mM, which compared to a source phase concentration of 15 μM corresponds to an enrichment factor of 2.3 x 10^4. Although this result is 20% less than predicted by theory, the results suggest that vesicle pH gradients can be utilized for rapid preconcentration of acid-base active analyte compounds in aqueous solution for quantitative analysis. Confocal Raman microscopy or other spectroscopic microscopies are suitable for measuring the analyte concentrations that accumulate within a single vesicle.

2.6 References

(1) Barani, H.; Montazer, M. *Journal of Liposome Research* **2008**, *18*, 249.

(2) Reza Mozafari, M.; Johnson, C.; Hatziantoniou, S.; Demetzos, C. *Journal of Liposome Research* **2008**, *18*, 309.

(3) Fenske, D. B.; Cullis, P. R. *Methods in Enzymology* **2005**, *391*, 7.

(4) Drulis-Kawa, Z.; Dorotkiewicz-Jach, A. *International Journal of Pharmacology* **2010**, *387*, 187.

(5) Mayer, L. D.; Bally, M. B.; Cullis, P. R. *Biochimica et Biophysica Acta, Biomembranes* **1986**, *857*, 123.

(6) Petre, C. E.; Dittmer, D. P. *International Journal of Nanomedicine* **2007**, *2*, 277.

(7) Ceh, B.; Lasic, D. D. *Journal of Colloid and Interface Science* **1997**, *185*, 9.

(8) Cullis, P. R.; Hope, M. J.; Bally, M. B.; Madden, T. D.; Mayer, L. D.; Fenske, D. B. *Biochimica et Biophysica Acta* **1997**, *1331*, 187.

(9) Mayer, L. D.; Bally, M. B.; Hope, M. J.; Cullis, P. R. *Journal of Biological Chemistry* **1985**, *260*, 802.

(10) Bally, M. B.; Mayer, L. D.; Loughrey, H.; Redelmeier, T.; Madden, T. D.; Wong, K.; Harrigan, P. R.; Hope, M. J.; Cullis, P. R. *Chemical Physics of Lipids* **1988**, *47*, 97.

(11) Thurn, R.; Kiefer, W. *Applied Spectroscopy* **1984**, *38*, 78.

(12) Urlaub, E.; Lankers, M.; Hartmann, I.; Popp, J.; Trunk, M.; Kiefer, W. *Chemical Physics Letters* **1994**, *231*, 511.

(13) Ajito, K. *Applied Spectroscopy* **1998**, *52*, 339.

(14) Houlne, M. P.; Sjostrom, C. M.; Uibel, R. H.; Kleimeyer, J. A.; Harris, J. M. *Analytical Chemistry* **2002**, *74*, 4311.

(15) Cherney, D. P.; Conboy, J. C.; Harris, J. M. *Analytical Chemistry* **2003**, *75*, 6621.

(16) Ajito, K.; Han, C.; Torimitsu, K. *Analytical Chemistry* **2004**, *76*, 2506.

(17) Cherney, D. P.; Myers, G. A.; Horton, R. A.; Harris, J. M. *Analytical Chemistry* **2006**, *78*, 6928.

(18) Fox, C. B.; Horton, R. A.; Harris, J. M. *Analytical Chemistry* **2006**, *78*, 4918.

(19) Fox, C. B.; Myers, G. A.; Harris, J. M. *Applied Spectroscopy* **2007**, *61*, 465.

(20) Cherney, D. P.; Harris, J. M. *Annual Review of Analytical Chemistry* **2010**, *3*, 277.

(21) Ajito, K.; Morita, M.; Torimitsu, K. *Analytical Chemistry* **2000**, *72*, 4721.

(22) Heider, E. C.; Barhoum, M.; Edwards, K.; Gericke, K.-H.; Harris, J. M. *Analytical Chemistry* **2011**, *83*, 4909.

(23) McCreery, R. L. In *Chemical Analysis*; John Wiley & Sons: New York, 2000, p 264.

(24) Kuyper, C. L.; Brewood, G. P.; Chiu, D. T. *Nano Letters* **2003**, *3*, 1387.

(25) Hester, R. E.; Plane, R. A. *Inorganic Chemistry* **1964**, *3*, 769.

(26) Foil, A. M. *Journal of Raman Spectroscopy* **1988**, *19*, 219.

(27) Litman, B. J.; Lewis, E. N.; Levin, I. W. *Biochemistry* **1991**, *30*, 313.

(28) Fox, C. B.; Uibel, R. H.; Harris, J. M. *The Journal of Physical Chemistry B* **2007**, *111*, 11428.

(29) Englard, S.; Seifter, S. *Methods in Enzymology* **1990**, *182*, 285.

CHAPTER 3

MICROSCOPIC RATES OF PEPTIDE-PHOSPHOLIPID BILAYER INTERACTIONS FROM SINGLE-MOLECULE RESIDENCE TIMES

Grant A. Myers, Daniel Gacek, Eric M. Peterson, Christopher B. Fox, and Joel M. Harris
This manuscript was submitted for publication to *Journal of the American Chemical Society*, June 2012.

3.1 Introduction

The membrane catalysis hypothesis[1-3] suggests that signaling peptides targeting membrane-resident receptors must first interact with the membrane bilayer before binding with their receptor. According to this model, membrane interactions can facilitate ligand-receptor binding in several ways. First, interactions of the peptide with the membrane effectively concentrate the ligand near the receptor. Second, the reduced dimensionality of diffusion across the membrane to the receptor can be more efficient than three-dimensional diffusion through solution. Finally, conformational changes associated with membrane binding can effectively pre-fold the peptide structure and position it within the membrane for receptor interaction binding. Thus, interactions between signaling peptides and cell membranes can play a critical role in membrane-resident receptor binding. In this work, we analyze single-molecule fluorescence imaging data to extract the microscopic rates of peptide-membrane association, applying this method to the study of glucagon-like peptide-1 (GLP-1) and its interactions with a supported lipid bilayer.

GLP-1 is an incretin, a 30-residue peptide hormone of the digestive system that has been linked to systemic insulin and glucagon levels.[4] Because of their effects on blood glucose levels, synthetic analogues of GLP-1 have been successfully developed as treatments for type 2 diabetes.[5] The target of this hormone is a G protein-coupled receptor, located in cell membranes throughout the body including pancreas, lung, gastrointestinal tract, and central nervous system.[6] Like many membrane-active peptides,[3,7] GLP-1 undergoes a significant conformational change upon binding to a phospholipid membrane. The peptide exists as a random coil in solution, and it must first associate with the membrane and reorganize into an alpha helix in the amphipathic environment of the cell membrane[8-11] before interacting with its receptor. Recently, X-ray crystallography has shown that GLP-1 adopts an alpha helix conformation when bound to its receptor. [12]

It is expected that the transition of GLP-1 from a random-coil peptide in solution to a folded state in a membrane should involve a significant release of enthalpy, to compensate for the entropy penalty of a folded peptide.[7] This step should represent a kinetic barrier, where the peptide may arrive, adsorb, and leave the membrane before transitioning to a more stable, folded state. Membrane binding studies of other amphipathic peptides[13,14] have reported evidence of two membrane-dissociation rates. In preliminary work from this lab,[15] evidence of two populations of GLP-1, weakly and strongly associated with a supported lipid bilayer, was found in the residence times of individual fluorescently labeled GLP-1 molecules, determined from images acquired by total-internal-reflection-fluorescence (TIRF) microscopy. The observed residence-time histograms were biexponential, suggesting two rates for peptides leaving the membrane.[15] In this previous work, the relationships between the measured rates and the kinetic steps of peptide adsorption, folding, unfolding, and desorption were not developed. In the present work, a kinetic model is derived to account for the observed single-molecule residence-times in terms of the microscopic rates of peptide adsorption and intercalation in the membrane. This model is applied to new measurements of the number density and residence times of fluorescently-labeled GLP-1 interacting with a 1,2-dipalmitoyl-sn-glycero-3-phosphocholine (DPPC) planar lipid bilayer supported on glass, where microscopic rate constants of peptide-membrane association are determined from a fit of the three-state kinetic model to the results.

3.2 Theory

3.2.1 Three-state model of membrane association

When the sequence of adsorption and insertion steps of a peptide interacting with a membrane is reversible, a model that describes the expected kinetics is a consecutive first-order three-state kinetic scheme, illustrated in Figure 3.1. In this model, F represents the free-solution population of peptide, W represents weakly-associated, likely random-coil peptides adsorbed to the membrane surface, and S represents a strongly-associated and folded population within the membrane. The constants, k_1 through k_4, represent the rate constants for the transitions between these three populations. The heterogeneous rate

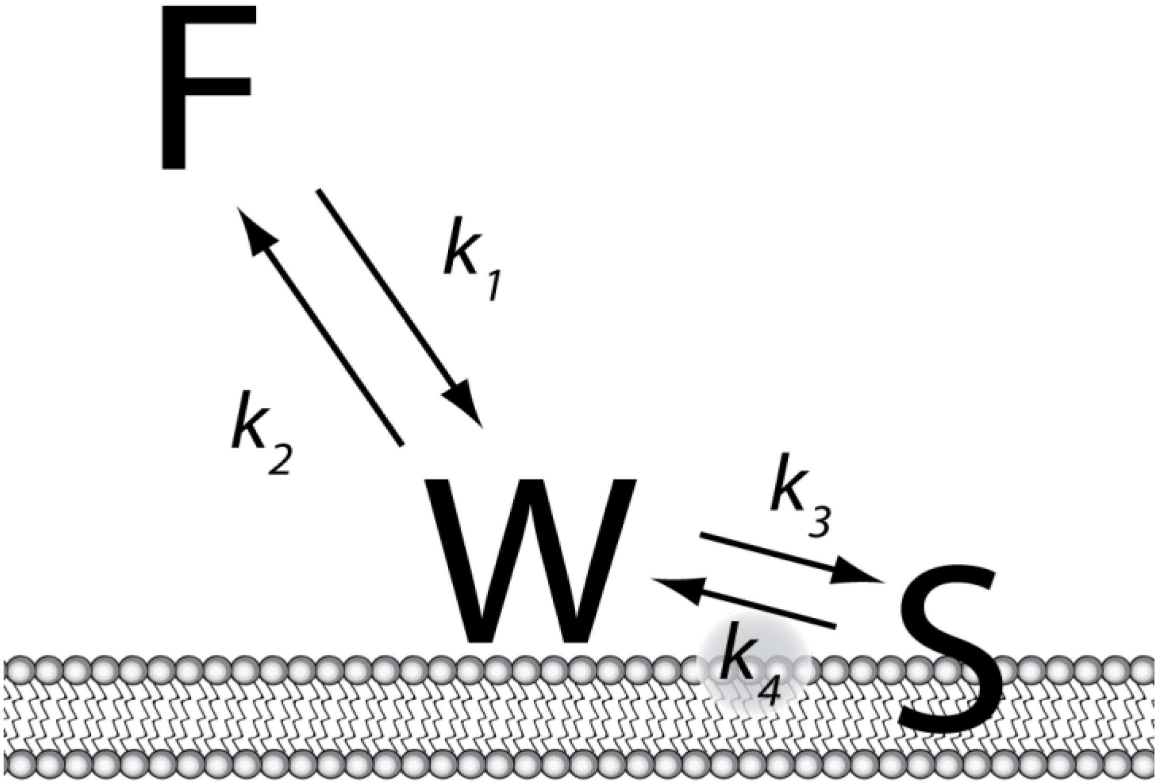

Figure 3.1 Three-state kinetic model for the interaction of a membrane-active peptide with a phospholipid bilayer, where a free peptide in solution, F, adsorbs to the bilayer in a weakly bound state, W, followed by folding and insertion into the bilayer in a strongly-associated state, S.

constant k_1 describes the rate of molecules adsorbing to the membrane from solution. The rate constant k_2 characterizes the rate of desorption of weakly associated peptide from the membrane surface. The rate constant k_3 is the intercalation rate, where molecules transition from the weakly-associated, adsorbed state to the longer-lived folded and membrane-inserted state. The rate constant k_4 describes a process where molecules reemerge from the folded state to the weakly-bound surface-adsorbed state, at which point the molecules may either leave the surface (at a rate k_2), or return to the strongly-associated state (at a rate k_3).

When residence times of individual labeled GLP-1 peptides are measured using TIRF microscopy, the cumulative residence-time histogram data are well described by a biexponential decay[15] (see results below):

$$H(t) = P_1 e^{-t/\tau_1} + P_2 e^{-t/\tau_2} \tag{2.1}$$

where the observed time constants are inversely related to the decay rates of the two apparent populations, $r_1 = 1/\tau_1$ and $r_2 = 1/\tau_2$, and the preexponential coefficients P_1 and P_2 represent the relative numbers of events from these two populations. It is tempting to conclude that the longer residence time corresponds to the lifetime of the folded peptide, S, in the membrane and the shorter residence time represents desorption of W from the membrane surface. This interpretation ignores the fact that the kinetic steps are strongly coupled. For example, the emergence of a folded peptide to the membrane surface does not immediately lead to its desorption into solution; both desorption (k_2) and reinsertion (k_3) extend the lifetime of the peptide on or within the membrane upon its reemergence to the membrane surface. The goal of this section, therefore, is to derive the relationship between the measured single-molecule residence times and preexponential factors in Equation 3.1 and the microscopic rate constants described by the kinetic model in Figure 3.1; this relationship can then be used to interpret membrane association kinetics of GLP-1 or other membrane-active peptides.

3.2.2 Interpreting single-molecule residence-time histograms

The relationships between the measured parameters from residence-time histograms and the intrinsic microscopic rate constants is determined by an analysis of the system of differential equations associated with the three-state reversible first order system illustrated in Figure 3.1.

$$
\begin{aligned}
\partial F / \partial t &= -k_1 F(t)\lambda^{-1} + k_2 W(t)\lambda^{-1} \\
\partial W / \partial t &= k_1 F(t) - (k_2 + k_3) W(t) + k_4 S(t) \\
\partial S / \partial t &= k_3 W(t) - k_4 S(t)
\end{aligned}
\qquad [3.2]
$$

where F, W, and S are the concentrations of the respective populations and λ^{-1} is the ratio of the surface area of the bilayer to the volume of the solution that accounts for the change in dimensionality. This system of equations is one of a few multistep kinetic schemes having an analytical solution. While the general solutions are cumbersome (see Supporting information in Appendix), particular solutions to the system have been published as early as the turn of the last century.[16-18] For the present application, symbolic computational methods were used to solve the general system of differential equations explicitly and then to apply boundary conditions to the results to obtain the analytical relationships between the individual rate constants of adsorption, intercalation, emergence, and desorption from the parameters determined from single-molecule residence histogram measurements.

The information contained in a histogram of residence times is derived from the random arrival of molecules at the membrane surface; these molecules associate with the membrane for a period of time and then leave. To construct a histogram of residence times, all of the events measured during an experiment are aligned onto a new time axis, so that each event begins at time zero (see Figure 3.2). This realignment of the data establishes the first of two boundary conditions for solving the differential equations. First, because all of the molecules arrive at time $t = 0$ on the membrane surface, then within the assumptions of the three-state model, they all begin in the weakly bound or adsorbed state, so that the initial condition for the normalized population is $W(t{=}0) = 1$ and $S(t{=}0) = 0$. Some of the adsorbed molecules may then leave the surface without transitioning to the strongly-bound state, while other molecules may successfully transition between the weakly- and strongly-bound states, and thus persist for a longer time before leaving the surface (see Figure 3.2). A second constraint arises from the very low surface density of peptides observed in these experiments, where the probability of an interrogated spot being doubly occupied is very small, less than 1.2% (see below). As a result, kinetics reported in the residence-time histograms have no significant contribution from an additional molecule binding to the membrane surface within an interrogated spot, prior to the original molecule leaving; therefore, the adsorption rate is neglected in the kinetic analysis, $k_1 = 0$.

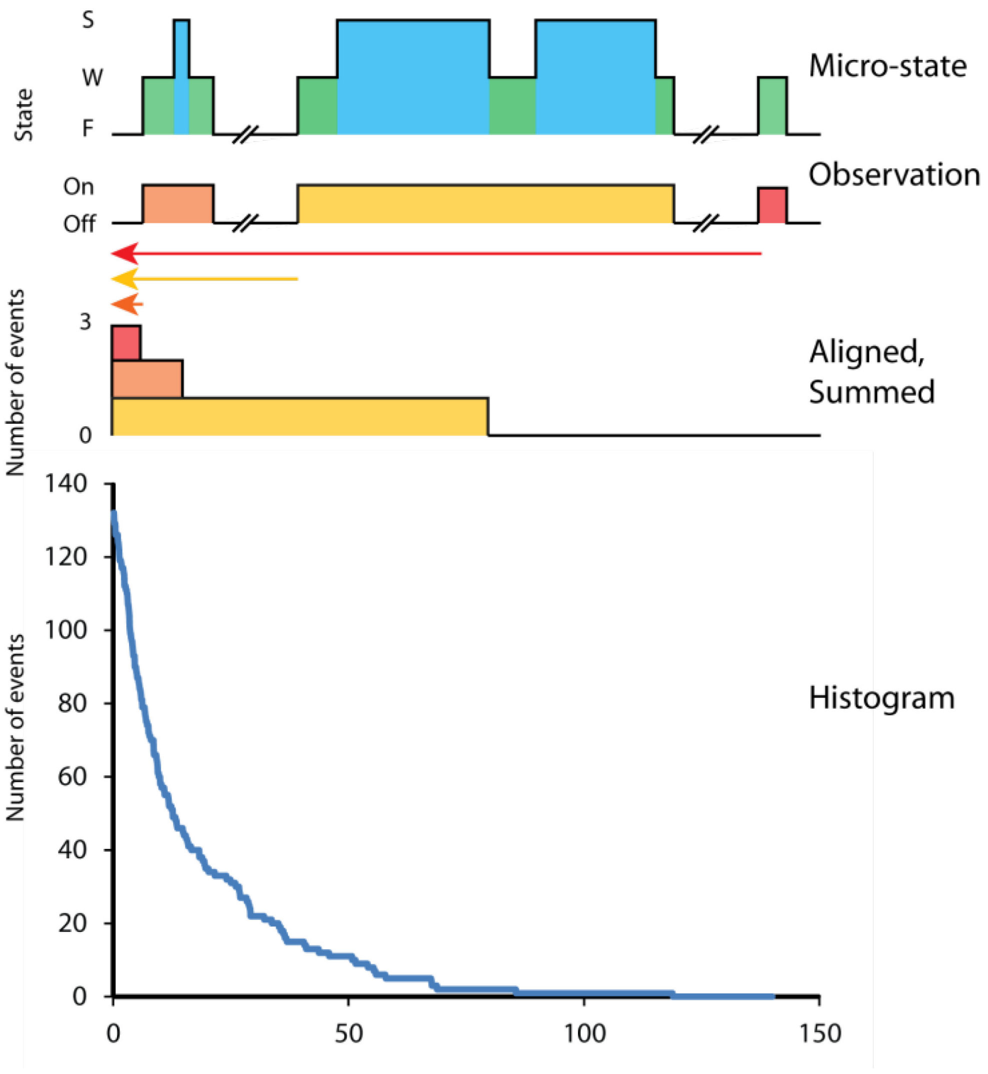

Figure 3.2 Construction of a single-molecule residence-time histogram. Top trace shows the binding state of three molecules arriving and leaving the lipid bilayer; peptides arrive at the bilayer surface in the weakly bound state and may transition into the folded, strongly bound state. The observation of a molecule in a fluorescence image cannot distinguish between micro-states of the bound peptide. To construct a histogram, all observed events are aligned onto a new time axis having an origin that coincides with the arrival of each molecule; these events are then summed on this new axis to produce a residence-time histogram.

When these two constraints are applied to the system of differential equations (see Supporting information in Appendix), the time dependences of the two surface populations, $W(t)$ and $S(t)$, are *both* biexponential functions, having different preexponential factors but sharing the same pair of rates:

$$r_1 = \frac{1}{2}\left(k_2 + k_3 + k_4 + \sqrt{(k_2 + k_3 + k_4)^2 - 4k_2k_4}\right) \tag{3.3a}$$

$$r_2 = \frac{1}{2}\left(k_2 + k_3 + k_4 - \sqrt{(k_2 + k_3 + k_4)^2 - 4k_2k_4}\right) \tag{3.3b}$$

These functions are summed to obtain the time dependence of the entire surface population, $H(t) = W(t) + S(t)$. The result is biexponential decay without offset, corresponding exactly to the form of Equation 3.1, , where r_1 and r_2 are given by Equations 3.3a and 3.3b, while P_1 and P_2 are given by:

$$P_1 = \frac{k_2 - k_3 - k_4 + (r_1 - r_2)}{2(r_1 - r_2)} \tag{3.4a}$$

$$P_2 = \frac{-k_2 + k_3 + k_4 + (r_1 - r_2)}{2(r_1 - r_2)} \tag{3.4b}$$

While these expressions predict the observed rates and preexponential factors for single-molecule residence-time histograms from the intrinsic reaction rates, k_2, k_3, and k_4, they can be readily rearranged so that the intrinsic rates can be determined from measured residence-time histograms. The resulting relationships derived for determining the intrinsic rates from measureable quantities are remarkably simple. For example, the rate constant for molecules leaving the surface, k_2, is the population-weighted average of the two observed rates in the histogram decay:

$$k_2 = \frac{P_1 r_1 + P_2 r_2}{P_1 + P_2} \qquad [3.5]$$

The rate constant for molecules transitioning from the strongly associated state back to the weakly associated, adsorbed state is the ratio of the product of the histogram rates to the intrinsic rate constant for molecules leaving the surface:

$$k_4 = \frac{r_1 r_2}{k_2} \qquad [3.6]$$

Finally, the rate constant of molecules transitioning from the weakly associated to the strongly associated state is given by the difference between the sums of the histogram decay rates and the intrinsic reverse rate constants:

$$k_3 = (r_1 + r_2) - (k_2 + k_4) \qquad [3.7]$$

These expressions will be used in this work to interpret histograms of GLP-1 residence times in supported lipid bilayers, but they are useful generally for interpreting two-state binding kinetics from single-molecule imaging experiments.

3.2.3 Interpreting single-molecule binding isotherms

The general solution to the system of differential equations for the three-state model of membrane association can also be used to interpret the equilibrium population of molecules at the membrane surface. These data are generally collected as an isotherm, where the number densities of membrane-associated molecules are measured by counting fluorescent spots in a known area as a function of solution concentration.[15] Because the fluorescence image data cannot distinguish whether molecules are weakly or strongly bound, the measured isotherm reports the total equilibrium population density, $W_{eq} + S_{eq}$. The ratio of this total surface concentration and the free solution concentration, F_{eq}, is the slope of the isotherm and the equilibrium constant for binding, K_0. This ratio can be derived from the general solution to system of Equation 3.2, under the assumption that the initial (arbitrary) populations, $F(0)$, $W(0)$, and $S(0)$, have evolved over long times ($t \gg 1/r_2$) to their equilibrium values (see Supporting information in Appendix):

$$\frac{W_{eq} + S_{eq}}{F_{eq}} = K_0 = \frac{k_1 k_4 + k_1 k_3}{k_2 k_4} \qquad [3.8]$$

It is useful to note that K_0 is a ratio of a surface concentration (molecules/area) to a solution concentration (molecules/ volume), and thus has units of distance. This distance is meaningful and represents the depth into solution above the surface that contains the same number of molecules that are bound to a given surface area.[19,20]

This expression can be easily rearranged to solve for the rate constant k_1, which characterizes adsorption of peptides to the membrane from solution:

$$k_1 = K_0 \frac{k_2 k_4}{k_3 + k_4} \qquad [3.9]$$

Note that k_1 is a heterogeneous rate constant having units of velocity (cm s^{-1}) and characterizes the rate of collision and adsorption of molecules from solution to the membrane surface. It is analogous to the use of heterogeneous reaction rates in electrochemistry,[21] which describe the rates of collision and electron transfer with an electrode surface. Finally, Equation 3.9 shows that by combining information from the slope of the binding isotherm, K_0, with rate constants, k_2, k_3, and k_4, from the analysis of histograms of single-molecule residence times, one can determine all four rate constants in the three-state kinetic model.

Note that as the rate constant for peptide folding and membrane insertion, k_3, goes to zero, the kinetic model reverts to a simple two-state system, and Equation 3.8 simplifies to $K_0 = k_1 / k_2$, which describes a simple adsorption equilibrium. Setting k_3 equal to zero in Equation 3.3, shows that the histogram of single-molecule residence times becomes single exponential, where $r_1 = k_2$ and $r_2 =$ zero, so that the desorption rate of the simple two-state system is k_2. In the three-state system, the effective desorption rate, $[k_2 k_4 / (k_3 + k_4)]$ (see Equation 3.9), becomes proportionally slower. The factor slowing the off-rate relative to k_2 is $[k_4 / (k_3 + k_4)]$, and this factor represents the fraction of membrane-associated peptides that are weakly bound. When k_3 is large compared to k_4, most of membrane-bound peptides are folded and inserted, and the effective rate of molecules leaving the membrane is reduced by the small fraction of peptides in the W state that can leave the membrane surface.

3.3 Materials and Methods

3.3.1 Sample preparation

To characterize the interactions of GLP-1 with a phospholipid bilayer, fluorescently-modified glucagon-like peptide was synthesized using solid-phase peptide synthesis. A Cy3B fluorescent maleimide label (GE Amersham) was covalently attached to a cysteine bound via a 20-atom polyethylene-glycol linker (Novabiochem) to the C-terminus of the 30-residue peptide.[15] The sequence of labeled GLP-1 is HAEGTFTS-DVSSYLEGQAAKEFIAWLVKGR-PEG$_2$-cysteine-Cy3B (maleimide). The labeled peptide was purified by reverse-phase chromatography and its molecular weight verified by matrix-assisted laser desorption-ionization mass spectrometry (see Supporting information in Appendix). Dipalmitoyl-phosphatidylcholine (DPPC) phospholipid bilayers were deposited onto the microscope coverslips using a Langmuir-Blodgett/Langmuir-Schaeffer technique.[22,23] Glass coverslips were cleaned in a piranha solution, 60:40 concentrated H_2SO_4:30% H_2O_2, then rinsed and stored in ultrapure (Barnstead) water; caution: piranha is a corrosive solution that can cause skin or eye burns and can react explosively with organic compounds. After filling the Langmuir trough (KSV Instruments) with ultrapure water, a clean coverslip was immersed in the water subphase and 47 μL of 1 mg/mL DPPC in chloroform was deposited on the air-water interface. Following evaporation of the chloroform, the barriers were closed, compressing the lipid monolayer to a surface pressure of 35 mN/m or ~53 Å^2/molecule, and the coverslip was raised through the subphase surface at a rate of 4 or 5 mm/min to deposit a lipid monolayer. The coverslip was then positioned parallel to the trough surface, after which it was pushed down quickly through the lipid film (~40 mm/min) to form a bilayer. The transfer ratios for the upward and downward depositions were ~1 and ~1.2, respectively. The slightly larger transfer ratio for the second layer may be due to some lipid sticking to the backside of the coverslip dipping apparatus.[24] The flow cell with coverslip-supported lipid bilayer was assembled under water so that the bilayer was not exposed to an air-water interface. Fluorescence images of deposited DPPC lipid bilayers by Nile red staining show a uniform intensity distribution and no resolvable defects.

3.3.2 Instrument description and experiment protocols

Through-the-objective total-internal-reflection fluorescence (TIRF) microscopy[25] was used to selectively excite individual fluorescent peptide molecules at the glass/water interface. The microscope system consisted of a diode laser (B&W Tek) at 532 nm fiber-coupled into an Olympus IX71 microscope with 60x, TIRF objective having numerical aperture 1.45. Images of single molecules were collected at a framing rate of 10 Hz using an electron-multiplying charge coupled-device (CCD) camera (Andor iXon^{EM}+ 897).

To determine the equilibrium constant for binding, isotherm experiments were performed in which the number densities of peptides in the bilayer were measured with three or more replicates for each of several peptide concentrations ranging from 4 pM up to 100 pM with acquisitions of 100 or more frames. To measure single-molecule residence time histograms, 50 pM peptide solutions were equilibrated with a fresh bilayer in the microscope cell and images were acquired using a laser power of 3 mW in the collimated beam at the rear of the microscope with total acquisition times of 300 seconds (3000 frames), again with three replicates. To characterize the effects of laser power on measured histogram parameters for Cy3B-labeled peptide excited at 532nm, identical experiments were performed with two replicates each at laser powers ranging from 1.8 to 11.1 mW in the collimated beam at the rear of the microscope. Experiments were carried out at room temperature, ~ 22°C.

3.3.3 Image analysis

The number densities of peptide molecules bound to the lipid bilayer and their residence times were extracted from fluorescence images using an adjacent-pixel criterion[26] to identify the locations of molecules in each frame. The signature of a fluorescent spot from a molecule is distinguished from the random (single-pixel) fluctuations in the background by requiring that the intensity occupy an area on the camera face comparable to the diffraction-limited point spread function, which has a $1/e^2$ diameter of 2.4 pixels or 0.64 μm in the sample plane. This criterion is enforced by requiring that both the intensity of a central bright pixel and at least one of the eight pixels adjacent to the bright pixel exceeds a threshold of 3.0-times the standard deviation of the background. While the probability of a single pixel from the background exceeding this threshold is significant, 4.9×10^{-4} or 32 pixels per 256-by-256 pixel frame, the probability that one of the 8 pixels adjacent to any of these 32 pixels will also exceed the threshold is quite small, $8*32*4.9 \times 10^{-4}$ or 0.125 false spots per frame or one event in every eight frames.

To determine residence times of each peptide in the lipid bilayer, the locations of all molecules in each frame of the acquisition were recorded and then analyzed using an algorithm which can extend the measured residence times over photoblinking events[27-31] of the single dye label. For every identified molecule in a frame, 10 subsequent frames were searched for molecules centered at the same pixel position or in one of the surrounding eight pixels. If subsequent frames indicate a molecule in the region in question, the residence time for that molecular event was incremented by the appropriate amount. Then, starting with the last frame in which the molecule was identified, the 10-forward-frame-search was repeated until the entire residence time of the molecule was determined. Using this method, photoblinking events or random fluctuations that caused the intensity to fall below the threshold for as many as 10 frames (1 second) were 'bridged'. The duration of the bridging search was optimized by examining the stability of the fitted kinetic parameters relative to the length of the bridge; a one-second bridge was found to produce consistent kinetic results for the longer-lived population of bound peptides (see Supporting information in Appendix). Molecules exhibiting residence times of only a single frame were dropped from the analysis to avoid counting events arising from peptides in solution briefly visiting the 150-nm evanescent-wave region at the bilayer surface. For accumulation of data into a residence-time histogram, molecular events that started in the first or last 10 frames of the acquisition were also neglected because of their unknown total residence times.

When bridging brief off-states of the dye label in order to report more accurate residence times, there is a chance that a new molecule from solution will bind to the membrane in the area previously identified as occupied and lead to an increase in the reported residence time. To calculate the probability of this occurring, we take the product of the heterogeneous binding rate constant, $k_1 \sim 1 \times 10^{-4}$ cm s^{-1} (see below), the area of a 9-pixel site projected back through the collection optics onto the sample surface

(0.64 μm^2), and the solution concentration of peptide (50 pM = 3 x 10^{10} molecules/cm^3). The product of these factors is the binding rate from solution to the site area, 2 x 10^{-2} molecules $site^{-1}$ s^{-1} or ~50 seconds between such events. The time between binding events is thus 500 frames, or 50 times greater than the 10-frame bridge for a new molecule to arrive at a resolvable site when the peptide concentration is 50 pM. Thus, when using this algorithm, there is 2% probability that a recorded residence time will be extended by the arrival and binding of a new peptide from solution (see Supporting information in Appendix).

3.4 Results

3.4.1 Binding of GLP-1 to DPPC lipid bilayers

To observe the population and residence times for GLP-1 on a lipid membrane, a DPPC bilayer was deposited onto a glass coverslip and exposed to varying concentrations of Cy3B-labeled GLP-1 in buffered solutions. Fluorescence images of the labeled peptide on the lipid bilayer were acquired, and from those images, molecular spots were identified and counted. The average intensity of labeled peptide fluorescence spots was 87 photoelectrons (PEs) for the brightest pixel and 66 PEs for the next brightest pixel, both of which are much greater than the 37-PE detection threshold (3.0-standard deviations above background) used to identify molecular spots. Intensity distributions of Cy3B-labeled GLP-1 fluorescence spots are plotted in Supporting information in Appendix and used to determine the probability of missing molecules in an image (false negatives). This probability was evaluated by fitting the distribution of measured intensities and determining what fraction of second-brightest pixels fall below the detection threshold; from these results (see Supporting information in Appendix), the false-negative probability or fraction of GLP-1 molecules that are missed in a given image is small, less than 7%. An example fluorescence image with identified molecular spots is shown in Figure 3.3.

To determine the equilibrium constant for GLP-1 binding to a DPPC bilayer, the number densities of molecules in the bilayer were measured by imaging and counting labeled-peptide spots versus solution concentration; the data from three replicates at each peptide concentration, which ranged from 4 pM up to 100 pM, are plotted in Figure 3.4. Two control experiments were performed to check the validity of these results. First, to test whether any defects in the lipid bilayer might lead to anomalous binding results, the adsorption affinity of the Cy3B-labeled peptide to a clean glass substrate was measured and found to be a small fraction (15%) of that observed on a DPPC bilayer (see Supporting information in Appendix). These data show that GLP-1 interacting with glass at any defects in the lipid bilayer would be weakly adsorbed. A second control was performed to determine whether the combined Cy3B and PEG tether used for labeling would contribute to the affinity of the GLP-1 peptide for the lipid bilayer. A model compound was synthesized containing Cy3B-maleimide labeled cysteine bound to the 20-atom polyethylene-glycol linker. As shown in Supporting information in Appendix, this compound exhibited negligible affinity for a DPPC bilayer, producing spot densities that were 0.01% of those observed for the labeled GLP-1 peptide at equivalent solution concentrations.

The relationship between the number density of GLP-1 molecules interacting with the lipid bilayer and their solution concentration is linear, as shown in Figure 3.4, with a

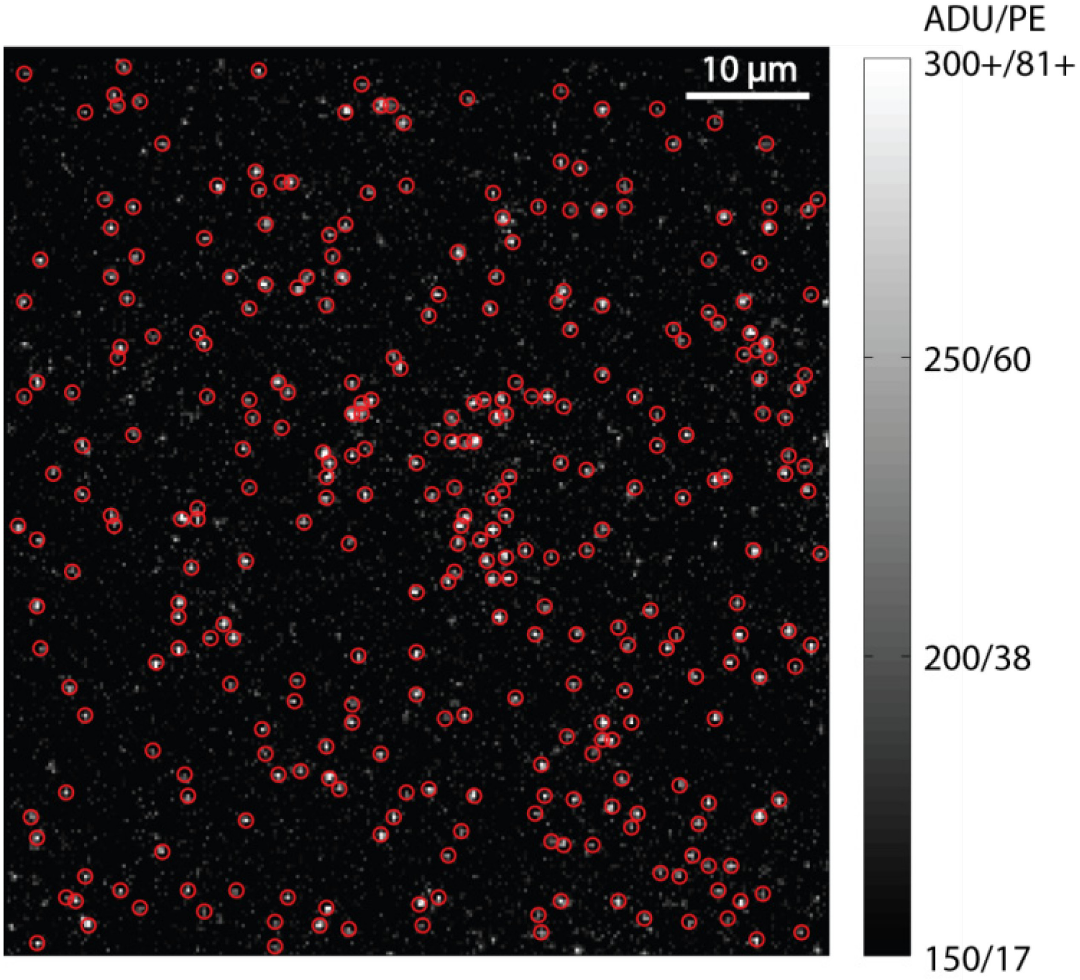

Figure 3.3 Fluorescence image (100 ms frame) of Cy3B-labeled GLP-1 associated with a DPPC supported lipid bilayer from a 50-pM solution of the peptide. The red circles indicate where molecular spots are identified based on the adjacent-pixel criterion. Gray scale indicates both analog-to-digital units (ADU) and photoelectrons (PE).

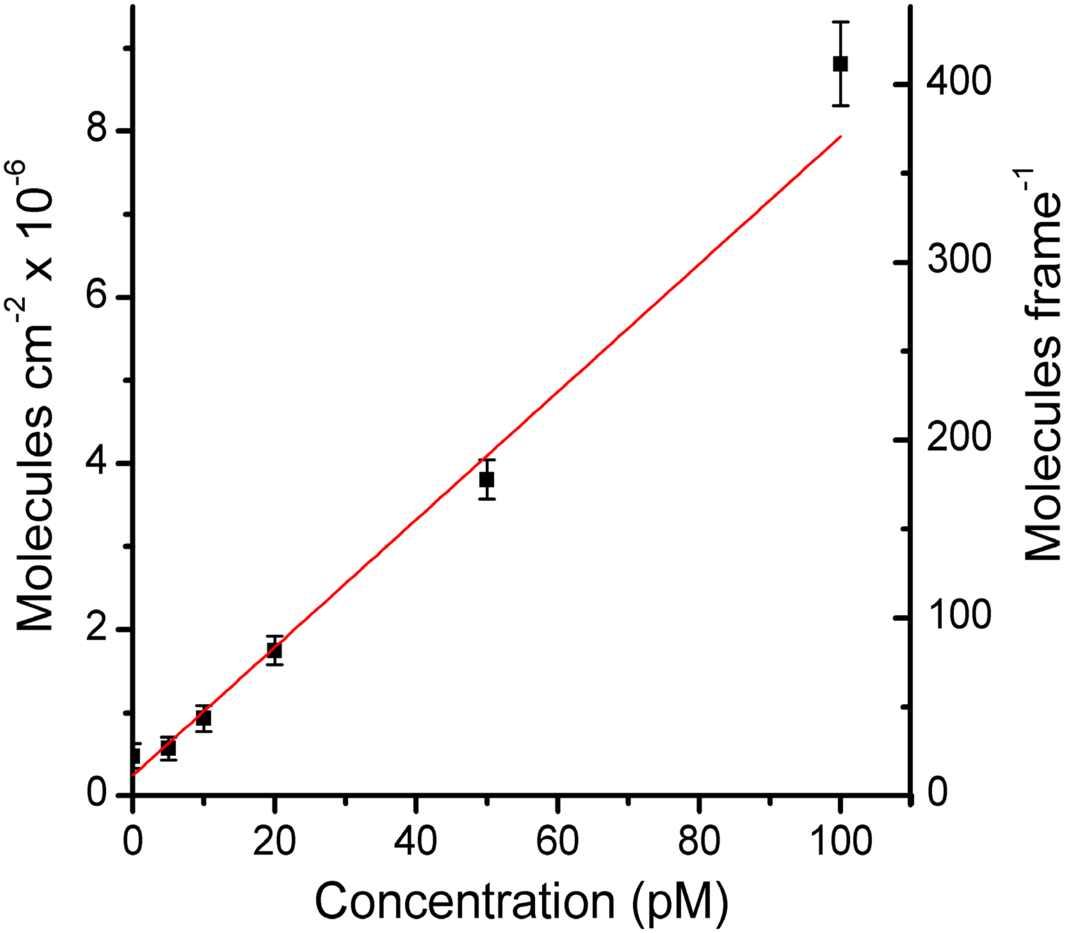

Figure 3.4 Isotherm plot of GLP-1 binding to a DPPC lipid bilayer. The average number of molecules in a 68 x 68 µm image (right axis) and the corresponding number density (left axis) are plotted versus solution concentration, together with a least-squares fitted straight line (red).

small intercept from fluorescent spots in the blank images. The slope of the isotherm data, $\Gamma/C = 2.2\ (\pm\ 0.1) \times 10^{17}$ cm^{-2} M^{-1} can be related to the equilibrium constant for GLP-1 binding to the lipid bilayer through a simple units conversion, $K_o =$ 1000 cm^{3} liter^{-1}$/C\ N_{Av} = 3.6\ (\pm 0.2) \times 10^{-4}$ cm or 3.6 μm. This result represents the distance into solution that contains the same number of molecules as reside at equilibrium in the lipid bilayer area below it.[19,20] This result not only characterizes the membrane-bound population and corresponding affinity of the peptide for the lipid bilayer at equilibrium, it is also needed to determine the rate of GLP-1 adsorption to the bilayer surface from solution (see below).

The linearity of the isotherm results in Figure 3.4 is consistent with a lack of spot overlap over this concentration range, which assures that the probability of any interrogated (9-pixel) region being doubly occupied is small. At a solution concentration of 50-pM GLP-1 used for residence-time kinetic experiments (see below), the density of molecular spots is 175 per frame, and their corresponding 9-pixel regions occupy a small fraction (2.5%) of the total image area. Based on a Poisson statistical model for spatially resolving spots in the image,[26,32] the expected number of overlapped spots at this surface coverage is 2.1 out of 175, corresponding to a probability of a spot being doubly-occupied of 1.2%. This result is critical to the kinetic model developed for the residence-time histograms (see above); the lack of doubly-occupied spots supports the assumption that there is a small probability of an additional molecule binding within an interrogated region before the original molecule leaves the membrane. This allows the adsorption rate, k_1, in the kinetic analysis of the residence times to be neglected.

3.4.2 Kinetics of GLP-1 binding to DPPC lipid bilayers

The observation of labeled GLP-1molecules bound to a lipid membrane provides not only a direct count of the membrane-associated peptide population but also the residence times of individual molecules, which allow the kinetics of their binding and unbinding to be determined. Residence times are determined by correlating the locations of detected fluorescent spots between frames, reporting the total length of time of a molecular visit. Single-frame events were neglected in the analysis, as were molecules present at the start or the end of the acquisition whose residence time is unknown.

From these data, a histogram of residence times is constructed where every event measured in an experiment is aligned on a common time axis, where each event begins at time zero (see Figure 3.2, above). In this cumulative histogram, all of the molecular events contribute to the total until the point in time when the molecule leaves the image. An example residence-time histogram is plotted in Figure 3.5, which shows the biexponential decay of the probability of individual GLP-1 peptides leaving the lipid bilayer.

From three replicates of the residence-time histogram experiment, the parameters from the fit of the data to the biexponential model, Equation 3.1, averaged as follows: $\tau_1 = 1.19 \pm 0.05$ s, $\tau_2 = 19 \pm 2$ s, and the preexponential fraction, $P_1 / (P_1+P_2) = 0.83 \pm 0.03$, where the average number of events measured in each histogram was 1200 ± 300. The apparent residence time of a labeled peptide in the lipid bilayer can be shortened by photobleaching of the dye label. The influence of photobleaching on the kinetic results was tested by acquiring residence-time data at several excitation laser powers. The results show that the measured time constants do not change within their uncertainties up

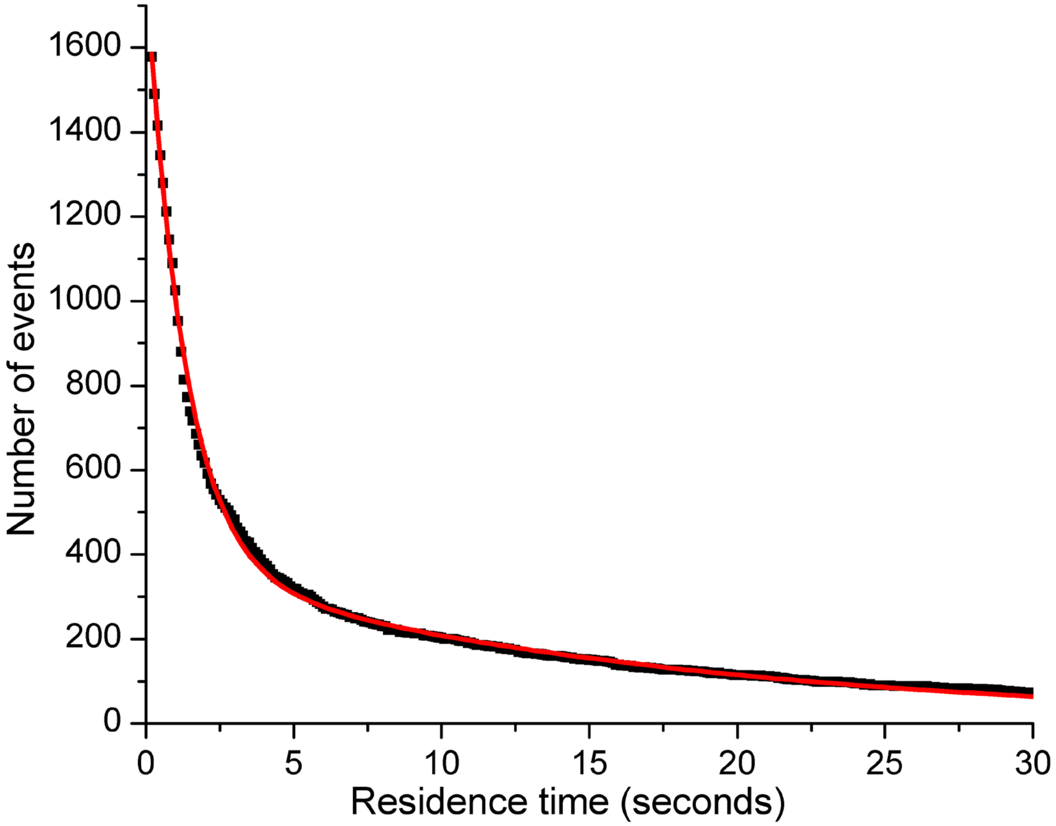

Figure 3.5 Example residence-time histogram for GLP-1 binding to a DPPC supported lipid bilayer. Data points (black) are fit to a biexponential model, Equation 3.1, with no offset (red line).

to a laser power of 4.5 mW, above which the longer time constant decreases significantly (see Supporting information in Appendix in Appendix). The reported isotherms and histograms were acquired with 3.0 mW excitation, well below the power level where photobleaching influences the measured residence times. Finally, the robustness of the kinetic parameters derived from residence-time histograms was tested by acquiring on different days, using different microscope systems, and with Cy3 and Cy3B labeling of the GLP-1 peptide. The results show remarkable consistency as shown in a tabulated comparison in Supporting information in Appendix.

The kinetic parameters, $P_1 / (P_1+P_2)$, $r_1 = 1/\tau_1$ and $r_2 = 1/\tau_2$, from the residence histogram above were substituted into Equations 3.5 – 3.7 to determine the microscopic rate constants for GLP-1 peptide association with a DPPC lipid bilayer. The rate constant for weakly associated peptides desorbing from the surface of the bilayer into solution was determined to be $k_2 = (7.0 \pm 0.2) \times 10^{-1}\ s^{-1}$, which corresponds to a desorption lifetime of 1.43 ± 0.04 s. Desorption from the lipid bilayer surface competes with intercalation of surface-associated peptides, transitioning to a strongly bound, folded state in the membrane, which occurs at a 5.4-fold slower rate, $k_3 = (1.3 \pm 0.2) \times 10^{-1}\ s^{-1}$. The ratio of this rate of intercalation to the sum of intercalation and desorption rates, $k_3/(k_2 + k3)$, is the fraction of peptides that adsorb to the membrane surface that successfully fold and intercalate into the membrane before they desorb. From the present results, this fraction of arriving peptides that intercalate is relatively small, 0.17 ± 0.3.

The rate constant for molecules emerging from the strongly bound, intercalated state to the weakly-associated, adsorbed state, k_4, $= (6.5 \pm 0.7) \times 10^{-2}\ s^{-1}$, is an order of magnitude slower than rate of desorption of GLP-1 from the lipid bilayer surface, k_2.

This result indicates that the intercalated population significantly lengthens the lifetime of GLP-1 in the membrane. Indeed, the majority of the GLP-1 peptide associated with the membrane at equilibrium is intercalated; this fraction is determined by the competition between intercalation of the adsorbed population and the rate of reemergence, where $k_3 / (k_3 + k_4) = 0.67$, indicates the fraction of GLP-1 population that is strongly bound. From the ratio of rates of reemergence and intercalation, one may calculate the Gibbs free energy difference between intercalated and surface adsorbed states of the peptide, where $\Delta G = -\mathrm{RT} \ln (k_3/k_4) = -1.7$ kJ mol^{-1} at 298 K. This small free energy difference likely represents a balance between the energy costs of creating free volume within the lipid bilayer and the reduction of conformational freedom of the peptide with changes in the degree of water contact with hydrophobic residues of the peptide, as it transfers from membrane-solution interface to the membrane interior.

The final rate constant to be determined from the data is for the adsorption of the peptide to the lipid bilayer from solution. This rate is found by substituting the effective off-rate for GLP-1 dissociation from the lipid bilayer, $[k_2 k_4 / (k_3 + k_4)]$, and the binding equilibrium constant determined from the accumulation isotherm, K_o into Equation 3.9. The resulting heterogeneous rate constant is $k_1 = (1.02 \pm 0.03) \times 10^{-4}$ cm s^{-1}. This rate constant can be compared with the frequency of collisions between molecules and the lipid bilayer to determine what fraction of the collisions lead to association of the peptide with the membrane. To predict the collision frequency, the diffusion coefficient of the peptide can be estimated by the Stokes-Einstein equation, where the peptide in solution is assumed to be a random coil[8-10] with a hydrodynamic radius, $r \sim 1.3$ nm.[33,34] From the Stokes-Einstein equation and the viscosity of water, the diffusion coefficient of the peptide at 298 K is estimated to be $D = k_B\ T/6\pi\eta r \sim 1.6 \times 10^{-6}\ \mathrm{cm}^2\ \mathrm{s}^{-1}$. The diffusion-controlled heterogeneous reaction velocity is predicted by Fick's first law[21] to be the flux through a unit area for a given solution concentration, $v = J/C = D(dC/dx)/C$, where the gradient, (dC/dx), is the bulk solution concentration divided by the encounter distance for reaction,[35] estimated to be about twice the hydrodynamic radius of the peptide. The bulk solution concentration thus cancels, and the diffusion-limited reaction velocity is estimated to be $v = J/dx \sim D/2r \sim 7\ \mathrm{cm\ s}^{-1}$. Dividing k_1 by the diffusion-limited rate provides an estimate of the fraction of collisions between the peptide and lipid bilayer surface that result in adsorption, $k_1/v \sim 1.5 \times 10^{-5}$. This result shows that adsorption of the GLP-1 peptide to the membrane is much slower than a diffusion-limited rate. It is limited by a significant free energy barrier to membrane association, which can be estimated from the ratio of the reaction rate compared to the diffusion limited reaction velocity, where $\Delta G^{\neq} = -RT \ln (k_1/v) \sim 28$ kJ/mol at 298K. This result represents the free-energy barrier for GLP-1 to associate with the lipid bilayer surface. It could arise from only a small fraction of peptide conformations being favorable to membrane association, changes in peptide solvation, and/or the requirement for phospholipids in the bilayer to adopt specific conformations to accommodate the adsorbed peptide.

3.5 Discussion

The present results illustrate the utility of measuring peptide residence times and populations on supported lipid bilayers by single-molecule imaging as a means of determining kinetics of their membrane surface association and intercalation. With careful attention to detection criteria, absolute populations of membrane-associated peptides can be measured at very low concentrations in solution and on the membrane surface, typical of physiological conditions. The microscopic rates determined from the residence-time analysis provide insight into the dynamics controlling the membrane-bound population of peptide, the fraction that is intercalated, and rates of transfer between the membrane-solution interface and a folded-state within the membrane interior. The membrane catalysis model[1-3] suggests that membrane-bound peptides are critical to cell signaling because the conformational changes accompanying membrane binding can pre-fold the peptide and facilitate receptor interactions within the membrane. In support of this hypothesis, the recently reported crystal structure of GLP-1 co-crystalized with the extracellular domain of the GLP-1 receptor has shown that the peptide also adopts an alpha helix conformation when bound to the receptor.[12] Furthermore, Exendin-4, an effective agonist for the GLP-1 receptor commercially produced for treatment of diabetes shares 50% sequence homology with GLP-1, but exhibits greater helical structure in n aqueous solution.[9,10] The tendency of this peptide to adopt an alpha-helix conformation prior to membrane affiliation may contribute to its efficacy. Measuring the membrane binding interactions and rates of those interactions of Exendin-4 or similar drug candidate peptides could provide important insight into their structure-activity relationships.

A limitation of the present GLP-1 results is that the peptide binding to the DPPC lipid bilayer was measured at 22°C, a temperature below the 42°C gel-to-liquid-crystal phase transition of DPPC.[36] Fluid or ripple phase lipids behave more like natural membranes than the gel-phase DPPC,[37,38] and the effects of the lipid phase and composition on the kinetics peptide insertion would be an important goal for future work.

These experiments introduce a measurement challenge, namely diffusion of the bound peptide in the fluid membrane environment. Peptide diffusion in gel-phase DPPC is minimal, which eases the measurement of residence times of stationary fluorescent spots; diffusion of peptides in a fluid membrane will require tracking of molecules over time in order to report residence times.[39-41] Lateral diffusion of peptides in a membrane could be readily quantified and may provide additional information to characterize peptide-membrane interactions, including resolving the weakly and strongly bound states based on differences in their lateral mobility. As was successfully demonstrated for single-stranded DNA diffusing at solid-liquid interfaces,[42] it may also be possible to measure resonance energy transfer between different fluorescent labels on the C- and N-termini of the GLP-1 peptide to discriminate between random coil and alpha-helix conformations of the peptide in the membrane.

The development of the mathematical relationships between residence-time histograms, surface-bound populations, and the microscopic rates of the three-state kinetic model should be broadly applicable to other areas of interfacial chemistry where an adsorbed molecule can transition to a more tightly bound state. The solutions to these differential equations are also relevant to wash-off experiments commonly used in sensor development, where a surface is first equilibrated against a given solution concentration and then subjected to a concentration step to zero. This step is usually accomplished by flushing the reacted surface with buffer, while the decay in the remaining surface-bound concentration of molecules is measured over time.

The boundary conditions of such an experiment are, first, that the surface is at equilibrium with the solution at time zero. In other words, the initial fractions of weekly and strongly associated species are given by their equilibrium values:

$$W(0) = \frac{k_4}{k_3 + k_4} \qquad [3.10a]$$

$$S(0) = \frac{k_3}{k_3 + k_4} \qquad [3.10b]$$

The second initial condition in the wash-off experiment is the same as for residence-time histograms: no molecules revisit the surface after unbinding, or in other words, k_1 is zero. When these initial conditions are applied to the general solutions in Equations A1.2-6 in Supporting information in Appendix, the counterpart to Equation 3.1 for the sum of the populations of molecules in the W and S states remaining after the beginning of a wash-off has the identical form as Equation 3.1, a biexponential decay without offset:

$$R(t) = P_{1R} e^{-r_1 t} + P_{2R} e^{-r_2 t} \qquad [3.11]$$

where r_1 and r_2 are given by Equations 3.3a and 3.3b, and P_{1R} and P_{2R} for the normalized function are given by:

$$P_{1R} = \frac{k_2 - k_3 - k_4 + (r_1 - r_2)}{2(r_1 - r_2)} - \frac{k_2 k_3}{(r_1 - r_2)(k_3 + k_4)} \qquad [3.12a]$$

$$P_{2R} = \frac{-k_2 + k_3 + k_4 + (r_1 - r_2)}{2(r_1 - r_2)} + \frac{k_2 k_3}{(r_1 - r_2)(k_3 + k_4)} \qquad [3.12b]$$

It can be shown that the derivative of this counterpart expression is proportional to Equation 3.1, and when both are normalized, the constant of proportionality is the effective desorption rate: the product of the microscopic rate constant, k_2, and the fraction of molecules in the W state at equilibrium:

$$-\partial/_{\partial t} R(t) = r_1 P_{1R} e^{-r_1 t} + r_2 P_{2R} e^{-r_2 t} = \frac{k_2 k_4}{k_3 + k_4} H(t) \qquad [3.13]$$

The derivative of an exponential is equal to the exponential times the derivative of the exponential argument, thus to convert the preexponential terms of the wash-off experiment to the equivalent histogram preexponentials, one need only scale the results by the corresponding rate constant and evaluate the measured rates and preexponential values according to Equations 3.5-3.7 above to determine the microscopic rate constants, $k_2 - k_4$.

The single-molecule imaging experiment has several advantages over a typical wash-off experiment. One advantage is that single-molecule imaging can report densities of bound molecules on the surface, while typical wash-off experiments are carried out at surface densities much too large for imaging and counting single molecules, so that determining the equilibrium constant, K_o, is challenging. More importantly, single-molecule residence-time measurements are carried out at equilibrium and thus do not require a concentration step of a wash-off experiment to measure unbinding kinetics. In practice, slow mass transfer through the unstirred boundary layer near the surface makes it difficult to quickly remove molecules from the solid/liquid interface, in order to prevent the re-binding of molecules liberated from the surface. Thus, the condition that k_1 is zero during the wash-off experiment may not be met, and the decay in population of molecules on the surface is confounded by rebinding from solution and the slow mass transfer of molecules away from the surface.

3.6 References

(1) Sargent, D. F.; Schwyzer, R. *Proceedings of the National Academy of Sciences of the United States of America* **1986**, *83*, 5774.

(2) Castanho, M. A. R. B.; Fernandes, M. X. *European Biophysics Journal* **2006**, *35*, 92.

(3) Langelaan, D. N.; Rainey, J. K. *Biochemistry & Cell Biology* **2010**, *88*, 203.

(4) Grieve, D. J.; Cassidy, R. S.; Green, B. D. *British Journal of Pharmacology* **2009**, *157*, 1340.

(5) Van Gaal, L. F.; Gutkin, S. W.; Nauck, M. A. *European Journal of Endocrinology* **2008**, *158*, 773.

(6) MacDonald, P. E.; El-kholy, W.; Riedel, M. J.; Salapatek, A. M. F.; Light, P. E.; Wheeler, M. B. *Diabetes* **2002**, *51*, S434.

(7) Wieprecht, T.; Apostolov, O.; Beyermann, M.; Seelig, J. *Journal of Molecular Biology* **1999**, *294*, 785.

(8) Thornton, K.; Gorenstein, D. G. *Biochemistry* **1994**, *33*, 3532.

(9) Neidigh, J. W.; Fesinmeyer, R. M.; Prickett, K. S.; Andersen, N. H. *Biochemistry* **2001**, *40*, 13188.

(10) Andersen, N. H.; Brodsky, Y.; Neidigh, J. W.; Prickett, K. S. *Bioorganic & Medicinal Chemistry* **2002**, *10*, 79.

(11) Xiaoqing, C.; Danielle, K.; Søren, B.; Jens, J. L. *Magnetic Resonance in Chemistry* **2001**, *39*, 477.

(12) Underwood, C. R.; Garibay, P.; Knudsen, L. B.; Hastrup, S.; Peters, G. H.; Rudolph, R.; Reedtz-Runge, S. *Journal of Biological Chemistry* **2010**, *285*, 723.

(13) Constantinescu, I.; Lafleur, M. *Biochimica et Biophysica Acta* **2004**, *1667*, 26.

(14) Papo, N.; Shai, Y. *Biochemistry* **2003**, *42*, 458.

(15) Fox, C. B.; Wayment, J. R.; Myers, G. A.; Endicott, S. K.; Harris, J. M. *Analytical Chemistry* **2009**, *81*, 5130.

(16) Lowry, T. M.; John, W. T. *Journal of the Chemical Society, Transactions* **1910**, *97*, 2634.

(17) Wei, J.; Prater, C. D. In *Advances in Catalysis*; Eley, D. D., Selwood, P. W., Weisz, P. B., Eds.; Academic Press: New York, NY, 1962; Vol. Volume 13, p 203.

(18) Capellos, C. *Kinetic Systems: Mathematical Description of Chemical Kinetics in Solution*; New York : Wiley-Interscience: New York, 1972.

(19) Hansen, R. L. *Anal Chem* **1998**, *70*, 4247.

(20) Starr, T. E.; Thompson, N. L. *Biophys J* **2001**, *80*, 1575.

(21) Bard, A. J.; Faulkner, L. R. *Electrochemical Methods: Fundamentals and Applications*; 2 ed.; Wiley: New York, 2001.

(22) Charitat, T.; Bellet-Amalric, E.; Fragneto, G.; Graner, F. *Eur Phys J B* **1999**, *8*, 583.

(23) Starr, T. E.; Thompson, N. L. *Langmuir* **2000**, *16*, 10301.

(24) Tamm, L. K.; McConnell, H. M. *Biophysical Journal* **1985**, *47*, 105.

(25) Wayment, J. R.; Harris, J. M. *Analytical Chemistry* **2008**, *81*, 336.

(26) Peterson, E. M.; Harris, J. M. *Analytical Chemistry* **2010**, *82*, 189.

(27) Ambrose, W. P.; Goodwin, P. M.; Martin, J. C.; Keller, R. A. *Physical Review Letters* **1994**, *72*, 160.

(28) Lu, H. P.; Xie, X. S. *Nature* **1997**, *385*, 143.

(29) Yip, W.-T.; Hu, D.; Yu, J.; Bout, D. A. V.; Barbara, P. F. *Journal of Physical Chemistry A* **1998**, *102*, 7564.

(30) Gensch, T.; Böhmer, M.; Aramendía, P. F. *Journal of Physical Chemistry A* **2005**, *109*, 6652.

(31) Gao, F.; Mei, E.; Lim, M.; Hochstrasser, R. M. *Journal of the American Chemical Society* **2006**, *128*, 4814.

(32) Hanley, D. C.; Harris, J. M. *Analytical Chemistry* **2001**, *73*, 5030.

(33) Sun, S.; Luo, N.; Ornstein, R. L.; Rein, R. *Biophysical Journal* **1992**, *62*, 104.

(34) Zagrovic, B.; Jayachandran, G.; Millett, I. S.; Doniach, S.; Pande, V. S. *Journal of Molecular Biology* **2005**, *353*, 232.

(35) Rice, S. A. In *Comprehensive Chemical Kinetics*; Bramford, C. H., Tipper, C. F. H., Compton, R. G., Eds.; Elsevier: Amsterdam, 1985; Vol. 25.

(36) Koynova, R.; Caffrey, M. *Biochimica et Biophysica Acta* **1998**, *1376*, 91.

(37) Pott, T.; Dufourcq, J.; Dufourc, E. J. *European Biophysics Journal* **1996**, *25*, 55.

(38) Sekharam, K. M.; Bradrick, T. D.; Georghiou, S. *Biochimica et Biophysica Acta* **1991**, *1063*, 171.

(39) Ishihara, A.; Jacobson, K. *Biophysical Journal* **1993**, *65*, 1754.

(40) Simson, R.; Sheets, E. D.; Jacobson, K. *Biophysical Journal* **1995**, *69*, 989.

(41) Saxton, M. J.; Jacobson, K. *Annual Reviews in Biophysics and Biomolecular Structure* **1997**, *26*, 373.

(42) Kastantin, M.; Schwartz, D. K. *ACS Nano* **2011**, *5*, 9861.

APPENDIX

SUPPORTING INFORMATION FOR MICROSCOPIC RATES OF PEPTIDE-PHOSPHOLIPID BILAYER INTERACTIONS FROM SINGLE-MOLECULE RESIDENCE TIMES

TABLE OF CONTENTS

A1 Analysis of the Differential Equations for Single-Molecule Binding

A1.1 General system of differential equations

The system of differential equations associated with three-state consecutive reversible first-order kinetics includes three expressions for the rate of change of the number of molecules in each of the three states as shown here in linear algebra form, given as the dot product of the microscopic rate coefficient matrix with a vector of the instantaneous concentrations (volume and surface) of the three populations:

$$\begin{pmatrix} \partial F/\partial t \\ \partial W/\partial t \\ \partial S/\partial t \end{pmatrix} = \begin{pmatrix} -k_1\lambda^{-1} & k_2\lambda^{-1} & 0 \\ k_1 & -k_2 - k_3 & k_4 \\ 0 & k_3 & -k_4 \end{pmatrix} \bullet \begin{pmatrix} F(t) \\ W(t) \\ S(t) \end{pmatrix}$$

[A1.1]

where, k_1 is the heterogeneous rate constant for molecules binding to the surface from the solution, k_2 is the rate constant for molecules unbinding from the surface, λ^{-1} is the ratio of the surface area of the bilayer to the volume of the system that accounts for the change in dimensionality for going from volume of solution to the surface area of bilayer, k_3 is the rate constant for molecules changing from the weakly bound to the strongly bound state. For example, the rate of change of the number of molecules in the S state, $\partial S/\partial t$, is given by $k_3\, W(t) - k_4\, S(t)$. The solutions to this system of differential equations for the functions representing the time dependence of the number of molecules of each of the components have the following general form: $X(t) = X_{eq} + P_{1X}e^{-r_1 t} + P_{2X}e^{-r_2 t}$, where the equilibrium and preexponential coefficient terms are complicated functions of the microscopic rate constants, k_1 through k_4, and are unique for each component. In contrast, the rate terms, r_1 and r_2, are the same for all components and are given[1] by the following equations:

$$r_1 = \frac{1}{2}[k_1\lambda^{-1} + k_2 + k_3 + k_4 + \sqrt{(k_1\lambda^{-1} + k_2 + k_3 + k_4)^2 - 4(k_1k_3\lambda^{-1} + k_1k_4\lambda^{-1} + k_2k_4}\,]$$

[A1.2a]

$$r_2 = \frac{1}{2}[k_1\lambda^{-1} + k_2 + k_3 + k_4 - \sqrt{(k_1\lambda^{-1} + k_2 + k_3 + k_4)^2 - 4(k_1k_3\lambda^{-1} + k_1k_4\lambda^{-1} + k_2k_4}\,] \qquad \text{[A1.2b]}$$

Note that, as written, r_1 will always be larger than r_2. These rate expressions can be recognized as the eigenvalues[2] of the coefficient matrix from Equation A1.1, or as roots[3] of the quadratic equation: $y = x^2 - (k_1\lambda^{-1} + k_2 + k_3 + k_4)x + (k_1k_3\lambda^{-1} + k_1k_4\lambda^{-1} + k_2k_4)$ Interestingly, the sum of r_1 and r_2 is equal to the sum of the microscopic rate constants, $k_1\lambda^{-1} + k_2 + k_3 + k_4$. The difference between r_1 and r_2 is equal to the radical term in either of the rate expressions, and the product of r_1 and r_2 is equal to $(k_1k_3\lambda^{-1} + k_1k_4\lambda^{-1} + k_2k_4)$.

The preexponential coefficients corresponding to the two rates, r_1 and r_2, for each of the three components are given as follows:

$$P_{1F} = \frac{\begin{pmatrix} -k_1\lambda^{-1}(-k_2k_3 - (k_3 + k_4)(k_3 + k_4 + r_1 - r_2) + r_1r_2)F(0) \\ +k_2(k_1k_3\lambda^{-1} - k_4(k_3 + k_4 + r_1 - r_2) + r_1r_2)W(0) - 2r_1k_2k_4S(0) \end{pmatrix}}{2r_1r_2(r_1 - r_2)} \qquad \text{[A1.3a]}$$

$$P_{2F} = \frac{\begin{pmatrix} k_1\lambda^{-1}(-k_2k_3 - (k_3 + k_4)(k_3 + k_4 - r_1 + r_2) + r_1r_2)F(0) \\ -k_2(k_1k_3\lambda^{-1} - k_4(k_3 + k_4 - r_1 + r_2) + r_1r_2)W(0) + 2r_2k_2k_4S(0) \end{pmatrix}}{2r_1r_2(r_1 - r_2)} \qquad \text{[A1.3b]}$$

$$P_{1W} = \frac{\begin{pmatrix} -k_1\lambda^{-1}\left(k_1k_3\lambda^{-1} - k_4(k_3 + k_4 - r_1 + r_2) + r_1r_2\right)F(0) \\ -\begin{pmatrix} k_1^2k_3\lambda^{-2} - k_2k_4(1 + k_2 + k_3 - k_4 + r_1 - r_2) + r_1r_2 \\ -k_1\lambda^{-1}\left(k_3^2 + (1 + k_2)k_4 + k_3(1 + k_2 + k_4 + r_1 - r_2)\right) \end{pmatrix} W(0) \\ +2k_4(k_1^2\lambda^{-2} - 3k_2k_4 + k_1\lambda^{-1}(k_2 - 2k_3 - 2k_4 - r_1 + r_2))S(0) \end{pmatrix}}{2r_1r_2(r_1 - r_2)} \qquad \text{[A1.3c]}$$

$$P_{2W} = \frac{\begin{pmatrix} k_1\lambda^{-1}(k_1k_3 - k_4(k_3 + k_4 + r_1 - r_2) + r_1r_2)F(0) \\ +\begin{pmatrix} k_1^2k_3\lambda^{-2} - k_2k_4(1 + k_2 + k_3 - k_4 - r_1 + r_2) + r_1r_2 \\ -k_1\lambda^{-1}\left(k_3^2 + (1 + k_2)k_4 + k_3(1 + k_2 + k_4 - r_1 + r_2)\right) \end{pmatrix} W(0) \\ -2k_4(k_1^2\lambda^{-2} - 3k_2k_4 + k_1(k_2 - 2k_3 - 2k_4 - r_1 + r_2))S(0) \end{pmatrix}}{2r_1r_2(r_1 - r_2)}$$

[A1.3d]

$$P_{1S} = \frac{\begin{pmatrix} -2k_1k_3r_1F(0)\lambda^{-1} \\ -k_3\left(k_1^2\lambda^{-2} - k_2k_4 + r_1 + r_2 + k_1\lambda^{-1}(k_2 + r_1 - r_2)\right)W(0) \\ +k_4(k_1^2\lambda^{-2} + r_1 + r_2 + k_1\lambda^{-1}(2k_2 + r_1 - r_2) + k_2(k_2 + k_3 + r_1 - r_2))S(0) \end{pmatrix}}{2r_1r_2(r_1 - r_2)}$$

[A1.3e]

$$P_{2S} = \frac{\begin{pmatrix} 2k_1k_3r_2F(0)\lambda^{-1} \\ +k_3\left(k_1^2\lambda^{-2} - k_2k_4 + r_1 + r_2 + k_1\lambda^{-1}(k_2 - r_1 + r_2)\right)W(0) \\ -k_4(k_1^2\lambda^{-2} + r_1 + r_2 + k_1\lambda^{-1}(2k_2 - r_1 + r_2) + k_2(k_2 + k_3 - r_1 + r_2))S(0) \end{pmatrix}}{2r_1r_2(r_1 - r_2)}$$

[A1.3f]

where *F*(*0*), *W*(*0*), and *S*(*0*) are the initial solution and surface concentrations in their respective states. At sufficiently long times ($t \gg 1/r_2$), the relative concentrations of each of the three components evolve from their initial concentrations to their equilibrium values, which are given by the following equations,[1] normalized to the total number of molecules in the system:

$$F_{eq} = \frac{k_2k_4}{k_2k_4 + k_1k_3\lambda^{-1} + k_1k_4\lambda^{-1}}$$

[A1.4]

$$W_{eq} = \frac{k_1 k_4}{k_2 k_4 + k_1 k_3 \lambda^{-1} + k_1 k_4 \lambda^{-1}} \qquad [A1.5]$$

$$S_{eq} = \frac{k_1 k_3}{k_2 k_4 + k_1 k_3 \lambda^{-1} + k_1 k_4 \lambda^{-1}} \qquad [A1.6]$$

The equilibrium expressions in Equations A1.4 through A1.6 are useful for interpreting isotherm experiments, where the interfacial concentration of molecules is measured versus the solution concentration. The sum, $W_{eq} + S_{eq}$, is the total population density on the surface. The slope of the measured isotherm is the equilibrium constant for binding, , which is the ratio of the total surface density of molecules, $W_{eq} + S_{eq}$, to the concentration in solution, F_{eq}:

$$K_0 = \frac{W_{eq} + S_{eq}}{F_{eq}} = \frac{k_1 k_4 + k_1 k_3}{k_2 k_4} \qquad [A1.7]$$

Solving this equation for k_1:

$$k_1 = K_0 \frac{k_2 k_4}{k_3 + k_4} \qquad [A1.8]$$

Allows the adsorption rate, k_1, to be determined from the slope of the isotherm and the values of k_2, k_3, and k_4 obtained from single-molecule histograms as described in the following section.

A1.2. Analysis of single-molecule residence-time histograms.

Two kinetic constraints are present in the histograms of residence times of molecular visits to the interface. First, by aligning the observed events to a common origin at $t = 0$, an initial condition arises for the normalized population where $W(0) = 1$ and $S(0) = 0$. A second constraint derives from the low surface densities interrogated in these experiments so the adsorption rate can be neglected in the analysis, $k_1 = 0$ (see discussion in the main body of the manuscript). These constraints greatly simplify Equations A1.2 and A1.3. When k_1 and $S(0)$ are zero, the rate terms r_1 and r_2 are given by:

$$r_1 = \frac{1}{2}[k_2 + k_3 + k_4 + \sqrt{(k_2 + k_3 + k_4)^2 - 4k_2k_4}\,] \qquad \text{[A1.9a]}$$

$$r_2 = \frac{1}{2}[k_2 + k_3 + k_4 - \sqrt{(k_2 + k_3 + k_4)^2 - 4k_2k_4}\,] \qquad \text{[A1.9b]}$$

The preexponential coefficient terms for the number of molecules in the W state are given by:

$$P_{1W} = \frac{k_2 + k_3 - k_4 + (r_1 - r_2)}{2(r_1 - r_2)} \qquad \text{[A1.10a]}$$

$$P_{2W} = \frac{-k_2 - k_3 + k_4 + (r_1 - r_2)}{2(r_1 - r_2)} \qquad \text{[A1.10b]}$$

while the preexponential coefficients for molecules in the S state are simpler expressions:

$$P_{1S} = -\frac{k_3}{(r_1 - r_2)} \qquad \text{[A1.11a]}$$

$$P_{2S} = \frac{k_3}{(r_1 - r_2)} \qquad \text{[A1.11b]}$$

The sums of the first and second preexponential terms for the W and S states are equivalent to the preexponential terms for the W state with the exception of a sign change on the k_3 term in the numerators:

$$P_{1W+S} = \frac{k_2 - k_3 - k_4 + (r_1 - r_2)}{2(r_1 - r_2)} \qquad \text{[A1.12a]}$$

$$P_{2W+S} = \frac{-k_2 + k_3 + k_4 + (r_1 - r_2)}{2(r_1 - r_2)} \qquad \text{[A1.12b]}$$

Equations A1.9a, A1.9b, A1.12a and A1.12b are the rate constants and normalized preexponential terms for the bi-exponential decay in the molecular population on the surface represented by the histogram plot of the residence times of molecules, given as follows:

$$H(t) = P_{1W+S}e^{-r_1 t} + P_{2W+S}e^{-r_2 t} \qquad \text{[A1.13]}$$

When the system of these four equations are solved for k_2, k_3, and k_4 in terms of P_1, P_2, r_1, and r_2, the relationships given in Equations 3.5-7 in the main body of this article are found which allow the interpretation of single-molecule residence-time histograms in terms of the microscopic rates of desorption, intercalation, and emergence. It is interesting to note that the conditions of this special case do not require the surface to be at equilibrium with the solution at any time during the course of the experiment as long as the free solution concentration, F, remains sufficiently low that the adsorption rate can be neglected.

A1.3. References

(1) Lowry, T. M.; John, W. T. *Journal of the Chemical Society, Transactions* **1910**, *97*, 2634.

(2) Wei, J.; Prater, C. D. In *Advances in Catalysis*; Eley, D. D., Selwood, P. W., Weisz, P. B., Eds.; Academic Press: New York, NY, 1962; Vol. Volume 13, p 203.

(3) Capellos, C. *Kinetic Systems: Mathematical Description of Chemical Kinetics in Solution*; New York : Wiley-Interscience: New York, 1972.

Figure A2 MALDI analysis of Cy3B-labeled GLP1. The HPLC-purified product was analyzed with time-of-flight matrix-assisted laser desorption ionization time-of-flight mass spectrometry (MALDI-TOF) in positive ion mode. The labeled peptide consists of the 30-residues of GLP-1 (HAEGTFTSDVSSYLEGQAAKEFIA WLVKGR), connected at the C-terminus to a Novabiochem (01-63-0141) bifunctional 20-atom PEG_2 spacer connected to a single amide-capped cysteine labeled at the thiol with GE Amersham (PA63131) Cy3B maleimide. At neutral pH the entire construct is zwitterionic with a total molecular weight of 4401.10. The singly-protonated species observed in positive-ion mode mass spectrometry has a molecular weight of 4402.93 with a calculated exact mass for the most abundant peak of 4402.11. The doubly-protonated species is also detected, which has an exact mass-to-charge ratio of 2201.56. A small amount of unlabeled peptide-linker-cysteine (<20% of total intensity) is also observed at a mass of 3720.03, however because experiments are run at surface coverages well below saturation ($<10^{-6}$), the competition of unlabeled peptide for binding sites on the lipid bilayer is negligible. Peptide concentrations were determined based only on the labeled peptide population; free label was previously removed by HPLC.

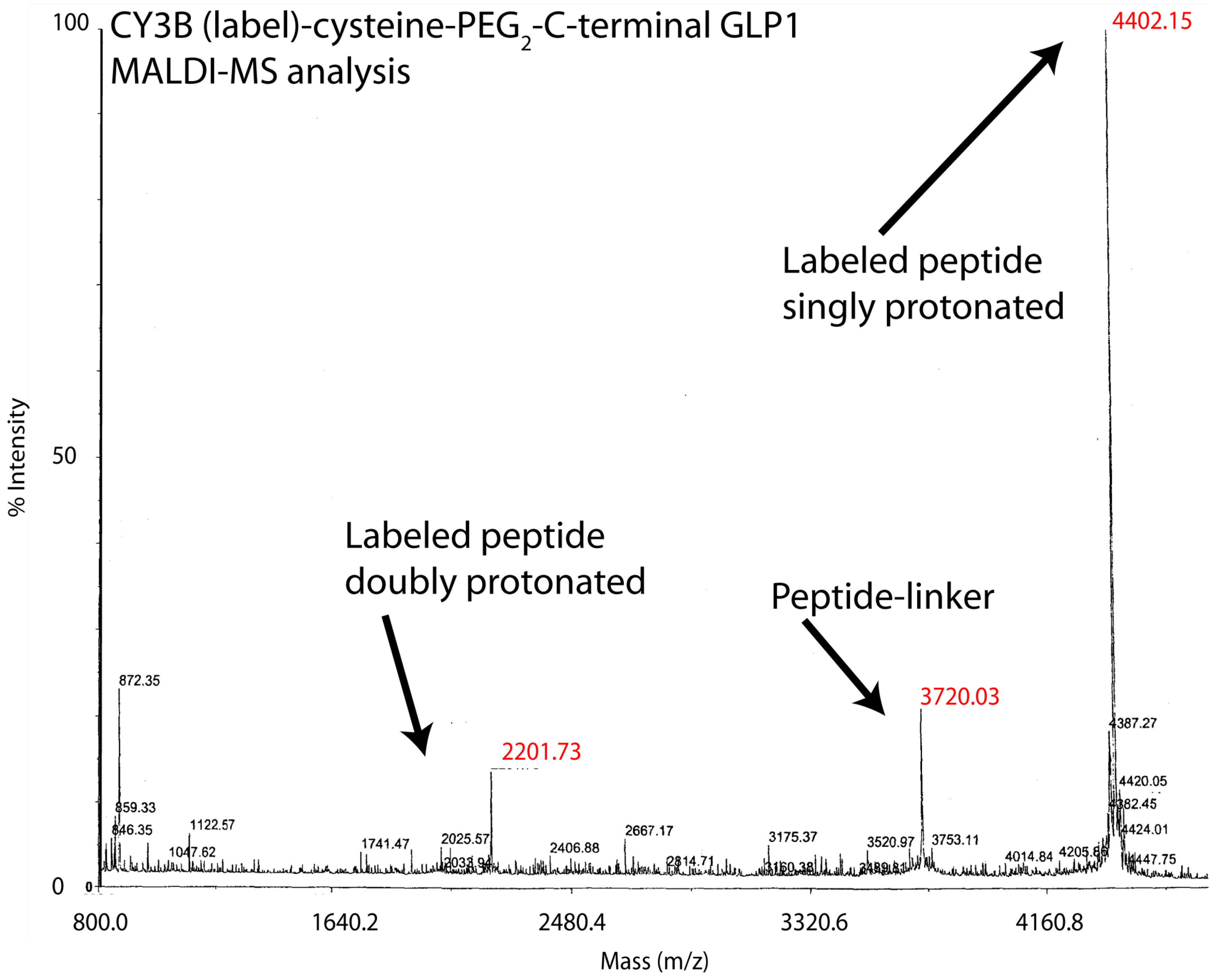

CY3B (label)-cysteine-PEG$_2$-C-terminal GLP1 MALDI-MS analysis

Labeled peptide singly protonated

Labeled peptide doubly protonated

Peptide-linker

Figure A3 Optimization of Imaging Algorithm to Bridge Photoblinking Events.

(A) Plots of k_1 and its first and second derivatives, as a function of bridge parameter, where single-molecule residence-time histograms were constructed for each bridge parameter and the results fit to Equation 3.1. The value of k_1 was calculated from Equation 3.9 using the parameters r_1, r_2, P_1, and P_2 from the histograms. First and second derivatives approach zero when the bridge parameter is increased to ten frames.

A1.2B. Plot of the number of molecules estimated to appear in a 9-pixel region from a 50-pM solution at the rate k_1 from 'A' during the bridge time on the x-axis. When the bridge parameter is ten frames, the probability of a second molecule appearing in a 9-pixel region during a bridge of 10 frames or 1.0 sec is ~2.2%.

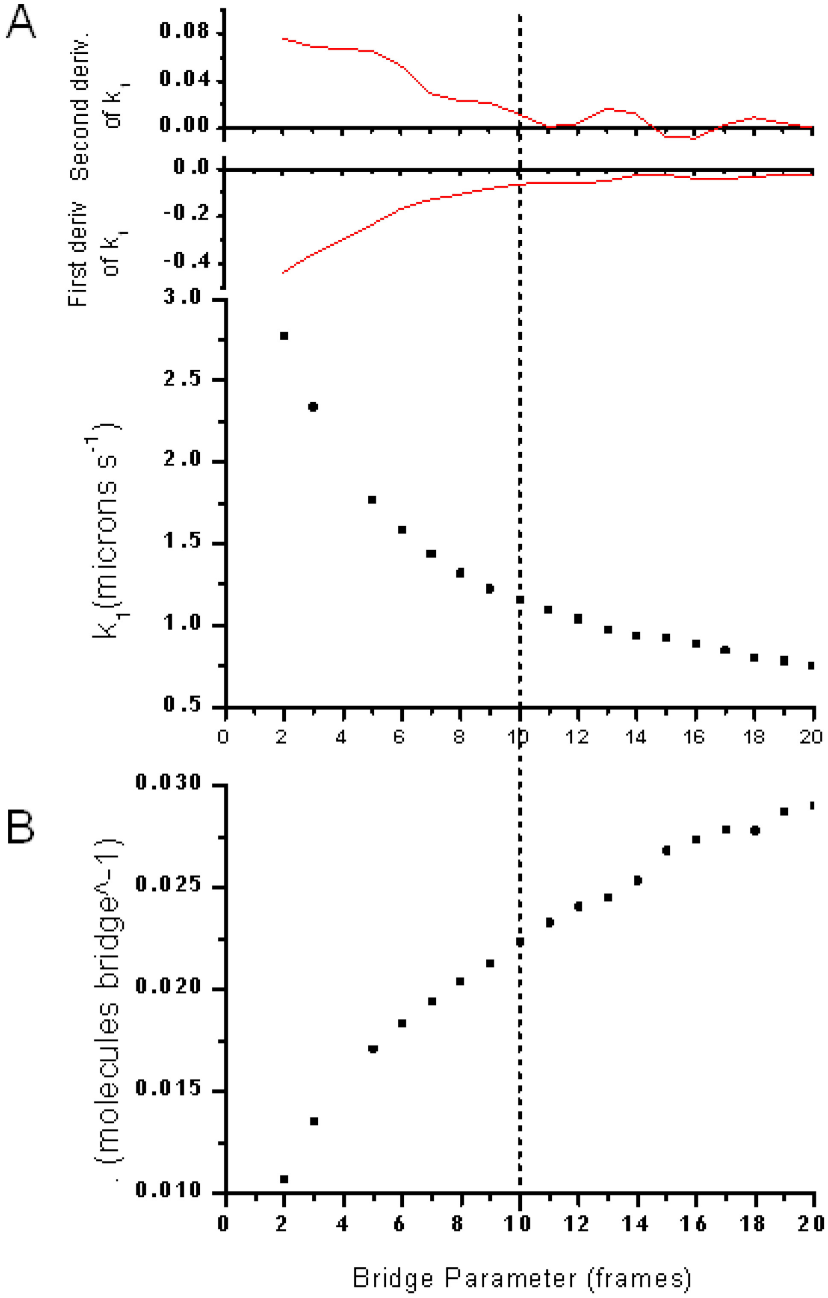
A
Second deriv. of k₁
0.08
0.04
0.00
First deriv of k₁
0.0
-0.2
-0.4
k₁(microns s⁻¹)
3.0
2.5
2.0
1.5
1.0
0.5
0
2
4
6
8
10
12
14
16
18
20
B
(molecules bridge^-1)
0.030
0.025
0.020
0.015
0.010
Bridge Parameter (frames)

Figure A4 Intensity Distributions of Cy3B-labeled GLP-1 Fluorescence Spots.

A. Distribution of the brightest pixel intensity of labeled-GLP1 fluorescence spots. The mean intensity is 87 photoelectrons (PEs). By fitting the distribution to a Gaussian convoluted with a single-sided exponential, the probability of an event being below the 37-PE critical level (3.0-standard deviations above background) is estimated to be 1.8%. B. Distribution of the next-brightest or threshold pixel intensity of labeled-GLP1 fluorescence spots. The mean intensity of this next-brightest pixel distribution is 66 PEs, and the probability of an event being below the 37-PE critical level is 6.9%. Note that integrated area fractions have a y-axis scale change at the line break.

A. Central bright pixel intensity distribution

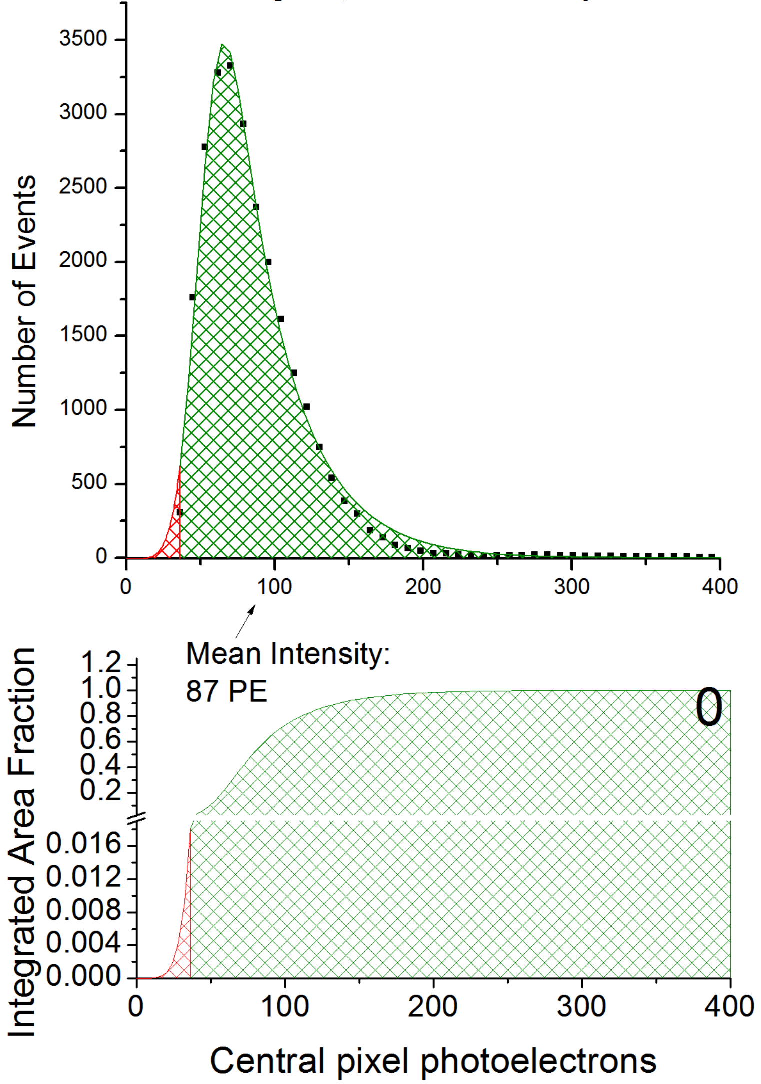

B.Threshold pixel intensity distribution

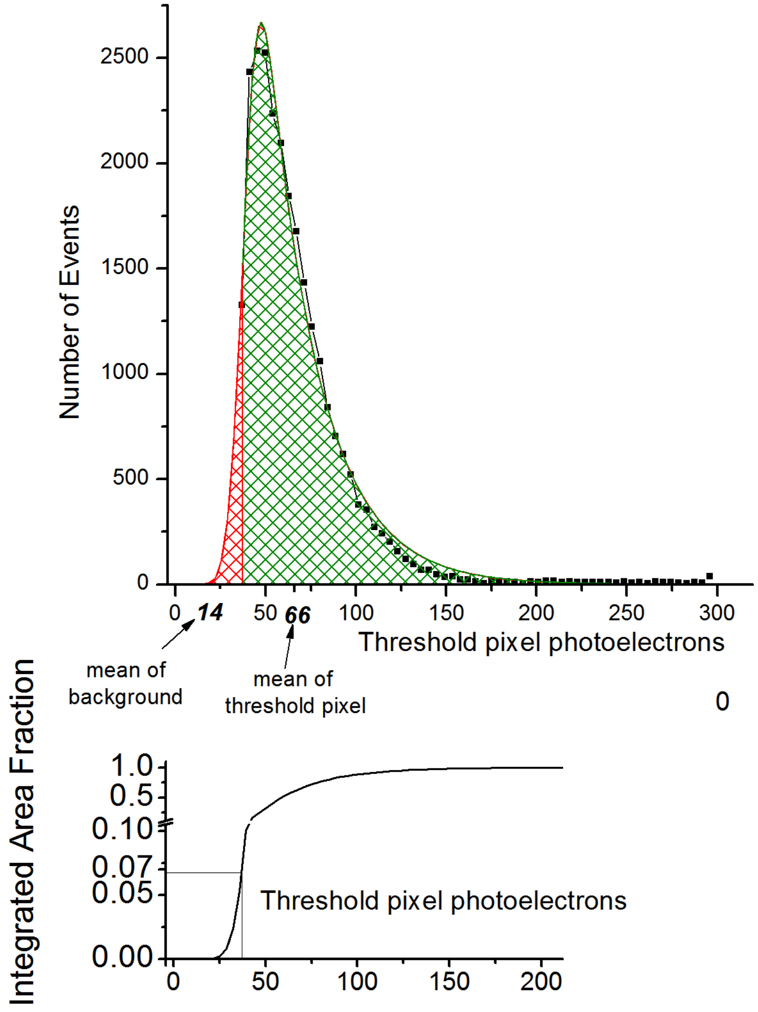

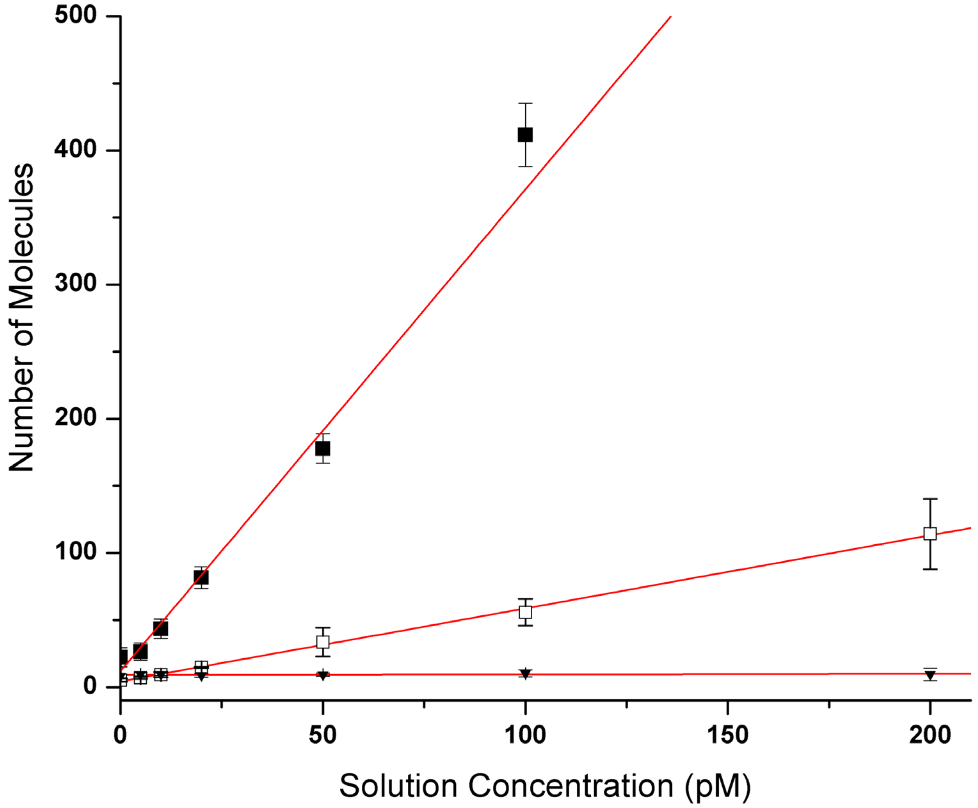

Figure A5. Isotherms Comparing the Binding of Cy3B-labeled GLP-1 to DPPC with Control Samples. Top line (solid squares) is the binding of Cy3B-labeled GLP-1 to a DPPC bilayer; slope of the fitted line is 3.6 (±0.2) molecules pM^{-1}. Middle line (open squares) is adsorption of Cy3B-labeled GLP-1 to bare glass, with a fitted line slope of 0.54 (±0.03) molecules pM^{-1}. Bottom line (solid triangles) is Cy3B-labeled cysteine with a 20-atom polyethylene-glycol linker binding to a DPPC bilayer, with a fitted slope of 0.0040 (±0.0003) molecules pM^{-1}.

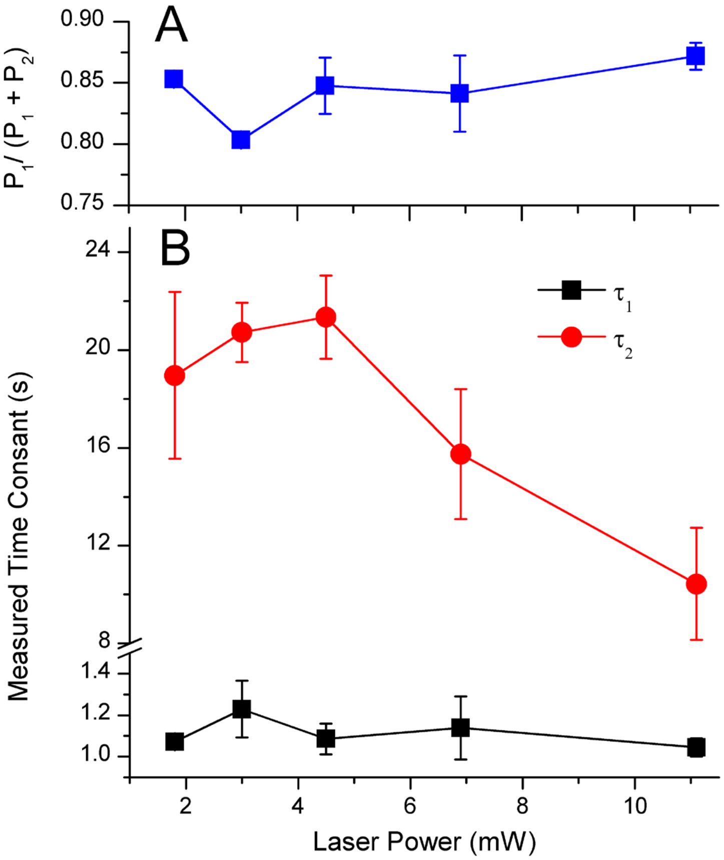

Figure A6. Residence-time histogram kinetics versus laser power. A. Preexponential fraction, $P_1 / (P_1 + P_2)$. B. Fast and slow decay constants, τ_1 and τ_2, respectively. Note the y-axis break between 1.5 and 8 seconds and the change in scale. The preexponential fraction and fast time constant show no correlation with laser power, as does the slow time constant below a laser power of 4.5 mW. Above 4.5 mW, however, the measured slower time constant decreases, suggesting that photobleaching of the dye label shortens the apparent residence times of the longer-lived population. Kinetic parameters reported in the manuscript are for data acquired at 3.0 mW, well below the level where laser power influences the results.

Table A7 Comparison of GLP-1 Kinetic Parameters Measured on Different Systems

Microscope System [A]	τ_1 *(seconds)*	τ_2 *(seconds)*	$P_1 / (P_1+P_2)$	(μm) [B]	Number of events per experiment / # of Experiments
Olympus IX71 514.5-nm Excitation 60x objective Cy3 label	1.26 ± 0.06	20 ± 3	0.867 ± 0.005	5.3 ± 0.1	3500 ± 400 / 3
Nikon TE200 514.5-nm Excitation 100x objective Cy3B label	1.2 ± 0.1	18.2 ± 0.9	0.84 ± 0.01	4.4 ± 0.2	2400 ± 700 / 3
	1.2 ± 0.1	21 ± 2	0.88 ± 0.02		1900 ± 200 / 3
Olympus IX71 532-nm Excitation 60x objective Cy3B label	1.19 ± 0.05	19 ± 2	0.83 ± 0.03	3.6 ± 0.2	1200 ± 300 / 3
	1.2 ± 0.1	21 ± 1	0.8033 ±0.0005		2700 ± 500 / 2

[A] Microscope frame, laser-excitation wavelength, TIRF-objective power, and dye label used on GLP-1.

[B] For missing entries, residence-time histograms at 50-pM GLP-1were replicated (on different days) but no isotherm data were collected.